Fakultät für Medizin

Lehrstuhl für Pharmazeutische Radiochemie

Development of biomarkers for molecular imaging and endoradiotherapy of prostate cancer

Martina Wirtz geb. Weineisen

Vollständiger Abdruck der von der Fakultät für Medizin der Technischen Universität München zur Erlangung des akademischen Grades eines

Doctor of Philosophy (Ph.D.)

genehmigten Dissertation.

Vorsitzender: Univ.-Prof. Dr. Jürgen Ruland

Betreuer: Univ.-Prof. Dr. Hans-Jürgen Wester

Prüfer der Dissertation:

1. apl. Prof. Dr. Sibylle Ziegler
2. apl. Prof. Dr. Klemens Scheidhauer

Die Dissertation wurde am 29.05.2015 bei der Fakultät für Medizin der Technischen Universität München eingereicht und durch die Fakultät für Medizin am 31.08.2015 angenommen.

TABLE OF CONTENTS

Abstract

Due to its consistently high expression in especially metastatic prostate cancer (PCa), PSMA (prostate-specific membrane antigen) represents an ideal target for both diagnostic imaging and endoradiotherapeutic approaches. Several PSMA inhibitors, mostly based on an urea-based zinc-binding motif (KuE-scaffold), have been evaluated preclinically. Meanwhile, [^{68}Ga]HBED-CC-Ahx-KuE ([^{68}Ga]**R3**) is the most studied PSMA inhibitor for PET diagnosis of PCa and initial PSMA-targeted endoradiotherapeutic treatment using [^{131}I]MIP-1095 has been conducted. The goal of this work was the development of novel PSMA inhibitors for PET imaging (^{68}Ga, ^{18}F), SPECT and image-/radioguided surgery (^{111}In, fluorescent dye), and endoradiotherapy (^{177}Lu) of PCa.

In general, the PSMA inhibitors in this study consist of a radiometal chelator or a radiolabeling synthone (e.g. SiFA) conjugated to the KuE-motif (binding to the active center of PSMA) over a peptidic spacer unit. A combined solid-phase peptide synthesis (spacer) and solution phase chemistry (KuE motif) were applied for the synthesis. Determination of the affinity to PSMA (IC_{50}) was performed in a competitive binding assay using PSMA-positive LNCaP cells and ([^{125}I]I-BA)KuE ([^{125}I]**R1**) as the radioligand. Internalization kinetics of the respective radiolabeled inhibitors were investigated using the same cell line. The lipophilicity and metabolic stability of the radiopharmaceuticals was determined, and the *in vivo* targeting was investigated by PET and biodistribution in LNCaP-tumor bearing mice.

An IC_{50} in the low nanomolar range, fast and efficient internalization in LNCaP cells, high PSMA-specific binding, and favorable pharmacokinetics *in vivo*, qualify PSMA inhibitor **19** (PSMA I&T) to be a promising PSMA-targeting radiopharmaceutical. Thus, ^{68}Ga-, ^{111}In- and ^{177}Lu-labeled PSMA I&T were investigated in proof-of-concept studies for theranostic application (diagnosis and endoradiotherapy) in PCa patients. Using [^{68}Ga]PSMA I&T in PET, detection of PCa metastases in bone and lymph nodes was achieved with high image contrast. In radioguided surgery using [^{111}In]PSMA I&T, surgeon confidence for resection of metastatic lesions in lymph nodes was increased. Initial [^{177}Lu]PSMA I&T endoradiotherapy of two patients revealed high uptake of the radiopharmaceutical in PCa lesions resulting in impressive molecular therapy response, PSA reduction and pain relief.

With an IC_{50} of 2.0 ± 0.1 nM and 2.1 ± 0.8 nM, the trimetric (DUPA-Pep-PA)$_3$-[^{nat}Ga]TRAP ([^{nat}Ga]**10**) and [^{nat}Lu]DOTAGA-y-nal-k(Sub-KuE) ([^{nat}Lu]**35**), respectively, revealed the highest affinity in this study. Multimerization is an efficient tool for affinity improvement, however, the “DUPA-Pep” seems to be metabolically instable *in vivo* resulting in increased unspecific background activity. Due to the favorable pharmacokinetics of [^{68}Ga]**35**, high contrast imaging of the PSMA expression *in vivo* was achieved. Internalization kinetics were

fast for all inhibitors, with an > 5-fold increase in internalization for [^{68}Ga/^{177}Lu]DOTAGA-y-nal-k(Glut-(I-f)-KuE) ([^{68}Ga/^{177}Lu]**36**) compared to the literature reference [^{68}Ga/^{177}Lu]DOTA-FFK(Sub-KuE) ([^{68}Ga/^{177}Lu]**R4**). In addition to the almost quantitative plasma-protein binding of [^{177}Lu]**36**, an improved uptake and retention over 24 h in LNCaP-tumors of mice was observed compared to [^{177}Lu]**35** and [^{177}Lu]PSMA I&T.

In conclusion, the theranostic PSMA inhibitor PSMA I&T revealed favorable *in vivo* targeting in [^{68}Ga]PSMA I&T PET, [^{111}In]PSMA I&T radioguided surgery and [^{177}Lu]PSMA I&T endoradiotherapy. Novel inhibitors with increased affinity and internalization into PSMA-expressing cells (**35** and **36**), improved pharmacokinetics towards long-term accumulation in the tumor, and fast excretion from the kidneys have to show their potential in larger cohorts of patients.

Zusammenfassung

PSMA (Prostata-spezifisches Membranantigen) stellt aufgrund der konsistent hohen Expression insbesondere bei metastasiertem Prostatakrebs (PCa) eine ideale Zielstruktur sowohl für diagnostische Bildgebung, als auch für endoradiotherapeutische Ansätze dar. Zahlreiche PSMA-Inhibitoren, welche zumeist aus einem Harnstoff-basiertem Zink-Bindemotiv (KuE) aufgebaut sind, wurden bereits präklinisch evaluiert. [^{68}Ga]HBED-CC-Ahx-KuE ([^{68}Ga]**R3**) ist der im Moment meistuntersuchte PSMA-Inhibitor für die PET Diagnostik des PCa. Mittels [^{131}I]MIP-1095 wurden initiale PSMA-gerichtete endoradiotherapeutische Behandlungen durchgeführt. Ziel dieser Arbeit war die Entwicklung neuer PSMA-Inhibitoren für PET-Diagnostik (^{68}Ga, ^{18}F), SPECT sowie Image-/Radioguided Surgery (^{111}In, Fluoreszenzfarbstoff) und Endoradiotherapie (^{177}Lu) des PCa.

Der generelle Aufbau der PSMA-Inhibitoren in dieser Studie beinhaltet einen Radiometal-Chelator oder ein Radiomarkierungssynthon (z.B. SiFA), welches über einen Peptidlinker an das KuE-Motiv (Bindung zum aktiven Zentrum von PSMA) gebunden ist. Die Synthese erfolgte mittels einer Kombination von Festphasensynthese (Linker) und Kopplungen in Lösung (KuE-Motiv). Zur Bestimmung der Affinität zu PSMA wurde ein kompetitiver Bindungsassay an PSMA-positiven LNCaP-Zellen mit dem Radioliganden ([^{125}I]I-BA)KuE ([^{125}I]**R1**) durchgeführt. Dieselbe Zelllinie wurde zur Bestimmung von Internalisierungskinetiken der jeweiligen radiomarkierten Inhibitoren verwendet. Die Lipophilie und metabolische Stabilität der Radiopharmazeutika wurde bestimmt und das *in vivo*-Targeting in LNCaP-Tumor tragenden Mäusen mittels PET und Biodistribution untersucht.

Ein IC_{50} im nanomolaren Bereich, schnelle und effiziente Internalisierung in LNCaP-Zellen, hohe PSMA-spezifische Bindung und eine vorteilhafte Pharmakokinetik *in vivo* macht den radiomarkierten PSMA-Inhibitor **19** (PSMA I&T) zu einem vielversprechenden PSMA-gerichteten Radiopharmazeutikum. Folglich wurde ^{68}Ga-, ^{111}In- und ^{177}Lu-markiertes PSMA I&T in Machbarkeitsstudien (Proof-of-concept) für die theranostische Anwendung (Diagnose und Endoradiotherapie) an PCa-Patienten eingesetzt. Mittels [^{68}Ga]PSMA I&T konnten in der PET Knochen- und Lymphknotenmetastasen mit hohem Bildkontrast detektiert werden. Durch Radioguided Surgery mittels [^{111}In]PSMA I&T konnte die Zuversicht des Operateurs zur vollständigen Resektion von Lymphknotenmetastasen gesteigert werden. Initiale [^{177}Lu]PSMA I&T Endoradiotherapie zweier Patienten zeigte eine hohe Aufnahme des Radiopharmazeutikums in PCa-Läsionen, welche in einem eindrucksvollen molekularen Therapieansprechen, einer Reduktion des PSA und Schmerzlinderung resultierte.

Mit IC_{50}-Werten von 2.0 ± 0.1 nM und 2.1 ± 0.8 nM zeigten das Trimer (DUPA-Pep-PA)$_3$-[^{nat}Ga]TRAP ([^{nat}Ga]**10**) und [^{nat}Lu]DOTAGA-y-nal-k(Sub-KuE) ([^{nat}Lu]**35**) die höchsten Affinitäten in dieser Studie. Multimerisierung ist ein effizientes Werkzeug zur Erhöhung der Affinität, jedoch scheint „DUPA-Pep“ *in vivo* metabolisch instabil zu sein, was zu erhöhter unspezifischer Hintergrundanreicherung führte. Aufgrund der vorteilhaften Pharmakokinetik von [^{68}Ga]**35**, konnte die Bildgebung der PSMA-Expression *in vivo* mit hohem Kontrast erreicht werden. Die Internalisierungskinetiken waren für alle Inhibitoren schnell, wobei jedoch eine > 5-fach höhere Internalisierung für [^{68}Ga/^{177}Lu]DOTAGA-y-nal-k(Glut-(I-f)-KuE) ([^{68}Ga/^{177}Lu]**36**) im Vergleich zur Literaturreferenz [^{68}Ga/^{177}Lu]DOTA-FFK(Sub-KuE) ([^{68}Ga/^{177}Lu]**R4**) gezeigt werden konnte. Zudem führte eine annähernd quantitative Plasmaproteinbindung bei [^{177}Lu]**36**, im Vergleich zu [^{177}Lu]**35** und [^{177}Lu]PSMA I&T, zu einer verbesserten Aufnahme und Retention über 24 h in LNCaP-Tumoren von Mäusen.

Zusammenfassend zeigte der theranostisch anwendbare PSMA-Inhibitor PSMA I&T vorteilhaftes *in vivo* Targeting in [^{68}Ga]PSMA I&T PET, [^{111}In]PSMA I&T Radioguided Surgery und [^{177}Lu]PSMA I&T Endoradiotherapie. Die neuartigen Inhibitoren mit gesteigerter Affinität und Internalisierung in PSMA-exprimierende Zellen (**35** und **36**), verbesserter Pharmakokinetik bezüglich einer Langzeitakkumulation im Tumor und schneller Exkretion aus den Nieren, müssen anhand eines größeren Patientenkollektivs ihr Potential zeigen.

I BACKGROUND

1 PROSTATE CANCER (PCa)

Although significant progress in prostate cancer (PCa) diagnosis and therapy has reduced death rates, PCa is the most prevalent disease and the third leading cause of cancer related deaths in Germany (1) and other developed countries. An indicator for primary tumors of the prostate is an elevated prostate-specific antigen (PSA) level or abnormalities detected by digital rectal examination (DRE), which are confirmed by needle biopsy and histologic analysis. Recently, the clinical value of PSA-screening was evaluated in big multi-center trials, such as ERSPC (2) in Europe and PLCO (3) in the USA. Associated aspects, such as quality of life and the risk of overtreatment were discussed controversial (4, 5). When PSA screening was approved by the Food and Drug Administration (FDA) in 1994, a normal PSA value was defined to be lower than 4.0 ng/mL. However, a higher PSA is also observed in non-malignant transformations of the prostate, such as prostatitis or benign prostate hyperplasia (BHP) (6). Thus, only in 25 - 35% of men with PSA levels of 4.1 - 9.9 ng/mL subsequent biopsies could confirm PCa (7). But PCa can also be detected in biopsy specimens of patients with PSA levels below 4.0 ng/mL (8).

In relation to tumor size, margin status and pathologic stage, the Gleason score is an important parameter for clinical decisions. The Gleason score is determined from H&E stained sections of biopsy specimens by grading the two most abundant cell populations into five basic patterns (1 - 5), resulting in (summarized) Gleason scores of 2 (well-differentiated normal gland) to 10 (poorly-differentiated carcinoma) (9). On the other hand, biopsies involve the risk of bleeding and infections. In one of three men aged 50 years or older without clinical PCa history, biopsy revealed small, low-grade and therefore clinically irrelevant PCa lesions, entailing risks of overtreatment (10). Overdiagnosis is estimated for 50% of PCa patients (10) and treatment options for primary tumors, such as radical prostatectomy may cause side effects like bladder incontinence and erectile dysfunction. Radiation therapy as an alternative treatment option is associated with pelvic problems, impotence and incontinence (11).

New blood markers are currently evaluated for improved primary diagnosis of PCa. The PHI (prostate health index) includes PSA, free PSA and the isoform p2PSA. PHI and p2PSA were found to predict biopsy results more reliable compared to PSA alone (12). The non-coding mRNA sequence PCA3 (12, 13) is elevated in more than 95% of PCa patients. Due to the specific expression (no transcripts in extra-prostatic tissue), PCA3 is able to distinguish between benign and malignant transformations of the prostate with a specificity of almost 100%. For the detection of primary tumors and for follow up, the PCA3 urine test Progensa™ (Gen-Probe Inc., San Diego, CA) was approved by the FDA in 2012.

Compared to local disease, development of metastatic castration resistant prostate carcinoma (mCRPC) is associated with less than 24% survival for one year (7). Therefore, the distinction of small highly differentiated tumors from aggressive, high-grade malignant carcinomas is of major clinical value as these carcinomas build metastases and cause symptoms finally leading to death. Metastases of prostate cancer are primarily located in lymph nodes and bone. Bone metastases are mostly detected because of symptoms, such as pain, fractures, hypercalcemia and spine compression (14). High PSA values are an indicator, since in 50% of patients with PSA > 100 ng/mL bone metastases were detected (15). These are usually confirmed by radionuclide based bone scans using either [^{99m}Tc]diphosphonates in single-photon emission computed tomography (SPECT) or [^{18}F]fluoride in positron emission tomography (PET) (14). The development of more sensitive and specific biomarkers for PCa diagnosis, as well as discrimination between a primary tumor and (soft tissue) metastasizing disease (staging) is of very high clinical interest.

2 PSMA

2.1 Expression and function

Human prostate-specific membrane antigen (PSMA, glutamate carboxypeptidase II, GCPII, EC 3.4.17.21) is a zinc-metallopeptidase (16). Two pharmacological functions of PSMA are closely linked to prominent sites of PSMA expression (17-20).

a) PSMA acts as “NAALADase”: In the central and peripheral nervous system, *N*-acetylated-α-linked acidic dipeptidase (NAALADase, Fig. 1) hydrolyses *N*-acetyl-L-aspartyl-L-glutamate (NAAG) (21-24). NAALADase is associated with an excessive activation of ionotropic glutamate receptors in acute and chronic neurodegenerative disorders, including stroke (25-27) and amyotrophic lateral sclerosis (28). Inhibition of NAALADase has been substantiated as a treatment approach for stroke (29), amyotrophic lateral sclerosis (30), chronic pain (31-36), diabetic neuropathy (37), and other neurological disorders associated with glutamate excitotoxicity (38).

b) PSMA acts as “folate hydrolase”: Folate (vitamin B_9) is a cofactor of various enzymes involved in nucleotide biosynthesis, e.g. in proliferating tissue (39). Dietary folates consist of a mixture of poly-γ-glutamated pteroic acid, but only the mono-glutamylated form (pteroylglutamate; folate) is actively transported across the intestinal wall into the blood stream (40). To facilitate absorption of folate by conversion of pteroylpoly-γ–glutamate to folate (41, 42), folate hydrolase (FOLH1, Fig. 1) is expressed in the brush border membrane of the small intestine (proximal jejunum) (43, 44).

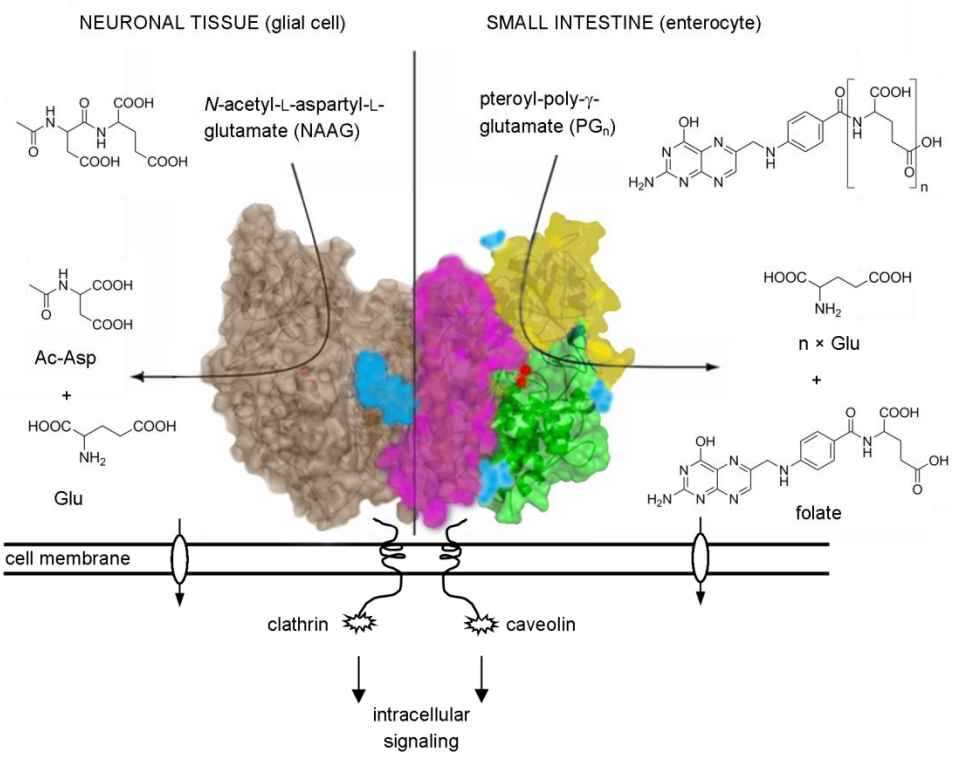

Figure 1. Crystal structure of the human PSMA homodimer: One monomer shown in semitransparent surface representation (green – protease; yellow – apical; purple – *C*-terminal domain) and the second monomer is colored brown. *N*-linked sugar moieties are colored cyan, and the active-site Zn^{2+} ions are shown as red spheres. **Left panel.** NAAG catabolism in the mammalian nervous system. **Right panel.** Folate hydrolase at the plasma membrane of enterocytes. (45)

Besides neuronal tissues and the intestine, PSMA expression was reported in the proximal tubuli of the kidneys, the salivary glands and, to a low extent, also in healthy prostate tissue (18, 42). However, a 1000-fold higher protein expression level was described for PCa (24, 46, 47), which is further increased with progression of the disease (18, 48). The enzymatic function of PSMA in normal and diseased prostate has not been clarified yet (49), but the folate level seems to play a remarkable role (50). In healthy prostate cells, increasing nutritional folate uptake is associated with a protective function against malignant transformations, whereas an increased cancer cell proliferation was observed in PCa patients with high serum folate levels (51). PSMA expression was related to an increased proliferation, migration, and survival of PCa cells *in vitro* (52) and a folate dependent growth advantage of PSMA expressing cells was confirmed (53, 54). On the other hand, a downregulation of PSMA was reported after androgen ablation *in vitro* (55). PSMA expression is also described for thyroid cancer (56) and the neovasculature (57) of numerous other solid tumors, such as gliomas, renal tumors, colorectal carcinomas, breast cancers and osteosarcoma (58-67). Thus, PSMA is a promising tumor marker for PCa, but might also gain importance in a variety of other oncological diseases.

Human PSMA is reported to have 91% homology to the mouse analog (folh1) (68), but species differences in the expression pattern need to be considered. In contrast to humans, no PSMA (folh1) expression is reported in the normal prostate (68, 69) and the small intestine (68) of mice. On the other hand the expression density in the kidneys seems to be much higher compared to humans (70, 71). Differences in plasma-protein binding might also be of importance (45). Nevertheless, mouse models are inevitable for the evaluation of new PSMA targeting agents.

2.2 Crystal structure based inhibitor design

PSMA belongs to the class II transmembrane glycoproteins of the MEROPS M28 peptidase family (72, 73), having homology to the transferrin receptor (74). The gene encoding PSMA (75) is located on chromosome 11 (at position 11p11.2), including 19 exons. The exon-intron structure is associated with an emerging number of splice variants with so far unknown functions (76). The full-length human PSMA protein, comprising 750 amino acids, is a homodimeric transmembrane protein (49). The *N*-terminal cytosolic PSMA tail (amino acid 1 – 18) is essential for PSMA internalization. It interacts with several scaffold proteins including clathrin, clathrin adaptor protein 2, filamin A, and caveolin-1. These interactions modulate PSMA endocytosis via different routes, including caveolae dependent and clathrin-coated pit dependent (receptor mediated endocytosis) mechanisms (77-80). PSMA is internalized in a constitutive manner, yet the internalization rate is increased three-fold by PSMA-specific antibodies bound to the extracellular domain of the protein (81). The large extracellular portion of PSMA (amino acid 44 – 750) serves for substrate recognition and is divided into three domains, the protease domain (green in Fig. 1, amino acids 57 – 116 and 352 - 590), the apical domain (yellow in Fig. 1, amino acid 117 – 351) and the *C*-terminal domain (purple in Fig. 1, amino acids 591 – 750) (45). High *N*-glycosylation (blue in Fig. 1) is crucial for targeting the protein to the cell membrane, proper protein folding, and enzymatic activity, resulting in a total size of 110 kDa (75).

The crystal structure of PSMA was solved by two independent groups (82, 83) in 2006 and provides the basis for development of PSMA inhibitors with high affinity, since the theoretical model for enzyme-substrate interaction (84) and a low-resolution crystal structure (85) are of limited value. Based on the co-crystallization of PSMA with NAAG, as well as small molecule PSMA inhibitors, the substrate binding site/active center of the enzyme was explored in detail.

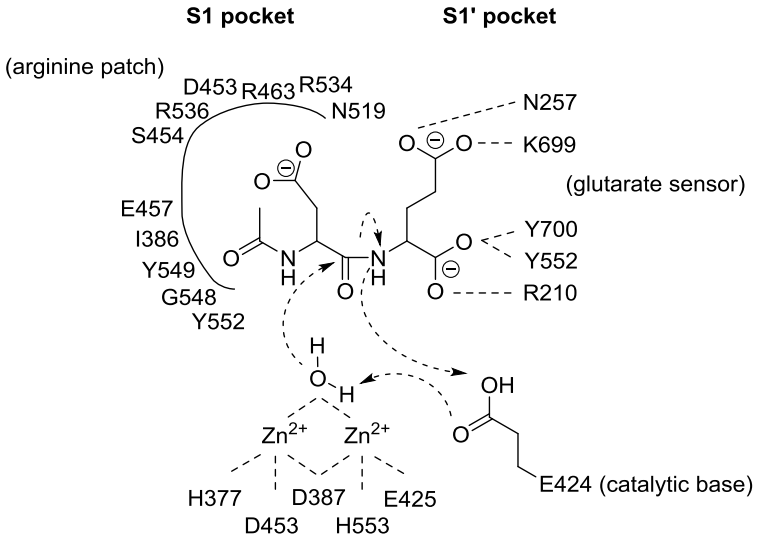

Figure 2. NAAG hydrolysis in the active center of PSMA, as proposed from the crystal structure (82).

In the active center (Fig. 2), two zinc ions are bridged by the β-carboxylate of Asp387 and are further coordinated by the side chains of His377, Glu425, Asp453 and His553 (83). An activated water molecule, which is hydrogen bonded to the conserved Glu424, is located symmetrically between the two Zn^{2+} and is essential for hydrolytic function of PSMA (Fig. 1) (83). According to the respective zinc binding motif, PSMA ligands/inhibitors can be divided into three groups: 1) phospho(i)nates, phosphoramidates (86), 2) thiols (87) and 3) ureas (88). Recently developed hydroxamates (89) and sulfamides (90) revealed lower PSMA affinity. The highly studied urea motif was shown to be an efficient binding moiety for two Zn^{2+} ions, and is stabilized by the residues Tyr552 and His553, forming a co-catalytic site (72, 91).

The S1' (pharmacophore) pocket is specific for L-glutamate (92), as defined by the residues Phe209, Arg210, Asn257, Gly427, Leu428, Gly518, Lys699 and Tyr700 (83). The latter two are part of the 'glutarate sensor' (amino acids 692 – 704), a flexible loop closing the bottom of the S1' pocket (82, 83). For application within the central nervous system efforts were made to increase the lipophilicity of PSMA inhibitors. Lipophilic substitution of the γ-carboxylate of the P1 residue lead to a more than 500-fold decrease in PSMA affinity (93), strengthening the glutamate specificity.

The S1 pocket is responsible for the substrate specificity of PSMA (86) therefore being more flexible compared to the S1' pocket (92, 94). It is defined by the residues Ser454, Glu457, Asp465, Asn519, Gly548, Tyr549, Tyr552 and the 'arginine patch' (Arg463, Arg534 and Arg536), which is stabilized by a chloride ion (82, 83, 86, 95). Interaction of PSMA inhibitors

with the arginine patch is an explanation for the preference of PSMA for substrates containing a P1 α-carboxylate (higher affinity).

For the first potent PSMA inhibitor 2-(phosphonomethyl)pentane-1,5-dioic acid (PMPA) (38) it was found, that only the (R)-enantiomer was cocrystalized in PSMA crystals (PDB code: 2JBJ and 2PVW), although the racemic PMPA was applied (96-98). More recent studies confirm the substrate specificity of PSMA for L-α-amino acid-urea-L-glutamate motifs (36, 96, 99), such as (((R)-1-carboxy-2-mercaptoethyl)carbamoyl)-L-glutamic acid (abbreviations used in the following: CuE for L-cystein-urea-L-glutamate) or (((S)-5-amino-1-carboxypentyl)carbamoyl)-L-glutamic acid (L-lysine-urea-L-glutamate; KuE).

3 PROSTATE CANCER IMAGING

Besides a variety of established imaging techniques, such as magnetic resonance imaging (MRI; dynamic contrast enhanced perfusion - DCE; diffusion-weighted-imaging - DWI), magnetic resonance spectroscopy (MRS), transrectal/Doppler ultrasound (TRUS/Doppler US) or elastography, the molecular imaging techniques PET and SPECT have evolved in recent years for the detection of PCa. Both techniques use the tracer principal to detect physiological abnormality or disturbed biochemical processes with high detection sensitivity. During the last two decades, mostly metabolic tracers have been developed and evaluated for PCa diagnosis in nuclear medicine, e.g. the glucose-analog [^{18}F]FDG, radiolabeled cholines and acetate (^{11}C- and ^{18}F-labeled), the synthetic amino acid [^{18}F]FACBC, and the dihydro-testosterone analog [^{18}F]FDHT. Recently, these metabolic tracers for PCa targeting have been summarized in several reviews (11, 100-103).

Disease specific biomarkers labeled with a radioisotope (radiopharmaceuticals), such as PSMA inhibitors in PCa targeting, reveal remarkable potential in early diagnosis, staging of high-risk patients (intermediate-high), anatomic localization of metastases and local relapse, but also for image-guided biopsy and resection of lymph nodes or capsule exceeding primary disease.

3.1 SPECT imaging

For SPECT, a γ-emitting isotope (often “tagged” to a targeted molecule that acts as *in vivo* vector) is intravenously administered. As the isotope decays, it emits photons, which are detected and recorded by a γ-camera resulting in a digital image of the distribution of the

radioisotope in the human body (assuming that the injected compound is metabolically stable, see III.5.1).

Most γ-cameras (scintillation detectors, Anger cameras) contain a Tl doped NaI crystal, converting γ-energy to a certain amount of light. In an array of 30 – 100 photomultiplier tubes (PMTs), coupled optically (optimized light collection efficiency) to the back face of the crystal, the light is detected and amplified, and finally is converted into an electrical signal (Fig. 3) (104). NaI(Tl) was among the first scintillators developed for γ-rays in a range of 80 – 300 keV, yet it remains a nearly ideal scintillator for detection of the 141 keV γ-rays emitted in the decay of ^{99m}Tc, the most widely used radionuclide for SPECT (105). The number of optical photons created from a γ-ray interaction is generally proportional to the deposited energy (106). The γ-camera is equipped with a collimator with septa to define the direction of the detected γ-rays, deciding between optimized photon-counting sensitivity (parallel hole collimator, Fig. 3) or high resolution (pinhole collimation) (104). Especially for preclinical set-ups, multi-pinhole collimators have been investigated in order to increase the sensitivity and field-of-view, with a preserved spatial resolution (107, 108). For SPECT, acquisition is performed at multiple angles by rotation of often two or three camera heads around the patient (overall covering a 360°-angle) (107). Subsequent image reconstruction leads to a three-dimensional image that reflects the distribution of radiotracer at the time of imaging (109).

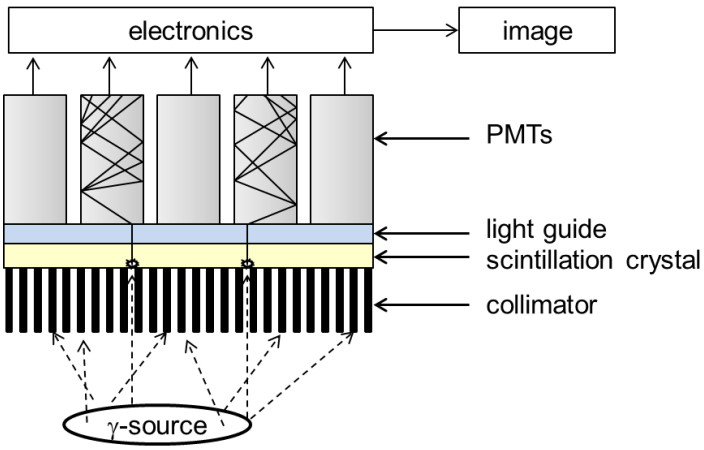

Figure 3. Basic structure of a γ-camera comprising a parallel hole collimator, a scintillation crystal, a light guide that allows light to spread, and an array of PMTs with related electronics.

The resolution of SPECT is 8 - 12 mm for clinical and down to 0.4 mm for preclinical scanners (107), which is determined by the distance of the detector from the γ–source. The extensive use of SPECT for diagnostic imaging in nuclear medicine is also caused by the

favorable nuclide properties of ^{99m}Tc and its ready availability from ^{99}Mo/^{99m}Tc-generators. A selection of important SPECT radionuclides is given in Table 1.

Table 1. Selected SPECT isotopes (photon emitters) and their physical properties (110). IT – isomeric transition; EC – electron capture.

nuclide	half-life	decay	γ-energy [keV]
^{99m}Tc	6.0 h	IT	141
^{123}I	13.2 h	EC	159, 529
^{67}Ga	3.3 d	EC	93, 185, 300
^{111}In	2.8 d	EC	171, 245
^{201}Tl	73.1 h	EC	167, 135

SPECT radiopharmaceuticals in PCa imaging: Due to the high accessibility as a cell surface protein and the overexpression on PCa cells, PSMA represents an excellent target for molecular imaging of PCa. Based on the murine monoclonal antibody 7E11, [^{111}In]Capromab pendetide (ProstaScint, Cytogen Corporation) was approved by the FDA in 1996 for radioimmunoscintigraphy in PCa patients potentially suffering from soft tissue metastases (111). Unfortunately, recent reports confirmed that 7E11 is directed against the intracellular domain of PSMA (112, 113), resulting in low sensitivity. To increase antibody uptake and sensitivity in the detection of PCa metastases, alternative antibodies against the extracellular portion of PSMA were developed (114), such as J591 (57). The J591 antibody was radiolabeled with ^{99m}Tc and ^{111}In and subsequently used for SPECT imaging in patients (115). [^{111}In]J591 revealed high tumor-uptake and low non-specific binding (116).

Small molecule PSMA inhibitors, based on phosphoramidates and ureas, were also developed for SPECT imaging. A broad range of ^{99m}Tc(I) tricarbonyl chelates of phosphoramidat- (117, 118) and urea-based PSMA inhibitors, as well as ^{99m}Tc(III) and ^{99m}Tc(V) ligands were reported and comparatively evaluated preclinically (119-123). Due to impressive preclinical data, such as a persistent tumor-retention of [^{99m}Tc]MIP-1404 over 24 h (122), [^{99m}Tc]MIP-1404 and [^{99m}Tc]MIP-1405 (Fig. 4) were transferred to the clinics (124) and a phase 2 clinical study is currently performed. Especially using [^{99m}Tc]MIP-1404 ([^{99m}Tc]Trofolastat) SPECT, PCa metastases in bone and lymph nodes could be detected with high image contrast. Furthermore, the tracer uptake in bone metastases was successfully correlated to conventional bone scans with radiolabeled phosphonates (124).

Radioiodinated (^{123}I) small molecule PSMA inhibitors with favorable targeting characteristics were developed and evaluated preclinically (125, 126). Initial clinical application of both,

[^{123}I]MIP-1072 and [^{123}I]MIP-1095 (Fig. 4) revealed clear visualization of bone and lymph node metastases (radiologic evidence) (127). Whereas [^{123}I]MIP-1072 is washed-out from PSMA-negative tissues and excreted over the bladder (54 ± 5% within 24 h), [^{123}I]MIP-1095 shows slow excretion kinetics (only 7.5 ± 4.7% of the injected dose was eliminated over the kidneys/bladder within 24 h).

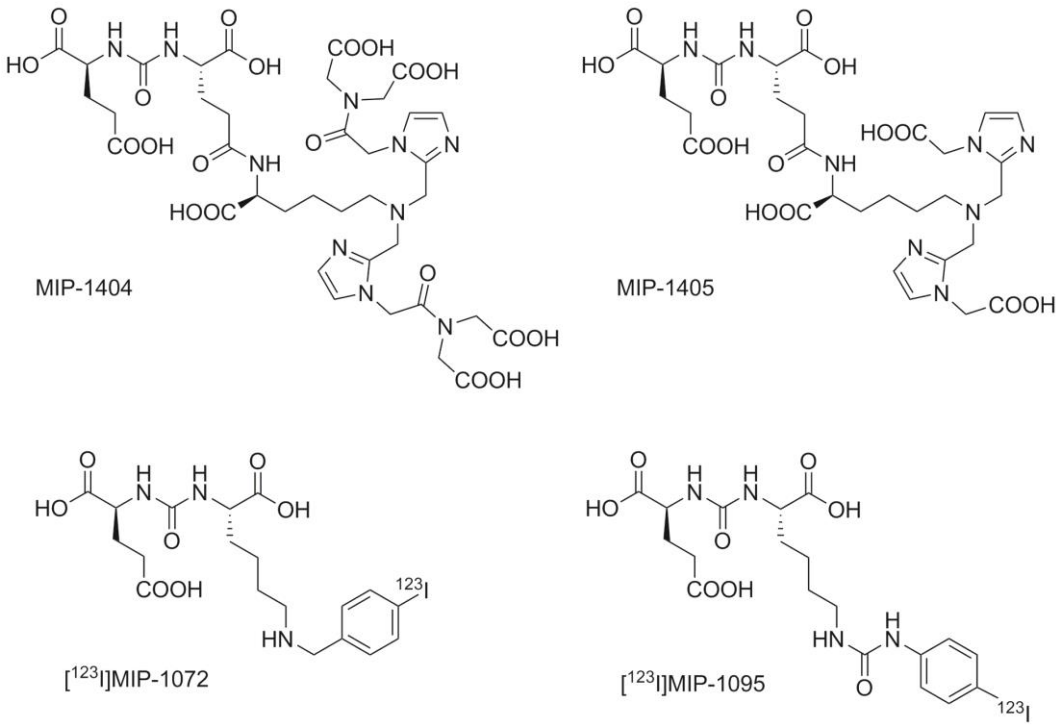

Figure 4. Structures of the PSMA inhibitors MIP-1404 and MIP-1405 (for radiolabeling with [^{99m}Tc(CO)$_3$(H$_2$O)$_3$]$^+$) (122), and the radioiodinated PSMA inhibitors [^{123}I]MIP-1072 and [^{123}I]MIP-1095 (127). All four inhibitors are currently under clinical investigation for PCa SPECT.

3.2 PET imaging

In the radioactive decay by positron emission, a proton in the nucleus is transformed into a neutron, a positron (β^+) and a neutrino (ν) (128).

$$ {}^{A}_{Z}X_N \rightarrow {}^{A}_{Z-1}X_{N+1} + \beta^+ + \nu $$

The ejected positron loses its kinetic energy in collisions with atoms of the surrounding matter (ionization, electronic excitation, *bremsstrahlung*), usually within a few millimeters from the emission site (depending on the initial positron energy). The thermalized positron and an electron from the surrounding matters form a positronium in an annihilation reaction, in which their masses are converted into energy. This energy is emitted by two 511 keV γ-

photons in a 180°-angle (Fig. 5) (128, 129). The precise directional relationship of the two photons is used in PET. Annihilation coincidence counting (Fig. 5) by circular detector pairs placed around the patient (opposite γ-detectors give a signal within 6 – 12 nanoseconds), allow the detection and localization of positron-emitters *in vivo* (129). From the 2-dimensional projections mathematical algorithms, such as filtered backprojection or iterative approaches (e.g. ordered subset expectation maximization - OSEM) are used to reconstruct 3-dimensional images (130).

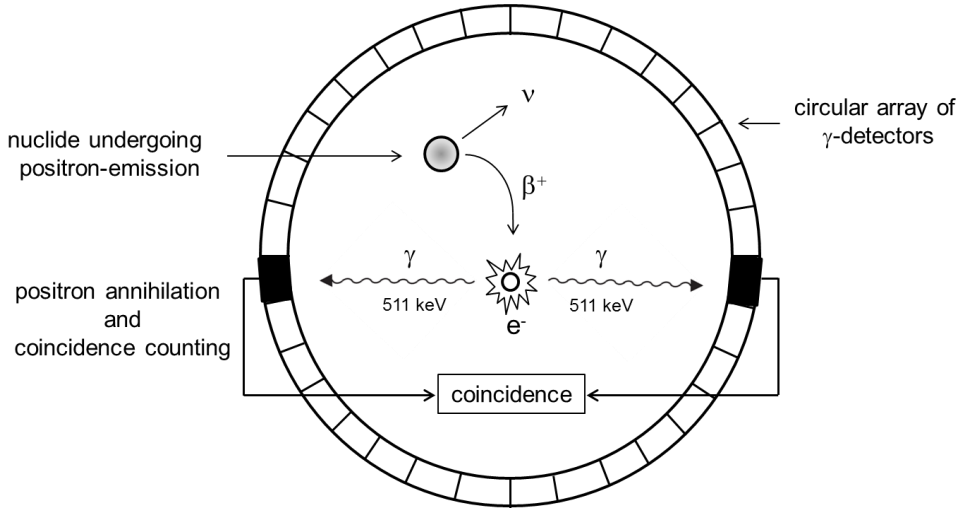

Figure 5. Schematic representation of a radioisotope that decays by β^+-emission, followed by annihilation of the formed positronium resulting into two 511 keV γ-quanta and acquisition of this irradiation by two small opposite detector units electronically connected via a coincidence circuit.

To quantify a PET signal, corrections for detector differences, randoms, scatter, attenuation, and dead time need to be applied to the projections prior to reconstruction (130, 131). In addition to these corrections, calibration factors must be determined to translate the corrected counts to radioactivity values (kBq/cm^3) (130). The PET signal in a region of interest is then expressed as % injected dose per mL (% ID/mL) or as standardized uptake value (SUV):

$$\mathrm{SUV} = \frac{\text{activity concentration in image } \left[\frac{\mathrm{kBq}}{\mathrm{mL}}\right] \times \text{ body weight [kg]}}{\text{injected activity [kBq]}}$$

However, in small structures the positron range (distance between emission and annihilation) leads to an underestimation in intensity, since the activity signal (same total counts) is

distributed over a larger volume (partial volume effect) (132). Thus, spatial resolution of app. 4 - 6 mm for clinical and 1 - 2 mm for preclinical PET scanners (133) is determined by the finite positron range and photon non-colinearity (annihilation photon departure trajectories are not exactly 180° apart) (134, 135). A selection of important positron emitting radioisotopes, half-lives and positron-energies is summarized in Table 2.

Table 2. Physical properties of selected PET isotopes (positron emitters) (110).

nuclide	half-life	maximum β^+-energy (abundance)
^{15}O	2.0 min	1.7 MeV (99.8%)
^{13}N	10.0 min	1.2 MeV (100%)
^{11}C	20.4 min	1.0 MeV (99.8%)
^{18}F	109.7 min	0.6 MeV (96.9%)
^{68}Ga	67.6 min	1.9 MeV (90%)
^{64}Cu	12.7 h	0.7 MeV (19.3%)
^{89}Zr	78.4 h	0.9 MeV (22.7%)
^{124}I	4.2 d	2.1 MeV (25%)

To reflect the biologic process of interest, the imaging time point has to be chosen carefully, as the spatial distribution of a radiopharmaceutical in the body changes with time. Dynamic PET imaging enables the measurement of radiotracer concentrations as a function of time. The PET acquisition is divided into time frames, which are reconstructed separately and thus, time-dependent changes in the activity concentration in regions of interest can be evaluated. For tracer kinetic modeling, mathematical models (on one or more parameters; compartment models) can be constructed to describe the radiopharmaceuticals' (or its metabolites') kinetics in the body (136-138).

PET radiopharmaceuticals in PCa imaging: The radiolabeled PSMA antibody J591 (57), its humanized analog huJ591 and a minibody version of huJ591 (139-142) were evaluated for PET imaging. However, due to slow antibody clearance kinetics, late imaging time points (optimum 7 days p.i.), and thus somewhat complicated imaging protocols, the clinical applicability of [^{89}Zr]J591 is challenging (141).

In contrast to radiolabeled antibodies, the use of small molecule PSMA inhibitors with fast pharmacokinetics and high PSMA affinity in combination with short-lived radioisotopes allow

for a simplified work flow and provide favorable characteristics for PET imaging. A broad range of PET tracers for PSMA targeting have been developed and preclinically evaluated. Due to the very short half-lives of ^{15}O and ^{13}N, both isotopes do not provide a basis for targeted imaging, whereas ^{11}C (143), and especially ^{18}F is of major clinical interest due to the favorable nuclide properties (Table 2). Thus, intensive research was conducted on the development of ^{18}F-labeled PSMA inhibitors, such as the small-molecule inhibitor 2-(3-{1-carboxy-5-[(6-[^{18}F]fluoro-pyridine-3-carbonyl)-amino]-pentyl}-ureido)-pentanedioic acid ([^{18}F]DCFPyL) (144), (*N*-[*N*-[(S)-1,3-dicarboxypropyl]carbamoyl]-4-[^{18}F]fluorobenzyl-L-cysteine ([^{18}F]DCFBC) (145), (*N*-[*N*-[(S)-1,3-dicarboxypropyl]carbamoyl]-4-[^{18}F]fluoroethyl-L-tyrosine ([^{18}F]FEtTUG) (146) and a ^{18}F-labeled PMPA analog (BAY 1075553) (147, 148). Besides the SPECT application, peptides based on DUPA-Pep (Fig. 6) (120) represent promising candidates for ^{18}F- (149, 150) and ^{68}Ga-based PET imaging (151, 152) and a ^{68}Ga-labeled PSMA inhibitor (DOTA-FFK(Sub-KuE), Fig. 6) revealed promising tumor targeting properties in a preclinical study (153).

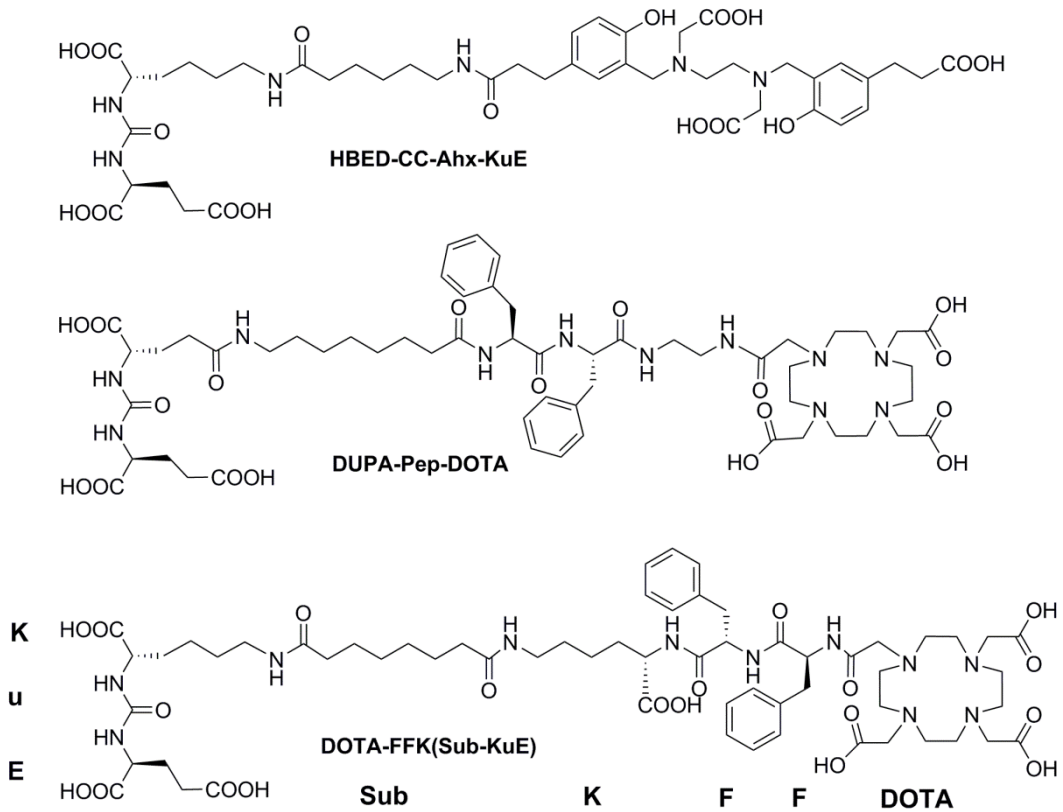

Figure 6. Structures of selected PSMA inhibitors reported for PET imaging of PCa.

The most extensively studied PSMA-directed PET tracer so far is [^{68}Ga]HBED-CC-Ahx-KuE (Fig. 6), initially published by Eder et al (99). In several studies (154-158), [^{68}Ga]HBED-CC-

Ahx-KuE PET allowed the detection of primary tumors, as well as lymph node and bone metastases with high sensitivity and specificity. Thus, the clinical value was proven in comparison to [^{18}F]fluoromethylcholine, a PCa directed PET tracer studied in detail in recent years. First clinical application for [^{18}F]DCFBC PET/CT (159) revealed a decelerated blood clearance, and clearly decreased tracer uptake in salivary glands compared to [^{68}Ga]HBED-CC-Ahx-KuE. Interestingly, a phosphonate-based PSMA inhibitor BAY 1075553 (PMPA analog) revealed promising preclinical targeting properties. However, in a direct comparison to [^{18}F]fluoromethylcholine lower detection rates of lymph node and bone metastases were found for BAY 1075553 (160).

4 IMAGE/RADIOGUIDED SURGERY

New technologies enable intraoperative γ- or fluorescence detection during surgery. The freehand SPECT system (declipseSPECT, SurgicEye, Munich, Germany) was developed to allow the intraoperative visualization of radioactivity within a reconstructed 3D-SPECT image. The position and count rate of the γ-probe is recorded by an optical tracking system. Once enough spatial information about the activity distribution has been acquired, a 3D-image is reconstructed. This image is then co-registered with a live video stream of the surgical field to provide an augmented reality display during radioguided surgery, showing the position of radioactive hotspots (161).

Due to the complementary physical properties of optical and radioactive probes, bimodal derivatives (radioactive and fluorescent label) or a combination of optical probes and radiotracers could provide additional information for surgical removal of PCa primary tumors (delineation of tumor margins) and resection of lymph node metastases. Other than with radionuclide-based imaging (PET and SPECT), fluorescent probes require light excitation before a fluorescent emission can be detected. Thus, optical imaging suffers from high background signal and limited tissue penetration compared to radioactivity based detection techniques, but allows real-time optical detection of the signal, with a microscopic resolution (162). Depending on the excitation wavelength, reflectance, scattering and tissue auto-fluorescence influence the imaging (163). Tissue penetration and auto-fluorescence was shown to be improved for near infrared dyes compared to dyes and quantum dots in the visible range (164).

Fluorescent and bimodal PSMA inhibitors for PCa targeting: For the antibody D2B bimodal tumor detection and image-guided surgery using [^{111}In]DTPA-D2B-IRDye800CW was described in a mouse model (165). The application in optical imaging and intraoperative detection of tumors, but also high resolution imaging of intracellular processes (166), are subjects of research for PSMA-targeted fluorescent (167-171) and bimodal (121) probes.

5 THERAPY OF PCa

As long as the disease is restricted to the prostate, radical prostatectomy and radiation therapy exhibit high efficacy (172) in the therapy of PCa. Current treatment options for PCa patients with metastatic disease are androgen deprivation therapy and chemotherapy (173). However, these therapies cause potentially serious adverse effects. Most aggressive forms of PCa develop androgen and chemotherapy resistances, resulting in mCRPC being associated with poor clinical prognosis.

Endoradiotherapeutic treatment relies on the specific delivery of therapeutic radionuclides (Table 3) to target-expressing cells, therefore inherently providing a means for high therapeutic efficiency even in small metastases (loss of the cell vitality and its disability of mitosis due to chromosome aberrations) (174). Therefore, dependent on the tumor size, the tumor type, and the addressed target, a radionuclide with appropriate energy, and thus tissue penetration has to be selected for efficient irradiation of the malignant cells with a minimum of damage to the surrounding healthy tissue (175, 176).

Table 3. Physical properties of selected therapeutic isotopes (110).

nuclide	half-life	decay	maximum β^--/α-energy (mean tissue range)	γ-energy [keV]
^{90}Y	64.1 h	β^-	2.3 MeV (2.8 mm)	-
^{188}Re	17.0 h	β^-	2.1 MeV (2.4 mm)	155, 633
^{186}Re	89.3 h	β^-	1.1 MeV (0.9 mm)	137
^{177}Lu	6.7 d	β^-	0.5 MeV (0.3 mm)	113, 208
^{131}I	8.0 d	β^-	0.8 MeV (0.4 mm)	364, 637, 284
^{213}Bi	45.6 min	α β^-	5.9 MeV (0.06 mm) 1.4 MeV (1.2 mm)	440
^{211}At	7.2 h	α	5.9 MeV (0.1 mm)	687
^{223}Ra	11.4 d	α	5.8 MeV (0.1 mm)	269, 154, 324

β-particles: Most β^--emitting radionuclides are easily accessible via (n,γ)-processes in nuclear reactors. Depending on the production route, ^{177}Lu can either be produced by ^{176}Lu(n,γ)^{177}Lu (carrier added; c.a.) or from highly enriched ^{176}Yb (> 99%) by ^{176}Yb(n, γ)^{177}Yb $\xrightarrow{\beta^-,\, t_{1/2}=1.9\,h}$ ^{177}Lu (non-carrier added; n.c.a.) (177). Thus, c.a. ^{177}Lu contains the long-lived ^{177m}Lu ($t_{1/2}$ = 160.1 d) and resulting differences in the specific activity of the radiolabeled product (number of decays per time divided by the amount of substance [GBq/µmol]), might influence target saturation in subsequent *in vitro* and *in vivo* applications.

The β^--particles deliver a cytotoxic level of radiation to the vicinity of the target and thus the radiotoxic effect is not restricted to the cells expressing the targeted epitope. This "crossfire effect" is important for the treatment of tumors with heterogeneous target expression or with insufficient vascularization and thus limited tracer delivery to all tumor cells (178). Many β^--emitters also exhibit γ-emission, which generally does not contribute to the desired dose in the target tissue, but increases the undesired whole-body radiation dose. However, when γ-emission is limited to a low abundance and ideal energies in the range of typical SPECT emitters, the accompanying γ-emission can be used to monitor endoradiotherapeutic treatments by means of SPECT (or planar scintigraphy) and to calculate the internal dosimetry (179).

α-particles: The α-emitter ^{213}Bi is produced by an ^{225}Ac/^{213}Bi-generator. Due to the high energy and low range of the α-particles in tissue (and thus linear energy transfer - LET), α-particles exhibit a strong radiotoxic effect. Therefore high tumor-selectivity of the targeting molecule and rapid clearance from non-target organs are of major importance. Their low range also entail that the radiopharmaceutical needs to be delivered "just-in-place". Thus, homogenous target expression (and distribution of the radiopharmaceutical) is of utmost importance for endoradiotherapeutic treatments with α-emitters (179).

Auger-electron emission: Decay by electron capture or internal conversion results in low energy electron (Auger-electron) emissions. Internalization and translocation of Auger-electron emitters to the cell nucleus (max. distance of 5 – 10 nm from nuclear DNA) is a prerequisite for radiotherapy with Auger-electron emitters, such as ^{111}In, ^{123}I, ^{125}I or ^{99m}Tc. Thus, the most successful experiments with Auger-electron emitters have been made with compounds that intercalate into the DNA (180).

Radiopharmaceuticals in PCa treatment: For radiotherapeutic treatment, the calcium mimetic α-emitter [^{223}Ra]radium dichloride (Xofigo, Bayer AG) was recently approved. Xofigo is indicated in patients with mCRPC that has spread to bones, if organ and lymph node metastases can be excluded. Xofigo treatment improved overall survival by only 3.6 months (181). Thus, there is a major need for additional therapeutic options, especially for patients with non-osseous metastases.

For radioimmunotherapy, J591 was labeled with ^{131}I, ^{90}Y, and ^{177}Lu. [^{90}Y]- and [^{177}Lu]J591 were evaluated in separate clinical studies for the treatment of patients with mCRPC (116, 139, 182-184) and both radiopharmaceuticals targeted bone and lymph node metastases. Using [^{177}Lu]J591, a better therapy response in terms of PSA decline (in 64% of patients) was observed (184) and the patient survival could be prolonged for 9.9 months (21.8 vs. 11.9 months) (140).

Recently, first-in-human endoradiotherapeutic application of [^{131}I]MIP-1095 in 28 patients was conducted, accompanied by PET-based dosimetry estimation using the ^{124}I-labeled analog (185). After application of an average of 4.8 GBq [^{131}I]MIP-1095, the PSA value decreased in 61% of the patients and a pain reduction was achieved for patients with bone metastases, therefore proving the feasibility of an endoradiotherapeutic PCa treatment approach.

6 OBJECTIVES

In general, the tissue uptake of a radiopharmaceutical is dependent on the properties of the tissue, such as target expression profile, non-specific binding, perfusion, diffusion/transport across membranes, and cellular localization of the target, as well as on the radiopharmaceutical's properties, such as affinity, specificity, selectivity, stability/metabolism, and specific activity. Due to the favorable expression profile and high accessibility of the cell-surface enzyme PSMA for small-molecule inhibitors, the goal of this work was the development of urea (KuE)-based PSMA inhibitors for PET imaging (labeling with ^{68}Ga, ^{18}F), SPECT imaging and image-guided surgery (^{111}In, optical dye), as well as ^{177}Lu-based endoradiotherapeutic treatment of PCa patients.

The increased availability of radioisotopes for radiopharmaceutical applications in imaging (I.3 and I.4) and therapy (I.5) has also driven the development of new coordination chemistry. Compared to the cyclotron produced ^{18}F, revealing the most favorable nuclide properties for PET imaging, the radiometal ^{68}Ga has the advantage of high availability through a ^{68}Ge/^{68}Ga-generator and a fast and efficient radiolabeling via automated synthesizers (186) to produce a concentrated, chemically and radiochemically pure, aqueous and isotonic solution ready-for-injection. The chelators used for ^{68}Ga^{III}-complexation are mostly based on linear or

macrocyclic polyamines modified with negatively charged pendant arms (carboxylates). Among them, 1,4,7,10-tetraazacyclododecane-1,4,7,10-tetraacetic acid (DOTA) (187) is one of the most investigated $^{68}Ga^{III}$-chelators. Other commonly used chelators are 1,4,7-triazacyclononane-triacetic acid (NOTA) (188), and the recently developed macrocycles with phosphinic acid arms 1,4,7-triazacyclononane-1,4-bis[methylene (hydroxymethyl)phosphinic acid]-7-[methylene(2-carboxyethyl)phosphinic acid] (NOPO) (189) and 1,4,7-triazacyclononane-triphosphinic acid (TRAP) (190), all of which form ^{68}Ga-chelates with higher kinetic inertness and/or thermodynamic stability compared to DOTA (190). Further advantages of both, NOPO and TRAP are labeling at a low pH (< 1) and high labeling yields using even less than 1 nmol of chelator, resulting in high specific activities (190). The effect of different chelators and complexes with various metals, such as ^{68}Ga and ^{64}Cu was investigated for PSMA inhibitors developed from DOTA-FFK(Sub-KuE) (Fig. 7) as the starting point. To explore the effect of multimerization on PSMA inhibitor properties, all three pendant arms of TRAP were coupled to the commercially available PSMA inhibitor DUPA-Pep (120) (ABX, Radeberg, Germany, Fig. 6). Recently, ^{68}Ga-labeling of the acyclic chelator *N*,*N'*-bis[2-hydroxy-5-(carboxyethyl)benzyl]ethylenediamine-*N*,*N'*-diacetic acid (HBED-CC) (99) was reported for a PSMA inhibitor with favorable PSMA targeting properties. Thus, [^{68}Ga]HBED-CC-Ahx-KuE was used as the literature reference in this study.

For PET imaging a variety of ^{18}F-based imaging agents are currently being evaluated. Conventional methods for radiofluorination are based on multi-step procedures and involve prosthetic groups. An objective of this work was to develop PSMA inhibitors comprising a fast and efficient radiolabeling procedure. Thus, conjugation of the silicon-based fluoride acceptor-motif (4-di-*tert*-butylfluorosilanebenzoic acid, SiFA-BA) (191), and complexation of $[Al^{18}F]^{2+}$ using a NOTA-conjugated PSMA inhibitor (192) was investigated.

Driven by the clinical interest in intraoperative detection of tumor metastases, the feasibility of applying a radioactive or optical probe to detect tumor lesions during surgery (e.g. lymph node resection) was explored. Approaches towards bimodal imaging by conjugation of a fluorescent dye to a chelator-bound PSMA inhibitor, as well as application of an ^{111}In-labeled PSMA inhibitor for radioguided surgery were made.

Based on DOTA-FFK(Sub-KuE) (153) (Fig. 7) lead structures for theranostic application (diagnosis and therapy using the same inhibitor by exchange of the radiometal) or radionuclide based therapy of PCa were developed. In contrast to HBED-CC, NOTA, NOPO and TRAP, DOTA can also be used for complexation of larger metal ions, particularly lanthanides like the therapeutic radiometal $^{177}Lu^{III}$. The DOTA analog 1,4,7,10-tetraazacyclododecane,1-(glutaric acid)-4,7,10-triacetic acid (DOTAGA) (193, 194) was examined to serve as the chelator for diagnostic as well as therapeutic radiometals. To

increase therapeutic efficiency of the endoradiotherapeutics, favorable pharmacokinetics, as well as high uptake and retention of the radiopharmaceutical in the tumor were the major objectives.

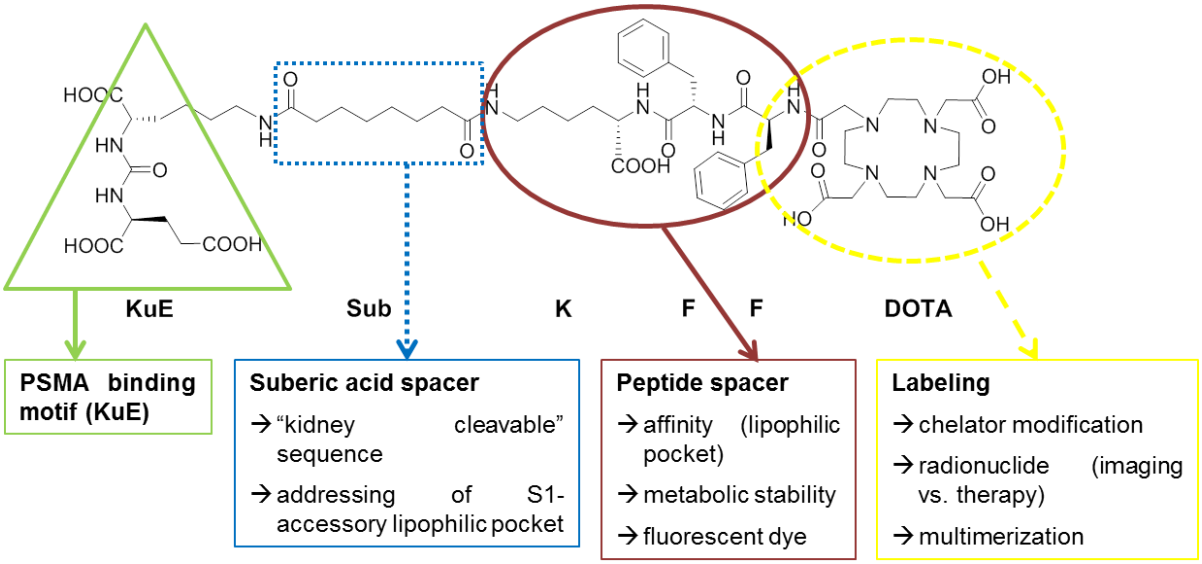

Figure 7. Schematic overview of DOTA-FFK-Sub-KuE based synthetic modifications for the development of novel PSMA inhibitors in this study.

Although PSMA expression is reported for the kidneys, and renal excretion is preferred over hepatobiliary excretion in terms of radiation dosimetry, efforts to minimize renal uptake were made to avoid nephrotoxicity during endoradiotherapeutic applications. Besides other described approaches towards reduction of kidney accumulation of radiopharmaceuticals (195-197), interposition of a kidney-selective cleavable linkage between the biomolecule and the radiolabel (198) was explored ("kidney-cleavable" sequence). Further, the impact of structural modifications and variation of the peptide amount on the kidney uptake of the radiopharmaceuticals were examined.

A central objective of the PSMA inhibitor design for diagnostic as well as therapeutic inhibitors was to increase the affinity (by chelator modification, spacer substitution, inhibitor multimerization; Fig. 7). Robust systems for affinity determination (IC_{50}), as well as cellular uptake and internalization kinetics assessment had to be established for a reproducible, comparative *in vitro* evaluation of all PSMA inhibitors in this study and future developments. Further, the lipophilicity and metabolic stability was determined. Imaging and biodistribution data were the basis for decisions on the suitability of novel candidates. Based on the preclinical results, initial proof-of-concept studies in humans to target PCa with the novel PSMA inhibitors were conducted.

II MATERIALS AND METHODS

1 GENERAL

Fmoc- (9-fluorenylmethoxycarbonyl-) and all other protected amino acid analogs were purchased from Iris Biotech (Marktredwitz, Germany) or Bachem (Bubendorf, Switzerland). TCP-resin was obtained from PepChem (Tübingen, Germany). The chelators NOTA, DOTA, DOTA-tris-*tert*-butyl-ester and DOTAGA-anhydride were purchased from Chematech (Dijon, France). NOPO was kindly provided by Dr. Jakub Simecek and TRAP was obtained from Dr. Johannes Notni. Solvents and all other organic reagents were purchased from SigmaAldrich (Munich, Germany) or CLN (Freising, Germany). Solid phase peptide synthesis was carried out manually using an Intelli-Mixer syringe shaker (Neolab, Heidelberg, Germany). Analytical reversed-phase high performance liquid chromatography (HPLC) was performed on a Nucleosil 100 C18 (5 µm, 125 × 4.0 mm) column (CS GmbH, Langerwehe, Germany) using a Sykam gradient HPLC system (Sykam GmbH, Eresing, Germany). The peptides were eluted applying different gradients of 0.1% (v/v) trifluoroacetic acid (TFA) in water (solvent A) and 0.1% TFA (v/v) in acetonitrile (solvent B) at a constant flow of 1 mL/min (specific gradients are cited in the text). UV-detection was performed at 220 nm using a 206 PHD UV-Vis detector (Linear^{TM} Instruments Corporation, Reno, USA). Both retention times t_R as well as the capacity factors *K'* are cited in the text. Preparative HPLC was performed on the same HPLC system using a Multospher 100 RP 18 - 5 (250 × 20 mm) column (CS GmbH, Langerwehe, Germany) at a constant flow of 10 mL/min. Radio-HPLC of the radioiodinated reference ligand was carried out using a Nucleosil 100 C18 (5 µm, 125 × 4.0 mm) column. For radioactivity detection, the outlet of the UV-photometer was connected to a NaI(Tl) well-type scintillation counter from EG&G Ortec (Munich, Germany). Radio-HPLC and Radio-TLC analysis of ^{68}Ga-labeled compounds was done as described previously (190). Electron-spray ionization mass spectrometry (ESI-MS) was conducted on a Varian 500-MS IT mass spectrometer (Agilent Technologies, Santa Clara, USA).

2 SYNTHESIS OF PSMA INHIBITORS

2.1 PSMA binding motif lysine-urea-glutamate (KuE)

The PSMA binding motif KuE was synthesized with *t*Bu-protected carboxylates (71) in an optimized literature procedure (126).

(1)

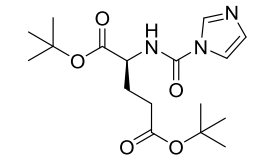

Chemical Formula: $C_{17}H_{27}N_3O_5$
Molecular Weight: 353.41 $gmol^{-1}$

(S)-Di-*tert*-butyl 2-(1H-imidazole-1-carboxamido)pentanedioate: A suspension of 2.50 g (9.64 mmol, 1.0 eq.) L-di-*tert*-butyl-glutamate·HCl in 25 mL dichloromethane (DCM) was cooled to 0 °C, and 3.36 mL triethylamine (TEA) (24.1 mmol, 2.5 eq.) and 4.1 mg (0.38 mmol, 0.04 eq.) 4-(dimethylamino)pyridine (DMAP) were added. After stirring for 5 min, 1.72 g (10.6 mmol, 1.1 eq.) carbonyldiimidazole (CDI) dissolved in 10 mL DCM were slowly added. The mixture was then allowed to warm to room temperature (rt) and was stirred overnight. After diluting with 25 mL DCM, the reaction was quenched with 10 mL saturated $NaHCO_3$ solution, washed twice with water (15 mL each) and brine (15 mL) and dried over Na_2SO_4. The solvent was evaporated, and the crude product was used for further reaction steps without purification. HPLC (10 to 90% B in 15 min): t_R = 12.2 min; K' = 5.8. Calculated monoisotopic mass ($C_{17}H_{27}N_3O_5$): 353.4 found: m/z = 376.0 $[M+Na]^+$.

(2)

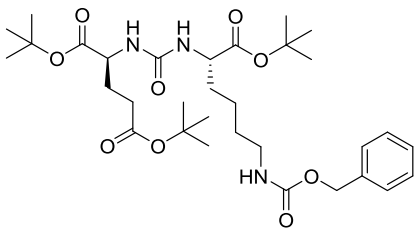

Chemical Formula: $C_{32}H_{51}N_3O_9$
Molecular Weight: 621.76 $gmol^{-1}$

(9R,13S)-tri-*tert*-butyl-3,11-dioxo-1-phenyl-2-oxa-4,10,12-triazapentadecane-9,13,15-tricarboxylate: A solution of 3.40 g (9.64 mmol, 1.0 eq.) **1** in 45 mL 1,2-dichloroethane (DCE) was cooled to 0 °C, and 2.69 mL (19.28 mmol, 2.0 eq.) TEA and 3.59 g (9.64 mmol, 1.0 eq.) H-Lys(Cbz)-O*t*Bu·HCl were added under vigorous stirring. The reaction mixture was heated to 40 °C overnight. The solvent was removed *in vacuo* and the crude product was purified via silica gel flash-chromatography using an eluent mixture of ethyl acetate/hexane/TEA (500/500/0.8 (v/v/v)). Upon solvent evaporation, 4.80 g of **2** were obtained as a colorless, sticky oil (yield: 80% based on L-di-*tert*-butyl-glutamate·HCl). HPLC (40 to 100% B in 15 min): t_R = 14.3 min; K' = 8.5. Calculated monoisotopic mass ($C_{32}H_{51}N_3O_9$): 621.8 found: m/z = 622.2 $[M+H]^+$, 644.3 $[M+Na]^+$.

(3)

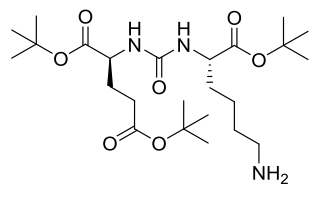

Chemical Formula: $C_{24}H_{45}N_3O_7$
Molecular Weight: 487.63 $gmol^{-1}$

Di-*tert*-butyl (((S)-6-amino-1-(tert-butoxy)-1-oxohexan-2-yl) carbamoyl)-L-glutamate ((O*t*Bu)KuE(O*t*Bu)$_2$): For Cbz-deprotection, 6.04 g (9.71 mmol, 1.0 eq.) **2** were dissolved in 150 mL ethanol, and 0.60 g (1.0 mmol, 0.1 eq.) palladium on activated charcoal (10%) were added. After purging the flask with H_2, the solution was stirred overnight under light H_2-pressure (balloon). The crude product was filtered through celite, the solvent was evaporated *in vacuo*, and the desired product was obtained as a waxy solid (4.33 g, 91.5% yield). HPLC (10 to 90% B in 15 min): t_R = 12.6 min; K' = 6.4. Calculated monoisotopic mass ($C_{24}H_{45}N_3O_7$): 487.6 found: m/z = 488.3 $[M+H]^+$, 510.3 $[M+Na]^+$.

2.2 Precursor for radioiodination (reference ligand)

The synthesis was performed according to previously published methods (126, 199, 200).

Succinimidyl-4-iodobenzoate (I-BA-NHS): Under a nitrogen atmosphere, 500 mg (2.0 mmol, 1.0 eq.) 4-iodobenzoic acid was dissolved in 10 mL DCM, and after addition of 278 mg (2.4 mmol, 1.2 eq.) *N*-hydroxysuccinimide (NHS) and 374 mg (1.81 mmol, 0.9 eq.) dicyclohexyl carbodiimide (DCC), the suspension was stirred overnight. The precipitate was filtered off, and the filtrate was evaporated to dryness. The resulting solid was washed with a 1:1-mixture of DCM and hexane to yield the desired product (584 mg, 93%) as a white solid. Due to the limited detectability of the product in ESI-MS, a representative conjugate with H-Phe-O*t*Bu (1.0 eq.) was prepared in *N,N*-dimethylformamide (DMF) in the presence of *N,N*-diisopropylethylamine (DIPEA) (3.0 eq.) and characterized via MS. HPLC (40 to 100% B in 15 min): t_R = 10.6 min; K' = 5.6. Calculated monoisotopic mass for I-BA-Phe(O*t*Bu) ($C_{20}H_{22}INO_3$): 451.1 found: m/z = 396.1 $[M+H-t\text{Bu}]^+$.

Succinimidyl-4-tributylstannyl-benzoate ($SnBu_3$-BA-NHS): To a solution of 100 mg (0.29 mmol, 1.0 eq.) I-BA-NHS in 5 mL anhydrous toluene were added 234 µL (0.46 mmol, 1.6 eq.) hexabutylditin and 10.7 mg (9.1 µmol, 0.02 eq.) of the catalyst *tetrakis*(triphenylphosphine)palladium under a nitrogen atmosphere. The mixture was heated under reflux until the solution turned black (overnight). After cooling, the toluene was removed *in vacuo*, and the resulting oil was purified using silica gel flash chromatography (ethyl acetate/hexane: 3/7 (v/v)) to yield 78 mg (53%) as a colorless oil. TLC (ethyl acetate/hexane: 3/7): R_f = 0.46.

(4)

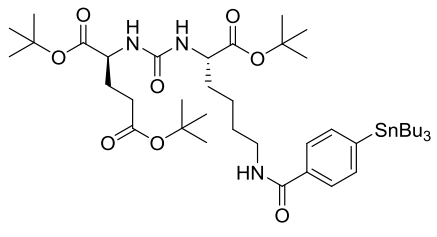

Chemical Formula: $C_{43}H_{75}N_3O_8Sn$
Molecular Weight: 880.78 $gmol^{-1}$

Di-*tert*-butyl (((S)-1-(*tert*-butoxy)-1-oxo-6-(4-(tributylstannyl)benzamido)hexan-2-yl)carbamoyl)-L-glutamate ($(SnBu_3\text{-BA})(O\textit{t}Bu)KuE(O\textit{t}Bu)_2$): In 2.0 mL DCM, 19.0 mg (0.039 mmol, 1.0 eq.) **3** were added to 26.3 µL (0.19 mmol, 4.8 eq.) TEA and 19.8 mg (0.39 mmol, 1.0 eq.) **5**. The mixture was stirred at rt for 4 h and then diluted with DCM. After washing with water, the organic phase was dried over Na_2SO_4, filtered and evaporated to dryness. **4** (30.8 mg, 90%) was obtained as a colorless oil. HPLC (10 to 90% B in 15 min): t_R = 23.8 min; K' = 13.9. Calculated monoisotopic mass ($C_{43}H_{75}N_3O_8Sn$): 880.8. 881.8, 882.8 found: m/z = 902.2/903.3/904.3 $[M+Na]^+$.

2.3 Small molecule PSMA inhibitors

(R1)

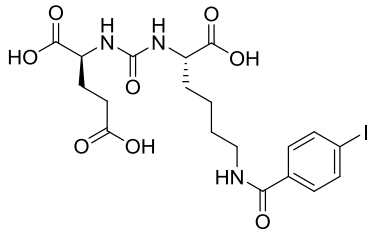

Chemical Formula: $C_{19}H_{24}IN_3O_8$
Molecular Weight: 549.31 gmol^{-1}

(((S)-1-carboxy-5-(4-iodobenzamido)pentyl)carbamoyl)-L-glutamic acid ((I-BA)KuE) (201): To a solution of 15.0 mg (0.031 mmol, 1.0 eq.) **3** in 2 mL DMF were added 11.4 mg (0.046 mmol, 1.5 eq.) 4-iodo-benzoic acid, 6.3 mg (0.046 mmol, 1.5 eq.) 1-hydroxy-7-azabenzotriazole (HOAt), 7.2 µL (0.046 mmol, 1.5 eq.) *N,N*-diisopropyl-carbodiimide (DIC) and 23.7 µL (0.138 mmol, 4.5 eq.) DIPEA. The yellow solution was stirred for 20 h, diluted with ethyl acetate and extracted with water. The organic layer was dried over Na_2SO_4, filtered and evaporated to dryness. For *t*Bu-deprotection, the crude product was dissolved in 200 µL TFA. After 30 min, the solvent was evaporated and the crude product was purified by HPLC (isocratic eluent: 18% B). HPLC (10 to 90% B in 15 min): t_R = 10.5 min; K' = 5.6. Calculated monoisotopic mass ($C_{19}H_{24}IN_3O_8$): 549.3 found: *m/z* = 550.0 $[M+H]^+$, 571.9 $[M+Na]^+$.

(R2)

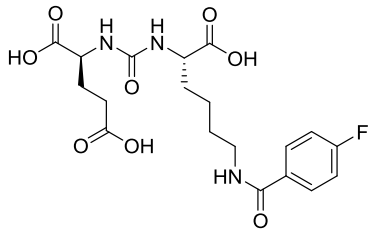

Chemical Formula:$C_{19}H_{24}FN_3O_8$
Molecular Weight: 441.41 gmol^{-1}

(((S)-1-carboxy-5-(4-fluorobenzamido)pentyl)carbamoyl)-L-glutamic acid ((F-BA)KuE) (201): In 2 mL DMF, 17.0 mg (0.035 mmol, 1.0 eq.) **3** were added to 7.4 mg (0.052 mmol, 1.5 eq.) 4-fluoro-benzoic acid, 7.2 mg (0.052 mmol, 1.5 eq.) HOAt, 8.1 µL (0.052 mmol, 1.5 eq.) DIC and 26.9 µL (0.157 mmol, 4.5 eq.) DIPEA. The yellow solution was stirred for 20 h, followed by extraction with water-ethyl acetate. The organic layer was evaporated to dryness and lyophilized. For *t*Bu-deprotection the crude product was dissolved in 200 µL TFA for a 30 min incubation and immediately dried. Purification was performed by HPLC (10% B isocratic). HPLC (10 to 90% B in 15 min): t_R = 9.5 min; K' = 5.8. Calculated monoisotopic mass ($C_{19}H_{24}FN_3O_8$): 441.2 found: *m/z* = 442.1 $[M+H]^+$, 464.0 $[M+Na]^+$.

(5)

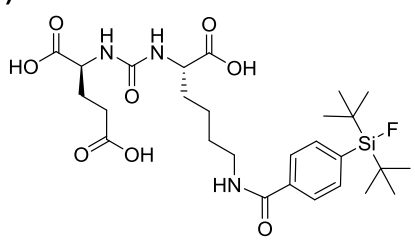

Chemical Formula: $C_{27}H_{42}FN_3O_8Si$
Molecular Weight: 583.72 gmol^{-1}

(SiFA-BA)KuE: To a solution of 15.0 mg (0.032 mmol, 1.0 eq.) **3** in 2 mL DMF was added 8.8 mg (0.046 mmol, 1.5 eq.) SiFA-BA (202), 6.3 mg (0.046 mmol, 1.5 eq.) HOAt, 7.2 µL (0.046 mmol, 1.5 eq.) DIC and 23.7 µL (0.138 mmol, 4.5 eq.) DIPEA. The yellow solution was stirred for 20 h, followed by extraction with brine-ethyl acetate. The organic layer was evaporated to dryness and lyophilized. For *t*Bu-deprotection the crude product was dissolved in 200 µL TFA for a 30 min incubation and purified by HPLC (37% B isocratic). HPLC (10 to 90% B in 15 min):

t_R = 14.7 min; K' = 9.5. Calculated monoisotopic mass ($C_{27}H_{42}FN_3O_8Si$): 583.3 found: m/z = 584.1 $[M+H]^+$, 606.0 $[M+Na]^+$.

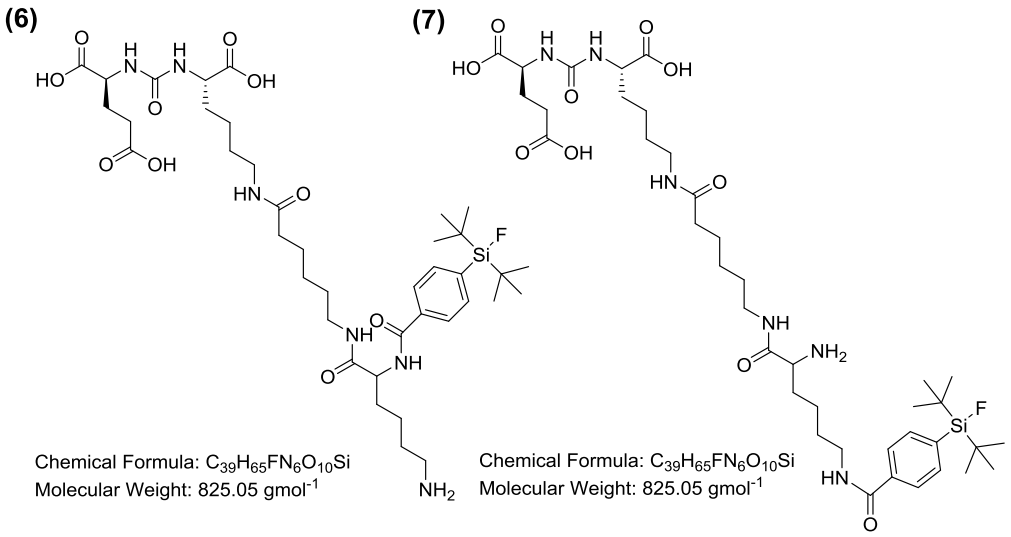

SiFA-BA-K-Ahx-KuE (6) and K(SiFA-BA)-Ahx-KuE (7): Fmoc-6-aminohexanoic acid (Fmoc-6-Ahx-OH) was coupled to tritylchloride polystyrene (TCP) resin according to a previously published method (203). Briefly, Fmoc-6-Ahx-OH (1.5 eq.) was dissolved in dry DCM, and DIPEA (1.25 eq) was added. Dry TCP-resin (1.0 eq. of tritylchloride groups, based on resin loading as given by the manufacturer) was suspended in this solution and stirred at rt for 5 min. Another 2.5 eq. DIPEA were added, and stirring was continued for 90 min. Then, 1.0 mL methanol per gram resin was added to cap unreacted tritylchloride groups. After 15 min the resin was filtered off, washed twice with DCM, DMF and methanol, respectively, and dried *in vacuo*. Final loading of resin-bound Fmoc-Ahx-OH was calculated using the following equation:

$$load\left[\frac{mmol}{g}\right] = \frac{(m_2 - m_1)\cdot 1000}{\left(MW - 36.461\frac{g}{mol}\right)\cdot m_2}$$

m_1 = mass of the dry TPC resin before coupling [g]

m_2 = mass of the dried resin after the coupling reaction [g]

MW = molecular weight of Fmoc-Ahx-OH [g/mol]

After Fmoc-deprotection (20% piperidine in *N*-methyl-pyrrolidon (NMP), 5 min and 15 min, respectively), the resin was washed eight times with NMP. Coupling of either Fmoc-Lys(Boc)-OH (**6**) or Boc-Lys(Fmoc)-OH (**7**) on resin-bound Ahx, followed by Fmoc-deprotection and coupling of SiFA-BA (1.5 eq.) was performed in DMF according to a standard Fmoc-protocol using 1.5 eq. of 1-hydroxybenzotriazole (HOBt) and *O*-(1H-

benzotriazol-1-yl)-*N,N,N',N'*-tetramethyluronium-tetrafluoroborate (TBTU) as coupling reagents and 4.5 eq. DIPEA as the base. After coupling of SiFA-BA, the resin was washed (8 × DMF, 3 × DCM), dried in a desiccator and the Boc-protected peptide was cleaved from the resin using DCM/acetic acid/trifluoroethanol (6/3/1; v/v/v). The solvent was evaporated and the crude product was reacted with 126 mg (0.26 mmol, 1.5 eq.) **3** using HOAt (1.5 eq.), DIC (1.5 eq.) and DIPEA (4.5 eq.) in 4 mL DMF overnight. After extraction with ethyl acetate and brine, the protection groups were cleaved by incubation in 3 mL TFA for 45 min at rt. The crude product was purified by HPLC (isocratic 30% B). HPLC (40 to 100% B in 15 min): t_R = 8.5 min; K' = 5.1. Calculated monoisotopic mass ($C_{27}H_{42}FN_3O_8Si$): 824.5 found: m/z = 825.3 $[M+H]^+$, 847.3 $[M+Na]^+$.

2.4 DUPA-Pep-based inhibitors

(8)

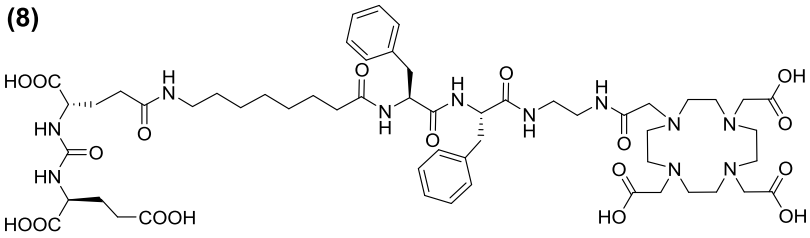

Chemical Formula: $C_{55}H_{81}N_{11}O_{18}$
Molecular Weight: 1184.29 $gmol^{-1}$

DUPA-Pep-DOTA was kindly provided by Prof. S. Reske (Ulm, Germany).

(9)

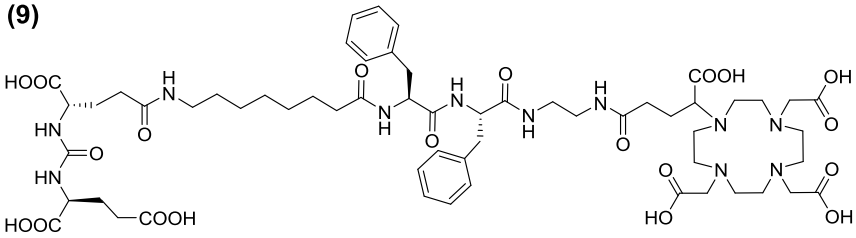

Chemical Formula: $C_{58}H_{85}N_{11}O_{20}$
Molecular Weight: 1256.36 $gmol^{-1}$

DUPA-Pep-DOTAGA: A solution of 10.0 mg (12.5 µmol, 1.0 eq.) DUPA-Pep (ABX, Radeberg, Germany) and 5.8 mg (12.5 µmol, 1.0 eq.) DOTAGA-anhydride in 1.0 mL DMF was added to 5.2 µL (37.6 µmol, 3.0 eq.) TEA. After 2 h at 70 °C, the solvent was evaporated *in vacuo* and the crude product was precipitated in diethyl ether before HPLC purification (isocratic 20% B). HPLC (25 to 55% B in 24 min): t_R = 17.2 min; K' = 10.5. Calculated monoisotopic mass ($C_{58}H_{85}N_{11}O_{20}$): 1,255.6 found: m/z = 1,256.4 $[M+H]^+$, 1,278.4 $[M+Na]^+$, 628.2 $[M+2H]^{2+}$.

(10)

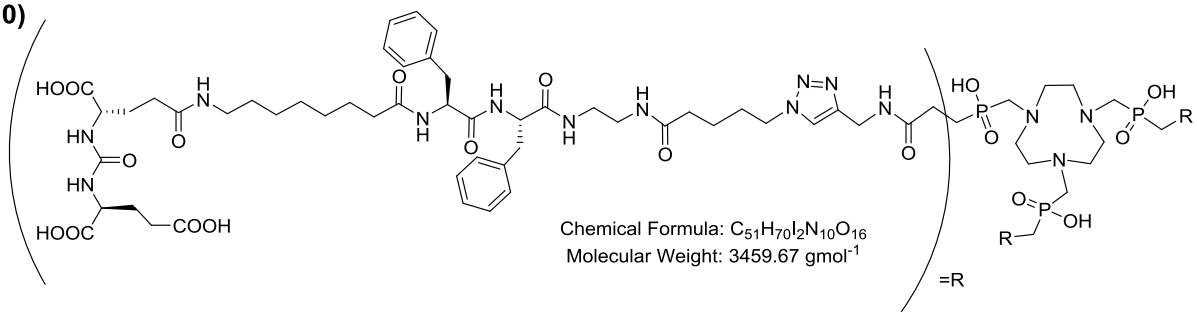

(DUPA-Pep-PA)$_3$-TRAP: To a solution of 5.2 mg (13.8 µmol, 1.1 eq.) O-(7-azabenzotriazol-1-yl)-*N,N,N′,N′*-tetramethyluronium hexafluorophosphate (HATU) in DMF was added 2.5 mg (17.5 µmol, 1.4 eq.) 5-azidopentanoic acid and 20 µL (15.1 mg, 117 µmol, 9.4 eq.) DIPEA in 100 µL DMF. The resulting yellow solution was stirred for 10 min at rt, and then added dropwise to a stirred solution of 10 mg (12.5 µmol, 1.0 eq.) DUPA-Pep (ABX, Radeberg, Germany) and 14 µL (10.6 mg, 82.0 µmol, 6.5 eq.) DIPEA in 200 µL DMF. The reaction mixture was stirred for another 60 min at rt, and then added dropwise to 25 mL diethyl ether. The precipitate was centrifuged and purified using HPLC. The azide-functionalized product (4.2 mg, 36%) was obtained as a white solid. Calculated monoisotopic mass ($C_{44}H_{62}N_{10}O_{12}$): 922.5 found: *m/z* = 623.6 $[M+H]^+$

The 3-aminopropyne functionalized TRAP (TRAP(proyne)$_3$) was prepared as described previously (190). To 6.8 mg (9.0 µmol, 1.0 eq.) TRAP(propyne)$_3$ was added 17.9 mg (90.0 µmol, 10.0 eq.) sodium ascorbate in 90 µL water and 27.3 mg (29.5 µmol, 3.3 eq.) azide-functionalized DUPA-Pep in 90 µL saturated $NaHCO_3$. After the addition of 2.2 mg (10.7 µmol, 1.2 eq.) $Cu(OAc)_2$ in 90 µL water the reaction mixture was stirred for 1 h, and then combined with a solution of 33.0 mg (109 µmol, 12 eq.) NOTA in 4 mL 1 µM hydrochloric acid (pH 3.0) and 2.5 mL ethanol and stirred for two days. The demetalation mixture was directly subjected to HPLC purification (39 – 45% B). Consecutive lyophilisation yielded the trimer **10** (9.4 mg, 30%) as a white solid. Calculated monoisotopic mass ($C_{159}H_{231}N_{36}O_{45}P_3$): 3,459.7 found: *m/z* = 1,730.8 $[M+2H^+]$, 1,154.0 $[M+3H^+]$.

^{nat}Ga-compounds: For the preparation of the ^{nat}Ga-complexes, equal volumes of a 2 mM solution of $Ga(NO_3)_3$ in water and a 2 mM solution of the respective PSMA inhibitor in water were mixed and heated to 40 °C for 30 min. After cooling, the $^{nat}Ga^{III}$-chelate formation was confirmed using HPLC and MS. The resulting 1 mM aqueous solutions of the respective ^{nat}Ga-complexes were then further diluted and used in the *in vitro* IC_{50} studies without further processing.

[^{nat}Ga]DUPA-Pep-DOTA ([^{nat}Ga]**8**) HPLC (25 to 55% B in 24 min): t_R = 17.4 min; *K′* = 10.6. Calculated monoisotopic mass ($C_{55}H_{78}N_{11}O_{18}Ga$): 1,249.48, 1,251.48 found: *m/z* = 1,250.6.1/1,252.4 $[M+H]^+$, 1,272.4/1,274.4 $[M+Na]^+$.

[^{nat}Ga]DUPA-Pep-DOTAGA ([^{nat}Ga]**9**) HPLC (25 to 55% B in 24 min): t_R = 17.4 min; *K'* = 10.6. Calculated monoisotopic mass ($C_{58}H_{82}N_{11}O_{20}Ga$): 1,321.50, 1,323.5 found: *m/z* = 1,322.1/1,324.1 $[M+H]^+$, 1,344.3/1,346.0 $[M+Na]^+$.

[^{nat}Ga] (DUPA-Pep-PA)$_3$-TRAP ([^{nat}Ga]**10**) HPLC (25 to 55% B in 24 min): t_R = 18.4 min; *K'* = 12.1. Calculated monoisotopic mass ($C_{159}H_{228}N_{36}O_{45}P_3Ga$): 3,525.7, 3,527.7 found: *m/z* = 1,763.8/1,764.6 $[M+2H]^{2+}$, 1,774.9/1,775,8 $[M+H+Na]^{2+}$.

2.5 Choice of chelator-peptide spacer-unit

(11)

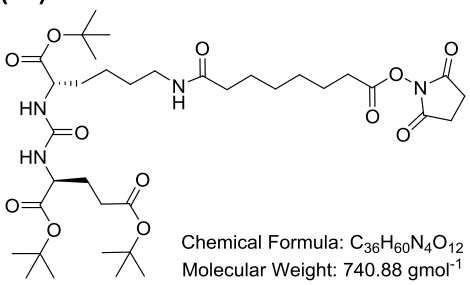

NHS-Sub-(O*t*Bu)KuE(O*t*Bu)$_2$ (204): A solution of 40.0 mg (0.08 mmol, 1.0 eq.) **3** in 500 µL DMF and 57 µL (0.41 mmol, 5.0 eq.) TEA were added dropwise (within 30 min) to a solution of 33.2 mg (0.09 mmol, 1.1 eq.) disuccinimidyl suberate (Sub(NHS)$_2$). After stirring for additional 2 h at rt, the reaction mixture was concentrated *in vacuo*, diluted with ethyl acetate and extracted with water (2 ×). The organic phase was dried over Na_2SO_4, filtered and evaporated to dryness. Due to sufficient purity of the crude product, it was used for the following reaction step without further purification. HPLC (10 to 90% B in 15 min): t_R = 16.9 min; *K'* = 8.4. Calculated monoisotopic mass ($C_{36}H_{60}N_4O_{12}$): 740.4 found: m/z = 741.2 $[M+H]^+$, 763.4 $[M+Na]^+$.

2.5.1 SPPS and resin-bound coupling of chelators

Fmoc-L-Phe-L-Phe-L-Lys(Boc) (Fmoc-FFK(Boc)) and Fmoc-D-Phe-D-Phe-D-Lys(Boc) (Fmoc-ffk(Boc)): Fmoc-Lys(Boc)-OH was coupled to TCP-resin as described for **6** and **7** in II.2.3. Assembly of the peptide sequence H_2N-Phe-Phe- on resin-bound Lys(Boc) was performed according to standard Fmoc-protocol using 1.5 eq. of HOBt and TBTU as coupling reagents and 4.5 eq. DIPEA as a base. After coupling of the last amino acid, the resin was washed, dried and stored in a desiccator until further functionalization.

Resin-bound coupling of chelating moiety: Fmoc-Phe-Phe-Lys(Boc)-TCP resin was allowed to preswell in NMP for 30 min. After cleavage of the *N*-terminal Fmoc-protecting group using 20% piperidine in NMP (v/v), the resin was washed eight times with NMP. The coupling of the respective chelators is described below. Cleavage from the resin (2 × 30 min) and concomitant *t*Bu-deprotection was performed using a mixture (v/v/v) of 95%

trifluoroacetic acid (TFA), 2.5% triisopropylsilane (TIPS) and 2.5% water. The combined product solutions were then concentrated, the crude peptide was precipitated using diethyl ether and was dried *in vacuo*. Due to sufficient purity of the crude products, they were used for the following reaction step without further purification.

DOTA-Phe-Phe-Lys (DOTA-FFK) (153): For 38 µmol of resin-bound peptide FFK(Boc), 33 mg (57 µmol, 1.5 eq.) DOTA-tris-*t*Bu-ester, 108 mg (0.28 mmol, 5.0 eq.) HATU and 87 µL (570 µmol, 15.0 eq.) DIPEA in NMP were added to the resin. After 72 h of shaking, the resin was washed with NMP and DCM. HPLC (10 to 90% B in 15 min): t_R = 8.2 min; *K'* = 4.1. Calculated monoisotopic mass ($C_{40}H_{58}N_8O_{11}$): 826.4 found: *m/z* = 827.3 $[M+H]^+$, 849.3 $[M+Na]^+$, 414.2 $[M+2H]^{2+}$.

DOTAGA-Phe-Phe-Lys (DOTAGA-FFK and DOTAGA-ffk): For 270 µmol resin-bound peptide, 190 mg (0.42 mmol, 1.5 eq.) DOTAGA-anhydride and 470 µL (2.7 mmol, 10.0 eq.) DIPEA in NMP were added to the resin. After 18 h of shaking, the resin was washed with NMP and DCM. HPLC (10 to 90% in 15 min): t_R = 10.6 min; *K'* = 5.6. Calculated monoisotopic mass ($C_{43}H_{62}N_8O_{13}$): 898.4 found: *m/z* = 899.4 $[M+H]^+$, 921.4 $[M+Na]^+$, 450.2 $[M+2H]^{2+}$.

NOPO-Phe-Phe-Lys (NOPO-FFK) and NOPO-Phe-Tyr-Lys (NOPO-FYK): For 34 µmol resin-bound peptide, 20 mg (34 µmol, 1.0 eq.) NOPO (189), 65 mg (0.17 mmol, 5.0 eq.) HATU and 59 µL (340 µmol, 10.0 eq.) DIPEA in NMP were added to the resin. After 18 h of shaking, the resin was washed with NMP and DCM.

NOPO-FFK: HPLC (10 to 90% B in 15 min): t_R = 8.6 min; *K'* = 5.1. Calculated monoisotopic mass ($C_{38}H_{62}N_7O_{13}P_3$): 917.4 found: *m/z* = 918.1 $[M+H]^+$, 940.2 $[M+Na]^+$, 459.6 $[M+2H]^{2+}$.

NOPO-FYK: HPLC (10 to 90% B in 15 min): t_R = 8.2 min; *K'* = 4.1. Calculated monoisotopic mass ($C_{43}H_{62}N_8O_{13}$): 933.4 found: *m/z* = 934.2 $[M+H]^+$, 956.2 $[M+Na]^+$.

2.5.2 Condensation of the chelator-conjugated peptides and the PSMA binding motif

(R4)

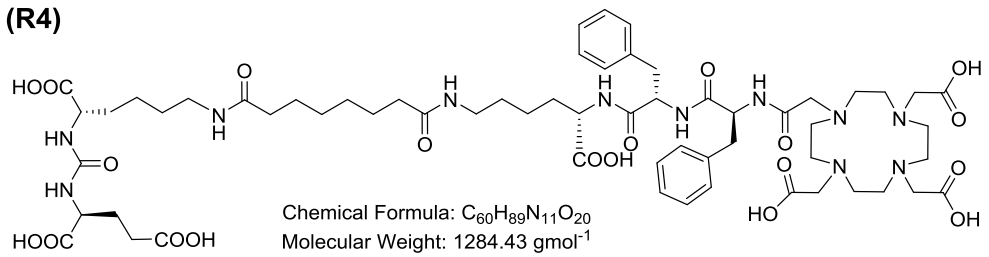

DOTA-FFK(Sub-KuE) (153): A solution of 15.0 mg (18 µmol, 1.0 eq.) DOTA-FFK and 13.1 µL (90 µmol, 5.0 eq.) TEA dissolved in 600 µL DMF was added to 13.1 mg (18 µmol, 1.0 eq.) **11** dissolved in 400 µL DMF. After stirring for 2 h at rt, the reaction mixture was evaporated to dryness. Subsequent removal of *t*Bu-protecting groups was carried out by dissolving the crude product in TFA and stirring for 40 min. After precipitation in diethyl ether, the crude product was dissolved in water and purified using preparative HPLC (25 to 40% B in 20 min).

R4: HPLC (10 to 90% B in 15 min): t_R = 10.3 min; *K'* = 5.4. Calculated monoisotopic mass ($C_{60}H_{89}N_{11}O_{20}$): 1,283.6 found: *m/z* = 1,284.5 $[M+H]^+$, 1,306.7 $[M+Na]^+$, 642.8 $[M+2H]^{2+}$.

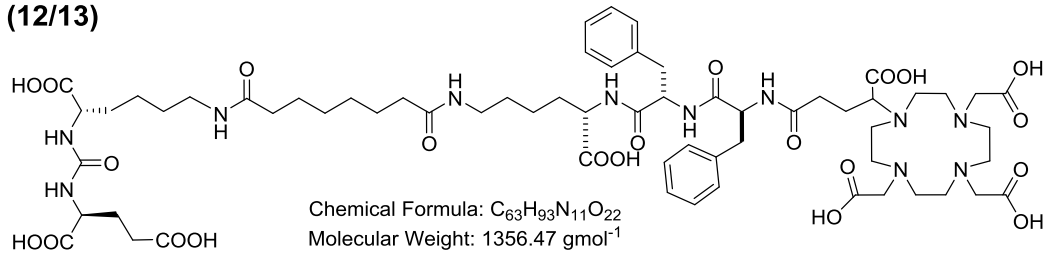

DOTAGA-FFK(Sub-KuE) (12) and DOTAGA-ffk(Sub-KuE) (13): Either 21.0 mg (30 µmol, 1.0 eq.) DOTAGA-FFK or DOTAGA-ffk were added to 21.1 µL (150 µmol, 5.0 eq.) TEA and 26.9 mg (30 µmol, 1.0 eq.) **11**. Deprotection was carried out using TFA and the crude products were purified via HPLC as described for **R4**.

12 and **13**: HPLC (10 to 90% B in 15 min): t_R = 9.7 min; *K'* = 4.1. Calculated monoisotopic mass ($C_{63}H_{93}N_{11}O_{22}$): 1,355.7 found: *m/z* = 1,356.2 $[M+H]^+$, 1,378.2 $[M+Na]^+$, 679.2 $[M+2H]^{2+}$.

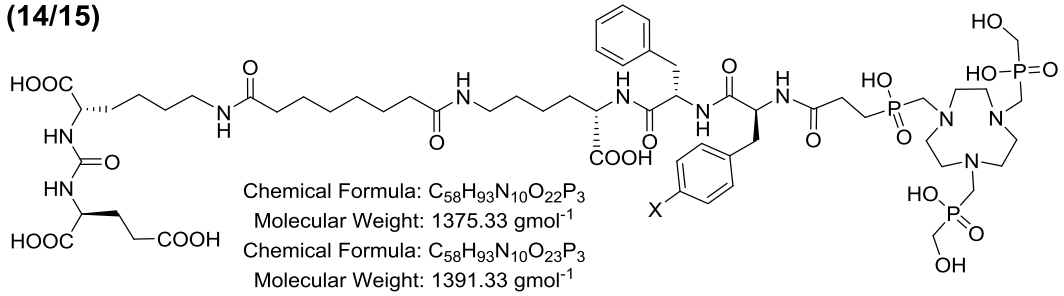

NOPO-FFK(Sub-KuE) (X = H; 14) and NOPO-FYK(Sub-KuE) (X = OH; 15): Either 7.9 mg (8.6 µmol, 1.0 eq.) NOPO-FFK or NOPO-FYK were added to 12.1 µL (86 µmol, 10.0 eq.) TEA and 7.7 mg (10.3 µmol, 1.2 eq.) **11**, deprotected using TFA and purified via HPLC as described for **R4**.

14: HPLC (10 to 90% B in 15 min): t_R = 9.5 min; *K'* = 5.8. Calculated monoisotopic mass ($C_{58}H_{93}N_{10}O_{22}P_3$): 1,374.6 found: *m/z* = 1,375.0 $[M+H]^+$, 1,397.9 $[M+Na]^+$, 688.6 $[M+2H]^{2+}$.

15: HPLC (10 to 90% B in 15 min): t_R = 9.7 min; *K'* = 4.11. Calculated monoisotopic mass ($C_{58}H_{93}N_{10}O_{23}P_3$): 1,390.6 found: *m/z* = 1,391.6 $[M+H]^+$.

2.5.3 Metal complexation

^{nat}Ga-compounds: The ^{nat}Ga-complexes were prepared as described in II.2.4. The reference ligand HBED-CC-Ahx-KuE (**R3**) was also included in the comparative study.

[^{nat}Ga]HBED-CC-Ahx-KuE ([^{nat}Ga]**R3)** HPLC (25 to 43% B in 15 min): t_R = 9.0 min; *K'* = 5.0. Calculated monoisotopic mass ($C_{44}H_{59}N_6O_{17}Ga$): 1,012.3, 1,014.3 found: *m/z* = 1,013.0/1,015.0 $[M+H]^+$, 1,035.0/1,037.0 $[M+Na]^+$.

[^{nat}Ga]DOTA-FFK(Sub-KuE) ([^{nat}Ga]**R4**) HPLC (20 to 60% B in 15 min): t_R = 11.6 min; *K'* = 6.3. Calculated monoisotopic mass ($C_{60}H_{86}N_{11}O_{20}Ga$): 1,349.5, 1,351.5 found: *m/z* = 1,350.3/1,352.4 $[M+H]^+$, 1,372.1/1,374.2 $[M+Na]^+$, 675.7/676.6 $[M+2H]^{2+}$.

[^{nat}Ga]DOTAGA-FFK(Sub-KuE) ([^{nat}Ga]**12**) HPLC (25 to 45% B in 15 min): t_R = 16.0 min; *K'* = 9.0. Calculated monoisotopic mass ($C_{63}H_{90}N_{11}O_{22}Ga$): 1,421.7, 1,423.7 found: *m/z* = 1,422.1/1,424.1 $[M+H]^+$, 710.6/711.6 $[M+2H]^{2+}$.

[^{nat}Ga]DOTAGA-ffk(Sub-KuE) ([^{nat}Ga]**13**) HPLC (25 to 55% B in 15 min): t_R = 12.1 min; *K'* = 7.6. Calculated monoisotopic mass ($C_{63}H_{90}N_{11}O_{22}Ga$): 1,421.7, 1,423.7 found: *m/z* = 1,422.6/1,424.5 $[M+H]^+$, 1,444.4/1,446.4 $[M+Na]^+$.

[^{nat}Ga]NOPO-FFK(Sub-KuE) ([^{nat}Ga]**14**) HPLC (25 to 55% B in 15 min): t_R = 11.5 min; *K'* = 7.2. Calculated monoisotopic mass ($C_{63}H_{90}N_{11}O_{22}Ga$): 1,441.7, 1,443.7 found: *m/z* = 1,442.5/1,444.5 $[M+H]^+$, 1,464.4/1,466.5 $[M+Na]^+$.

[^{nat}Ga]NOPO-FYK(Sub-KuE) ([^{nat}Ga]**15**) HPLC (25 to 55% B in 15 min): t_R = 12.1 min; *K'* = 7.6. Calculated monoisotopic mass ($C_{63}H_{90}N_{11}O_{23}Ga$): 1,457.5, 1,459.5 found: *m/z* = 1,458.3/1,460.3 $[M+H]^+$, 1,480.5/1,482.4 $[M+Na]^+$.

^{nat}Lu-compounds: The corresponding $^{nat}Lu^{III}$-complexes were prepared from a 2 mM aqueous solution of the PSMA inhibitor with a 2.5 molar excess of $LuCl_3$ (20 mM solution), heated to 95 °C for 30 min and evaluated as described for the $^{nat}Ga^{III}$-complexes.

[^{nat}Lu]DOTA-FFK(Sub-KuE) ([^{nat}Lu]**R4**) HPLC (25 to 45% B in 16 min): t_R = 14.1 min; *K'* = 9.1. Calculated monoisotopic mass ($C_{60}H_{86}N_{11}O_{20}Lu$): 1,455.6 found: *m/z* = 1,456.4 $[M+H]^+$, 1,478.5 $[M+Na]^+$.

[^{nat}Lu]DOTAGA-FFK(Sub-KuE) ([^{nat}Lu]**12**) HPLC (25 to 45% B in 16 min): t_R = 14.4 min; *K'* = 9.3. Calculated monoisotopic mass ($C_{63}H_{90}N_{11}O_{22}Lu$): 1,527.6 found: *m/z* = 1,528.4 $[M+H]^+$, 1,550.3 $[M+Na]^+$, 764.2 $[M+2H]^{2+}$.

[^{nat}Lu]DOTAGA-ffk(Sub-KuE) ([^{nat}Lu]**13**) HPLC (25 to 55% B in 15 min): t_R = 10.4 min; *K'* = 6.4. Calculated monoisotopic mass ($C_{63}H_{90}N_{11}O_{22}Lu$): 1,527.6 found: *m/z* = 1,528.1 $[M+H]^+$, 764.5 $[M+2H]^{2+}$.

2.6 Iodo-tyrosine derivatives

The phenylalanine residues of the FFK-derivatives (II.2.5) were (partially) substituted by 3-iodo-tyosines. Syntheses were performed as described in II.2.5, with an increased coupling time of 18 h for Fmoc-3-iodo-tyrosine.

(16)

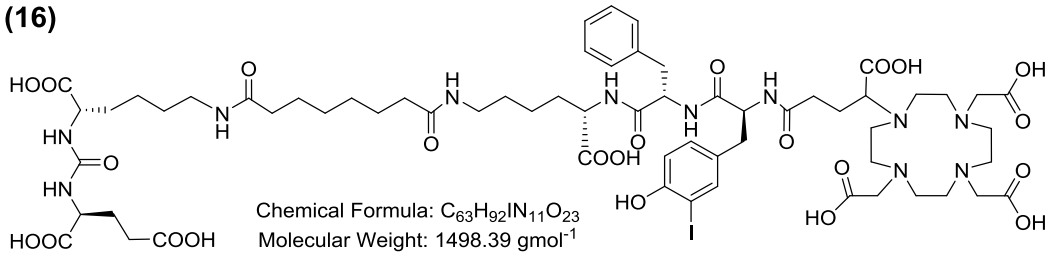

DOTAGA-(I-Y)FK(Sub-KuE) (**16**) HPLC (25 to 55% B in 15 min): t_R = 11.8 min, *K'* = 6.9. Calculated monoisotopic mass ($C_{63}H_{92}IN_{11}O_{23}$): 1,497.5 found: *m/z* = 1,498.7 $[M+H]^+$, 1,520.4 $[M+Na]^+$, 1536.4 $[M+K]^+$.

(17)

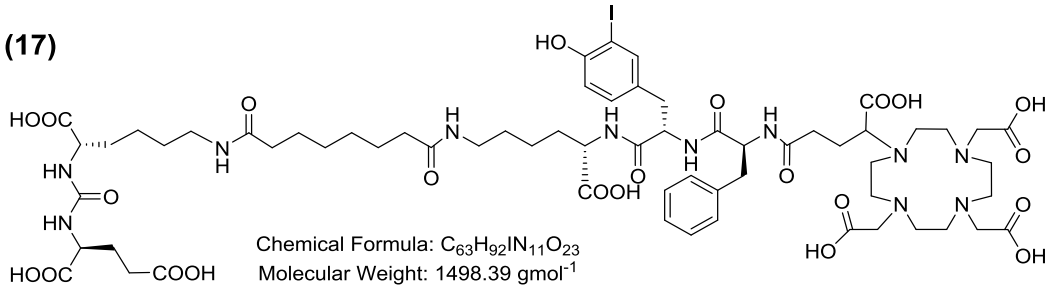

DOTAGA-F(I-Y)K(Sub-KuE) (**17**) HPLC (25 to 55% B in 15 min): t_R = 11.8 min, *K'* = 6.9. Calculated monoisotopic mass ($C_{63}H_{92}IN_{11}O_{23}$): 1,497.5 found: *m/z* = 1,498.7 $[M+H]^+$, 1,520.5 $[M+Na]^+$, 749.8 $[M+2H]^{2+}$.

(18)

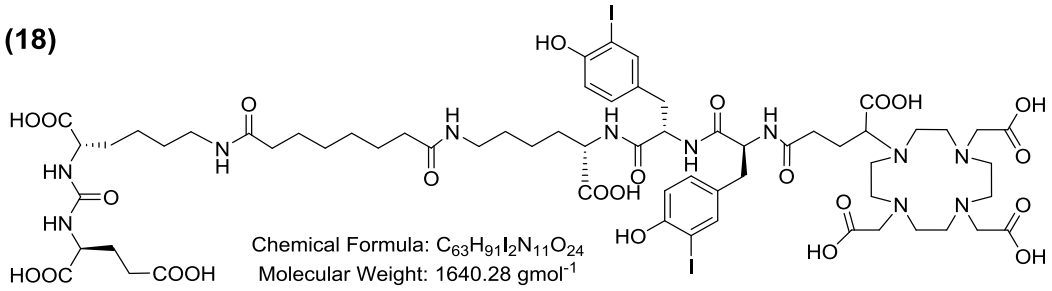

DOTAGA-(I-Y)(I-Y)K(Sub-KuE) (**18**) HPLC (25 to 55% B in 15 min): t_R = 12.2 min, *K'* = 7.1. Calculated monoisotopic mass ($C_{63}H_{91}I_2N_{11}O_{24}$): 1,639.4 found: *m/z* = 1,640.3 $[M+H]^+$, 1,662.1 $[M+Na]^+$.

(19)

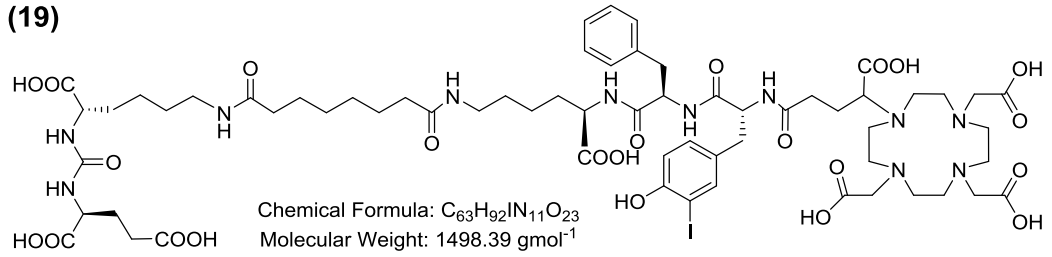

DOTAGA-(I-y)fk(Sub-KuE) (**19**) HPLC (25 to 55% B in 15 min): t_R = 11.5 min, *K'* = 5.4. Calculated monoisotopic mass ($C_{63}H_{92}IN_{11}O_{23}$): 1,497.5 found: *m/z* = 1,498.3 $[M+H]^+$, 1,520.1 $[M+Na]^+$.

^{nat}Ga-compounds: The ^{nat}Ga-complexes were prepared as described in II.2.4.

[^{nat}Ga]DOTAGA-(I-Y)FK(Sub-KuE) ([^{nat}Ga]**16**) HPLC (25 to 55% B in 15 min): t_R = 12.0 min; *K'* = 7.0. Calculated monoisotopic mass ($C_{63}H_{89}IN_{11}O_{23}Ga$): 1,563.4, 1,565.4 found: *m/z* = 1,564.8/1,566.8 $[M+H]^+$, 1,586.6/1,588.7 $[M+Na]^+$.

[^{nat}Ga]DOTAGA-F(I-Y)K(Sub-KuE) ([^{nat}Ga]**17**) HPLC (25 to 55% B in 15 min): t_R = 11.2 min; *K'* = 6.5. Calculated monoisotopic mass ($C_{63}H_{89}IN_{11}O_{23}Ga$): 1,563.4, 1,565.4 found: *m/z* = 1,564.5/1,566.6 $[M+H]^+$, 1,586.5/1,588.5 $[M+Na]^+$.

[^{nat}Ga]DOTAGA-(I-Y)(I-Y)K(Sub-KuE) ([^{nat}Ga]**18**) HPLC (25 to 55% B in 15 min): t_R = 12.6 min; *K'* = 6.3. Calculated monoisotopic mass ($C_{63}H_{88}I_2N_{11}O_{24}Ga$): 1,705.4, 1,707.4 found: *m/z* = 1,706.5/1,708.5 $[M+H]^+$, 1,728.4/1,730.5 $[M+Na]^+$.

[^{nat}Ga]DOTAGA-(I-y)fk(Sub-KuE) ([^{nat}Ga]**19**) HPLC (25 to 55% B in 15 min): t_R = 11.8 min, *K'* = 5.6. Calculated monoisotopic mass ($C_{63}H_{89}IN_{11}O_{23}Ga$): 1,563.4, 1,565.4 found: *m/z* = 782.7 $[M+2H]^{2+}$, 1,564.5/1,566.3 $[M+H]^+$.

2.7 “Kidney cleavable” sequence

(20/21)

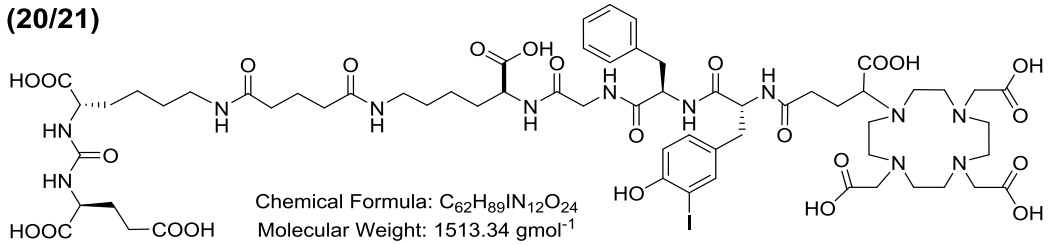

DOTAGA-peptides: The resin-bound synthesis of the DOTAGA-conjugated peptides (DOTAGA-iodo-D-Tyr-D-Phe-Gly-L-Lys and DOTAGA-iodo-D-Tyr-D-Phe-Gly-D-Lys) was performed according to the methods described in II.2.5. Coupling time for iodo-tyrosine was 18 h.

DOTAGA-(I-y)fGK: HPLC (20 to 70% B in 15 min): t_R = 7.9 min K' = 3.51. Calculated monoisotopic mass ($C_{45}H_{64}IN_9O_{15}$): 1,097.4 found: *m/z* = 1,098.3 $[M+H]^+$, 549.9 $[M+2H]^{2+}$.

DOTAGA-(I-y)fGk: HPLC (20 to 70% B in 15 min): t_R = 8.4 min K' = 2,36. Calculated monoisotopic mass ($C_{45}H_{64}IN_9O_{15}$): 1,097.4 found: *m/z* = 1,098.3 $[M+H]^+$, 549.9 $[M+2H]^{2+}$.

Glut-(O*t*Bu)KuE(O*t*Bu)$_2$: To a solution of 120.0 mg (0.25 mmol, 1.0 eq.) **3** and 33.7 mg (0.30 mmol, 1.2 eq.) glutaric anhydride in 5 mL chloroform was added 99.6 mL (0.74 mmol, 3.0 eq.) TEA and stirred for 24 h. The crude product was purified by HPLC (55 to 60% B in 20 min). HPLC (40 to 100% B in 15 min): t_R = 10.6 min K' = 4.3. Calculated monoisotopic mass ($C_{29}H_{51}N_3O_{10}$): 601.4 found: *m/z* = 624.2 $[M+Na]^+$.

DOTAGA-(I-y)fGK(Sub-KuE) (20) and DOTAGA-(I-y)fGk(Sub-KuE) (21): Both inhibitors were synthesized from the above mentioned fragments by preactivation of Glut-(O*t*Bu)KuE(O*t*Bu)$_2$ using 0.9 eq. HATU and 2.0 eq. DIPEA in DMF for 15 min, reaction with the peptides within 45 min, *t*Bu-deprotection in TFA, precipitation in diethyl ether and HPLC purification (23% B isocratic).

20: HPLC (25 to 55% B in 15 min): t_R = 10.6 min K' = 4.3. Calculated monoisotopic mass ($C_{62}H_{89}IN_{12}O_{24}$): 1,512.5 found: *m/z* = 1,513.3 $[M+H]^+$, 757,4 $[M+2H]^{2+}$.

21: HPLC (25 to 55% B in 15 min): t_R = 10.9 min K' = 4.5. Calculated monoisotopic mass ($C_{62}H_{89}IN_{12}O_{24}$): 1,512.5 found: *m/z* = 1,513.3 $[M+H]^+$, 757.4 $[M+2H]^{2+}$.

2.8 Fluorescent ligand

DOTAGA-K(Dde)-(I-Y)(I-Y)K: As described in II.2.5, the peptide DOTAGA-Lys(Dde)-3-iodo-Tyr-3-iodo-Tyr-Lys was synthesized via SPPS and subsequently purified by HPLC (20 to 50% in 20 min, t_R = 16.5 min). HPLC (10 to 90% B in 15 min): t_R = 10.9 min; K' = 5.7. Calculated monoisotopic mass ($C_{59}H_{84}I_2N_{10}O_{18}$): 1,474.4 found: m/z = 1,475.6 $[M+H]^+$.

Coupling to **11** and *t*Bu-deprotection was achieved as described in II.2.5. HPLC (10 to 90% B in 15 min): t_R = 13.3 min; K' = 7.3. Calculated monoisotopic mass ($C_{79}H_{115}I_2N_{13}O_{27}$): 1,931.6 found: m/z = 1,932.4 $[M+H]^+$.

DOTAGA-K-(I-Y)(I-Y)K(Sub-KuE): Dde-deprotection was accomplished in 3 mL DMF/hydrazine (99/1) for 25 min at rt. After precipitation in diethyl ether, the crude product was purified using HPLC (20 to 30% in 20 min, t_R = 19.5 min) yielding 5.7 mg (100 %) as a colorless solid. HPLC (10 to 90% B in 15 min): t_R = 9.7 min; K' = 4.4. Calculated monoisotopic mass ($C_{69}H_{103}I_2N_{13}O_{25}$): 1,767.5 found: m/z = 1,768.6 $[M+H]^+$.

(22)

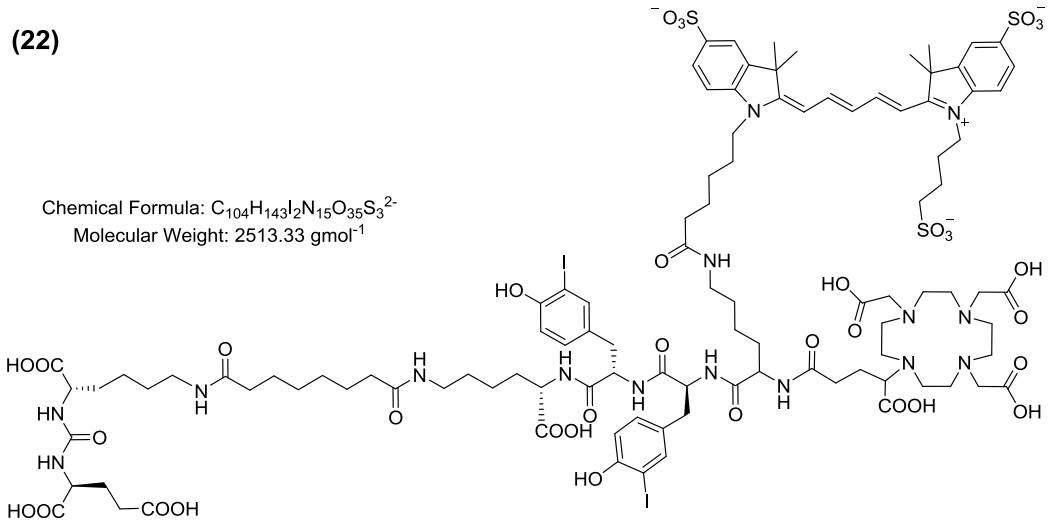

DOTAGA-K(Cy-5)-(I-Y)(I-Y)K(Sub-KuE): For condensation of the fluorescent dye Cy5 with the side chain amine of the DOTAGA-conjugated lysine in DOTAGA-K(I-Y)(I-Y)K(Sub-KuE) (1.0 eq.), the carboxylate of Cy5 (2.2 eq.) was preactivated using HATU (1.8 eq.) and TEA (10.0 eq.) in DMF and added to the peptide, which was dissolved in TEA (10.0 eq.) and DMF. After 2 h the crude product was purified using the analytical HPLC (35% B isocratic). HPLC (25 to 55% B in 15 min): t_R = 11.2 min; K' = 6.5. Calculated monoisotopic mass ($C_{104}H_{143}I_2N_{15}O_{35}S_3^{2-}$): 2,511.7 found: m/z = 1,258.8 $[M+2H]^{2+}$, 1,269.7 $[M+H+Na]^{2+}$, 1,281.1 $[M+2Na]^{2+}$.

[^{nat}Ga]DOTAGA-K(Cy5)-(I-Y)(I-Y)K(Sub-KuE) ([^{nat}Ga]**22**): Quantitative complexation was achieved as described in 2.4. HPLC (25 to 55% B in 15 min): t_R = 11.2 min; K' = 6.5. Calculated monoisotopic mass ($C_{104}H_{144}I_2N_{15}O_{35}S_3^{2-}Ga$): 2,580.7/2,582.7 found: *m/z* = 1,292.7/1,293.6 $[M+2H]^{2+}$, 1,303.8/1,304.5 $[M+H+Na]^{2+}$.

2.9 Lipophilic modification in the spacer

The peptide synthesis was performed as described in II.2.3. The TCP-resin bound lysine was coupled to the respective Fmoc-protected amino acids and after coupling of Fmoc-Tyr(*t*Bu)-OH and Fmoc-deprotection, the peptide was incubated with NMP/acetic anhydride/DIPEA (85/10/5) for 15 min. The resin was washed with NMP and DCM, before the peptides were cleaved from the resin using TFA/TIPS/water (95/2.5/2.5). The solvent was evaporated and the crude products were precipitated in diethyl ether. Coupling to **15** and final HPLC purification was performed as described in II.2.5.

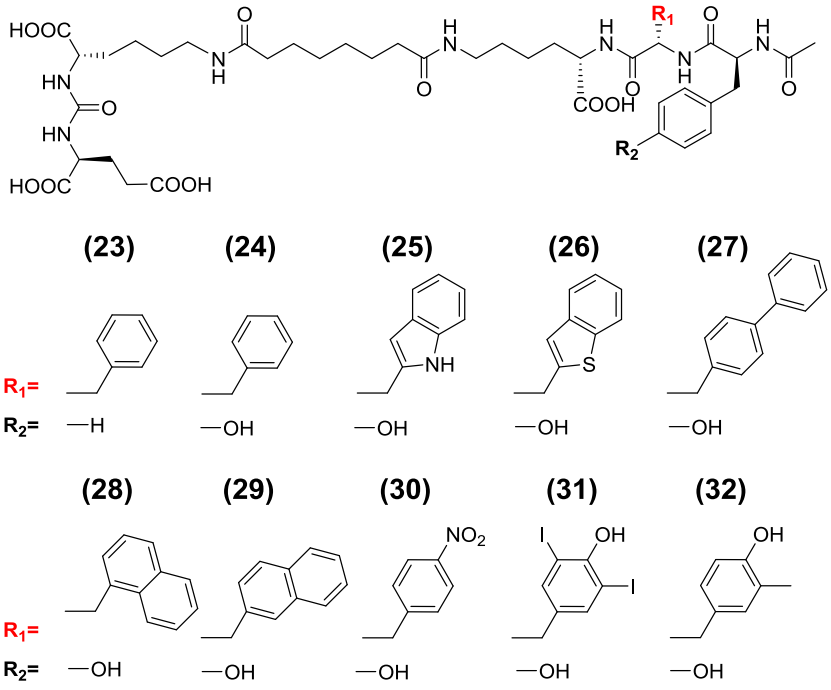

Ac-FFK(Sub-KuE) (**23**) HPLC (25 to 55% in 15 min): t_R = 13.3 min K' = 7.9. Calculated monoisotopic mass ($C_{50}H_{67}N_7O_{15}$) = 939.5 found: *m/z* = 940.9 $[M+H]^+$, 962.9 $[M+Na]^+$.

Ac-YFK(Sub-KuE) (**24**) HPLC (30 to 45% in 15 min): t_R = 7.4 min K' = 4.3. Calculated monoisotopic mass ($C_{46}H_{65}N_7O_{15}$) = 955.5 found: *m/z* = 956.5 $[M+H]^+$.

Ac-YWK(Sub-KuE) (**25**) HPLC (25 to 45% in 15 min): t_R = 15.3 min K' = 9.9. Calculated monoisotopic mass ($C_{48}H_{66}N_8O_{15}$) = 994.5 found: *m/z* = 995.3 $[M+H]^+$, 1,017.3 $[M+Na]^+$.

Ac-Y-(Benzothienyl-A)-K(Sub-KuE) (**26**) HPLC (35 to 45% in 15 min): t_R = 13.2 min *K'* = 9.2. Calculated monoisotopic mass ($C_{48}H_{65}N_7O_{15}S$) = 1,011.4 found: *m/z* = 1,012.4 $[M+H]^+$, 1,034.3 $[M+Na]^+$.

Ac-Y-(Biphenyl-A)-K(Sub-KuE) (**27**) HPLC (25 to 55% in 15 min): t_R = 15.4 min *K'* = 10.8. Calculated monoisotopic mass ($C_{52}H_{69}N_7O_{15}$) = 1,031.5 found: *m/z* = 1,032.3 $[M+H]^+$,1,054.2 $[M+Na]^+$.

Ac-Y-1-Nal-K(Sub-KuE) (**28**) HPLC (35 to 45% in 15 min): t_R = 13.6 min *K'* = 8.7. Calculated monoisotopic mass ($C_{50}H_{67}N_7O_{15}$) = 1,005.5 found: *m/z* = 1,006.4 $[M+H]^+$, 1,028.3 $[M+Na]^+$.

Ac-Y-2-Nal-K(Sub-KuE) (**29**) HPLC (35 to 45% in 15 min): t_R = 13.7 min *K'* = 8.8. Calculated monoisotopic mass ($C_{50}H_{67}N_7O_{15}$) = 1,005.5 found: *m/z* = 1,006.4 $[M+H]^+$,1,028.2 $[M+Na]^+$.

Ac-Y-(4-NO_2-F)-K(Sub-KuE) (**30**) HPLC (25 to 55% in 15 min): t_R = 11.8 min *K'* = 6.9. Calculated monoisotopic mass ($C_{50}H_{67}N_7O_{15}$) = 1,000.4 found: *m/z* = 1,001.6 $[M+H]^+$, 1,023.8 $[M+Na]^+$.

Ac-Y-(3,5-di-I-Y)-K(Sub-KuE) (**31**) HPLC (25 to 55% in 15 min): t_R = 14.8 min *K'* = 8.9. Calculated monoisotopic mass ($C_{50}H_{67}N_7O_{15}$) = 1,223.2 found: *m/z* = 1,224.6 $[M+H]^+$, 1,246.5 $[M+Na]^+$.

Ac-Y-(3-CH_3-Y)-K(Sub-KuE) (**32**) HPLC (25 to 55% in 15 min): t_R = 10.1 min *K'* = 5.7. Calculated monoisotopic mass ($C_{50}H_{67}N_7O_{15}$) = 985.5 found: *m/z* = 986.8 $[M+H]^+$, 1,008.9 $[M+Na]^+$.

2.10 NOTA-ligand

Di-pentafluorophenyl suberate (Sub(OPfp)$_2$): To a solution of 2.0 g (11.5 mmol, 1.0 eq.) suberic acid in 30 mL tetrahydrofurane, 2.8 mL (34.5 mmol, 3.0 eq.) pyridine, 7.1 mL (46.0 mmol, 4.0 eq.) DIC in 15 mL THF and 8.47 g (46.0 mmol, 4.0 eq.) pentafluorophenol in 15 mL tetrahydrofurane were successively added. Progress of the active ester formation was monitored using TLC (ethyl acetate/petroleum ether (55 - 65°C) (1/9)). After app. 2 h at rt, the reaction mixture was filtered, and the solvent was evaporated *in vacuo*. The crude product was purified via silica gel flash-chromatography using an eluent mixture of ethyl acetate/petroleum ether (1/9). The product was obtained as a yellow crystalline solid in 68% yield. Calculated monoisotopic mass for Sub(OPfp)$_2$ ($C_{20}H_{12}O_4F_{10}$) = 506.1 (Product is not detectable using ESI-MS).

(33)

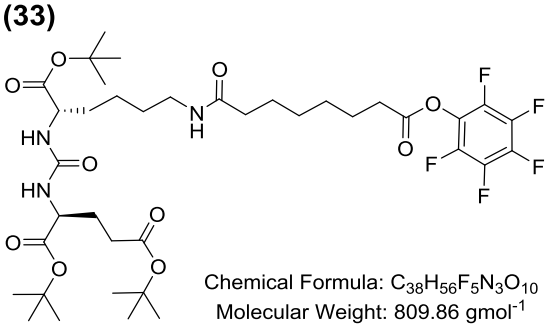

OPfp-Sub-(O*t*Bu)KuE(O*t*Bu)$_2$: To a solution of 400 mg (0.8 mmol, 1.0 eq.) **3** in 100 mL THF 274 µl (1.6 mmol, 2.0 eq.) DIPEA were added. This solution was added dropwise (within 30 min) to a solution of 1.6 g (3.2 mmol, 4.0 eq.) Sub(OPfp)$_2$. After stirring for an additional 2 h at rt, the reaction mixture was concentrated *in vacuo*, and the crude product was purified via silica gel flash-chromatography using a stepwise gradient of ethyl acetate in petroleum ether (55 - 65°C) of 10%, 50%, 90% and pure ethyl acetate (200 mL each). **33** was obtained as a yellowish oil in 58% yield. Calculated monoisotopic mass ($C_{38}H_{56}F_5N_3O_{10}$) = 809.4 found: *m/z* = 810.6 $[M+H]^+$, 832.4 $[M+Na]^+$.

(34)

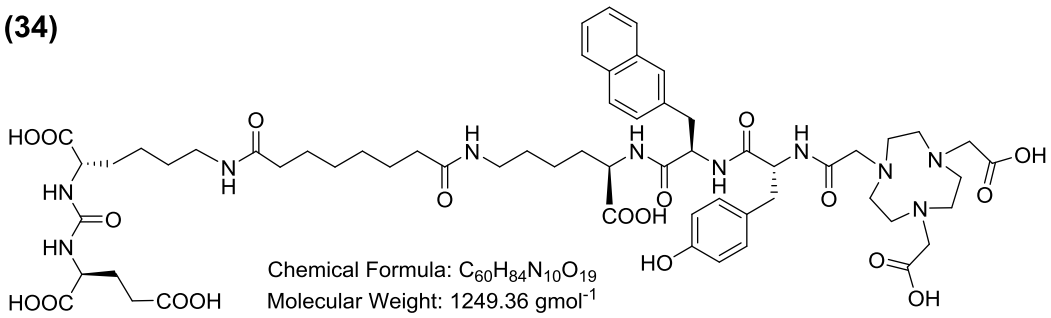

NOTA-y-nal-k(Sub-KuE): Peptide synthesis was performed as described in II.2.3 and coupling of NOTA was accomplished as described for DOTA in the literature (203). In brief, NOTA (3.0 eq.) was preactivated using NHS (3.75 eq.), 1-ethyl-3-(3-dimethylaminopropyl)carbodiimide (EDC) (3.75 eq.) and DIPEA (6.0 eq). After 15 min this solution was added to the peptide dissolved in DMF and stirred for another 20 min. The solvent was evaporated and the peptide was precipitated in diethyl ether, dried and Boc-deprotection was achieved by incubation in TFA for 30 min. The chelator-conjugated peptide was precipitated in diethyl ether and dried *in vacuo*. In contrast to the synthesis of the so far described PSMA inhibitors, conjugation of the Sub-KuE-motif was achieved by the pentafluorophenyl ester **34** instead of the NHS ester **11**. Reaction conditions of the peptide with **34** were similar as described in II.2.5. HPLC (Phenomenex Luna C18 column, 21% isocratic): t_R = 15.6 min K' = 10.1. Calculated monoisotopic mass ($C_{60}H_{84}N_{10}O_{19}$) = 1,248.5914 found: *m/z* = 1,249.5859 $[M+H]^+$.

Metal complexes of 34:

[Al]NOTA-y-nal-k(Sub-KuE) ([Al]**34**): For Al^{III}-complexation 10 µL of a 10 mM aqueous solution of **39** was added to 10 µL of a 20 mM $AlCl_3$ solution (pH 3.95) and 30 µL NaOAc buffer pH 3.95 and heated to 105 °C for 15 min. HPLC (25 to 55% in 15 min): t_R = 10.9 min *K'* = 6.3. Calculated monoisotopic mass ($C_{60}H_{82}N_{10}O_{19}Al^+$) = 1,273.6 found: *m/z* = 1,273.6 $[M]^+$.

[AlF]NOTA-y-nal-k(Sub-KuE) ([AlF]**34**): A 2.0 mM solution of **34** (2.3 eq.) was added to 0.5 eq. $AlCl_3$ (in 2 mM NaOAc pH 4.5) and 1.0 eq. NaF (in 2 mM NaOAc pH 4.5) resulting in pH 4 (150). The reaction mixture was heated to 105 °C for 0.5 h and purified using HPLC (Phenomenex Synergi 4u Max RP column, 1 mL/min, 17 - 27% B in 1 h). HPLC (Luna C18 column, 21% B isocratic): t_R = 11.3 min *K'* = 7.1. Calculated monoisotopic mass ($C_{60}H_{82}N_{10}O_{19}AlF$) = 1,292.5557 found: *m/z* = 1,293.5555 $[M+H]^+$.

[^{nat}Ga]NOTA-y-nal-k(Sub-KuE) ([^{nat}Ga]**34**): A 2.0 mM $Ga(NO_3)_3$ solution was added to a 2.0 mM solution of **34** and heated to 100 °C for 5 min. HPLC (Luna C18 column 21% B isocratic): t_R = 21.1 min *K'* = 13.1. Calculated monoisotopic mass ($C_{60}H_{82}N_{10}O_{19}Ga$) = 1,315.5014, 1,317.5005 found: *m/z* = 1,315.4934/1,317.4911 $[M]^+$.

[^{nat}Cu]NOTA-y-nal-k(Sub-KuE) ([^{nat}Cu]**34**): A 3 mM solution of $Cu(OAc)_2$ (100 µL) was added to 100 µL 2 mM **34** and heated to 95 °C for 30 min. HPLC (Luna C18 column 21% B isocratic): t_R = 8.2 min *K'* = 5.8. Calculated monoisotopic mass ($C_{60}H_{83}N_{10}O_{19}Cu$) = 1,309.5054, 1,310.5087, 1,311.5036 found: *m/z* = 1,310.5077/1,311.5024/1,312.5052 $[M+H]^+$.

2.11 Addressing of the S1-accessory lipophilic pocket

(35)

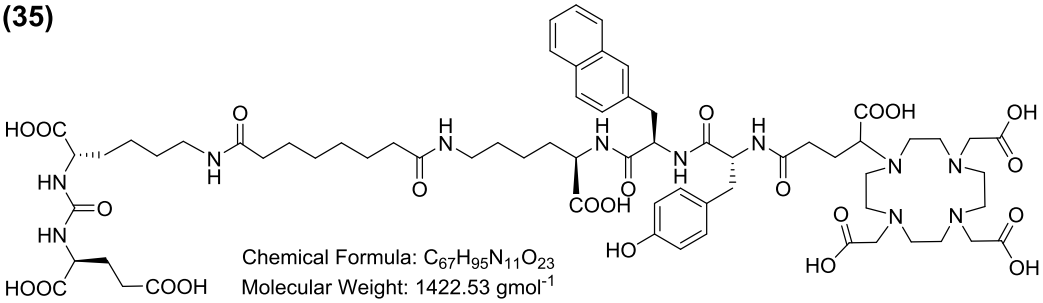

DOTAGA-y-nal-k(Sub-KuE): Peptide synthesis, chelator conjugation and purification of DOTAGA-y-nal-k was performed as described in II.2.5, the fragment condensation with the KuE-motif was performed using the pentafluorophenyl ester **33** as described in II.2.10.

DOTAGA-y-nal-k: HPLC (20 to 70% B in 15 min): t_R = 10.7 min *K'* = 4.13. Calculated monoisotopic mass ($C_{47}H_{64}N_8O_{14}$) = 964.5 found: *m/z* = 965.8 $[M+H]^+$, 987.8 $[M+Na]^+$.

35: HPLC (25 to 55% B in 15 min.): t_R = 12.5 min *K'* = 6.14. Calculated monoisotopic mass ($C_{67}H_{95}N_{11}O_{23}$) = 1,421.7 found: *m/z* = 1,422.8 $[M+H]^+$, 712.1 $[M+2H]^{2+}$.

(36)

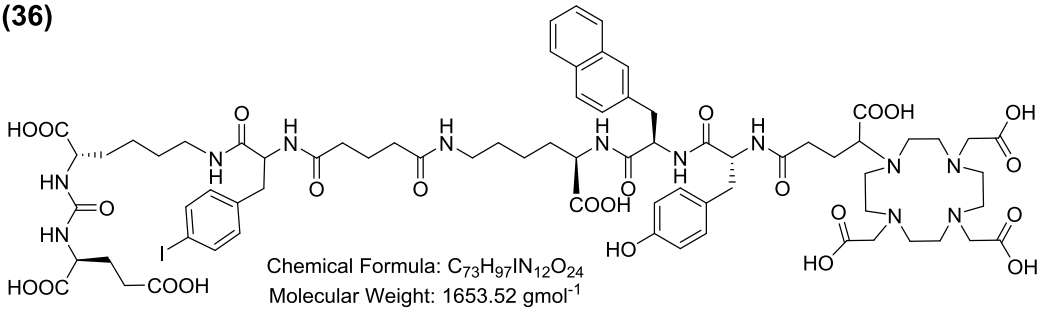

Di-pentafluorophenyl glutarate (Glut(OPfp)$_2$): To 2.0 g (15.1 mmol, 1.0 eq.) glutaric acid in 15 mL THF was added 3.7 mL (45.4 mmol, 3.0 eq.) pyridine, 9.5 mL (60.5 mmol, 4.0 eq.) DIC in 10 mL THF and 11.1 g (60.5 mmol, 4.0 eq.) pentafluorophenol in 10 mL THF. After 2 h the solvent was removed *in vacuo*, the crude dissolved in petrol ether was filtered and purified using silica gel flash chromatography (petrol ether/ethyl acetate = 95/5) yielding 6.1 g (87%) of a white crystalline solid. HPLC (10 to 100% B in 15 min): t_R = 17.5 min *K'* = 7.75. Calculated monoisotopic mass ($C_{19}H_{36}N_4O_6$) = 416.3 found: *m/z* = 417.1 $[M+H]^+$.

(I-f)-(O*t*Bu)KuE(O*t*Bu)$_2$: A solution of 0.5 g (0.97 mmol, 1.2 eq.) Fmoc-D-4-iodo-Phe, 0.2 g (1.22 mmol, 1.5 eq.) HOAt, 0.2 mL (0.16 g, 1.22 mmol, 1.5 eq.) DIC and 0.6 mL (0.47 g, 3.65 mmol, 4.5 eq.) DIPEA in 15 mL THF was stirred at rt for 1 h. After addition of 395 mg (0.81 mmol, 1.0 eq.) **3** in 5 mL THF the reaction mixture was stirred overnight. Water (20 mL) was added and extracted with 25 mL ethyl acetate (3 ×), followed by 20 mL H_2O (3 ×) and 25 mL brine. The organic phase was dried over $MgSO_4$ and the solvent was evaporated *in vacuo* yielding 2.0 g (> 100%) Fmoc-(I-f)-(O*t*Bu)KuE(O*t*Bu)$_2$ as a white solid, which was dissolved in 25.0 mL DMF and 5.0 mL piperidine was added and stirred for 2 h. The crude product was purified using HPLC (58% B isocratic). HPLC (10 to 90%): t_R = 15.6 min. *K'* = 8.2. Calculated monoisotopic mass ($C_{33}H_{53}IN_4O_8$): 760.3 found: *m/z* = 761.4 $[M+H]^+$, 783.4 $[M+Na]^+$, 799.4 $[M+K]^+$, 593.3 [M-3 *t*Bu +H]$^+$, 649.3 [M-2 *t*Bu +H]$^+$, 705.3 [M- *t*Bu +H]$^+$.

OPfp-Glut-(I-f)-(O*t*Bu)KuE(O*t*Bu)$_2$: At 0 °C 270 mg (0.35 mmol, 1.0 eq.) (I-f)-(O*t*Bu)KuE(O*t*Bu)$_2$ and 122 µL (0.71 mmol, 2.0 eq.) DIPEA in 20 mL THF were slowly added to 660 mg (1.42 mmol, 4.0 eq.) Glut(OPfp)$_2$ dissolved in 10 mL THF. After 2 h at rt, the solvent was removed *in vacuo* and the crude product was purified using silica gel flash chromatography (petrol ether/ethyl acetate: 10/1→1/10) yielding 143 mg (39%). HPLC (10 to

90% B in 15 min): t_R = 18.0 min *K'* = 9.6. Calculated monoisotopic mass ($C_{44}H_{58}F_5IN_4O_{11}$): 1,040.3 found: *m/z* = 1,041.2 $[M+H]^+$, 1,063.6 $[M+Na]^+$.

DOTAGA-y-nal-k(Glut-(I-f)-KuE) (36): A solution of 21.6 mg (0.021 mmol, 1.0 eq.) OPfp-Glut-(I-f)-(O*t*Bu)KuE(O*t*Bu)$_2$ in DMF was added to 22.3 mg (0.021 mmol, 1.0 eq) DOTAGA-y-nal-k and 14.5 µL (0.104 mmol, 5.0 eq.) TEA and stirred for 3.5 h. Deprotection of *t*Bu-esters was achieved in 1.0 mL TFA within 45 min and the crude was precipitated in diethyl ether and purified by HPLC (35% B isocratic). HPLC (35 to 60%): t_R = 10.5 min *K'* = 5.2. Calculated monoisotopic mass ($C_{73}H_{97}IN_{12}O_{24}$): 1,652.6 found: *m/z* = 1,654.9 $[M+H]^+$, 1,676.0 $[M+Na]^+$, 827.7 $[M+2H]^{2+}$.

Metal complexation: The nat. gallium was complexed as described in II.2.4 and nat. lutetium complexation is described in II.2.5.

[^{nat}Ga]DOTAGA-y-nal-k(Sub-KuE) ([^{nat}Ga]**35**) HPLC (25 to 55% B in 15 min): t_R = 10.8 min; *K'* = 8.0. Calculated monoisotopic mass ($C_{67}H_{92}N_{11}O_{23}Ga$): 1,487.6/1,489.6 found: *m/z* = 1,489.0/1,490.9 $[M+H]^+$, 1510.9/1512.9 $[M+Na]^+$, 746.1 $[M+2H]^+$.

[^{nat}Lu]DOTAGA-y-nal-k(Sub-KuE) ([^{nat}Lu]**35**) HPLC (25 to 55% B in 15 min): t_R = 11.6 min; *K'* = 8.7. Calculated monoisotopic mass ($C_{67}H_{92}N_{11}O_{23}Lu$): 1,593.6 found: *m/z* = 1,595.0 $[M+H]^+$, 1,616.8 $[M+Na]^+$, 798.2 $[M+2H]^+$.

[^{nat}Ga]DOTAGA-y-nal-k(Glut-(I-f)-KuE) ([^{nat}Ga]**36**) HPLC (25 to 55% B in 15 min): t_R = 11.8 min; *K'* = 5.6. Calculated monoisotopic mass ($C_{73}H_{94}IN_{12}O_{24}Ga$): 1,718.5, 1,720.5 found: *m/z* = 1,719.4/1,721.5 $[M+H]^+$, 1,740.5/1,742.6 $[M+Na]^+$, 861.4 $[M+2H]^+$.

[^{nat}Lu]DOTAGA-y-nal-k(Glut-(I-f)-KuE) ([^{nat}Lu]**36**) HPLC (25 to 55% B in 15 min): t_R = 10.6 min; *K'* = 4.9. Calculated monoisotopic mass ($C_{73}H_{94}IN_{12}O_{24}Lu$): 1,825.5 found: *m/z* = 1,826.5 $[M+H]^+$, 1,848.5 $[M+Na]^+$, 913.8 $[M+2H]^+$.

3 RADIOLABELING

3.1 Radioiodination ([^{125}I]NaI)

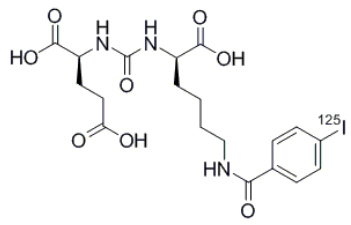

Chemical Formula: $C_{19}H_{24}{}^{125}IN_3O_8$
Molecular Weight: 547.31 gmol^{-1}

([^{125}I]I-BA)KuE ([^{125}I]R1): Peracetic acid was prepared by mixing 130 µL of H_2O_2 (30%) and 50 µL of acetic acid. After a 2 h incubation period, 20 µL peracetic acid solution and 5.0 µL (21.0 MBq) [^{125}I]NaI (74 GBq/µmol, 3.1 GBq/mL 40 mM NaOH, Hartmann Analytic, Braunschweig, Germany) were added to a solution of ~0.1 mg **6** in 20 µL acetonitrile/acetic acid (1/1) and incubated at rt for 10 min. The product was diluted with 10 mL of water and loaded onto a C18 Sep Pak Plus cartridge, which had been preconditioned with 10 mL of methanol and rinsed with 10 mL of water. The cartridge was then washed with 10 mL water, and the product was eluted in 300 - 500 µL fractions with a 1:1-mix (v/v) of ethanol/ acetonitrile (2.0 mL). The radioactive fractions were evaporated to dryness and the residue was dissolved in 200 µL TFA. After 30 min, the solvent was evaporated *in vacuo*. The crude product was dissolved in water/acetonitrile (9/1) and isolated from unlabeled tributyltin-precursor by HPLC (20 to 40% B in 20 min) to afford the desired product (10.9 MBq). HPLC (20 to 40% in 20 min, 220 nm): t_R = 13.0 min, *K'* = 6.22.

[^{125}I]15: NOPO-FYK(Sub-KuE) (**20**) was radioiodinated applying the Iodogen-method as described previously (203, 205, 206). In brief, app. 0.1 mg **20** in 200 µL phosphate-buffered saline (PBS) was incubated with 30 µg Iodogen (1,3,4,6-tetrachloro-3R,6R-diphenylglycoluril, Pierce, Rockford, IL) in a coated Eppendorf cap and [^{125}I]NaI within 20 min at rt. After HPLC purification (same gradient as used for [^{125}I]**7**) [^{125}I]**20** was obtained, diluted and used in cell experiments and for lipophilicity determination.

3.2 ^{68}Ga^{III}-labeling

A 1.25 mL fraction of ^{68}Ge/^{68}Ga generator (iTHEMBA Labs, South Africa) eluate (1 M HCl) was loaded onto a self-filled cartridge containing 300 mg SCX material (Bond Elut-SCX, Varian). The cartridge was then washed with 1.0 mL water and purged with air. The ^{68}Ga^{3+} was eluted with 0.5 mL 5.0 M NaCl and 90 - 140 µL 2.7 M 2-(4-(2-hydroxyethyl)-1-piperazinyl)-ethanesulfonic acid (HEPES) was added (pH 2 - 4.5). That solution was mixed with the precursor (3.0 nmol in 10 µL) and heated at 95 °C for 5 min. After cooling, labeling efficiency and radiochemicial purity were determined using Radio-TLC (0.1 M sodium citrate buffer or 0.06 M ammonium acetate/methanol (1/1), respectively) and Radio-HPLC.

Radiochemical purity of all ^{68}Ga-labeled conjugates was ≥ 95%. Therefore the tracers were diluted and used for *in vitro* experiments without further purification.

Tracers for *in vivo* use were prepared in GMP-compliant procedure using 5.0 nmol of precursor in a fully automated synthesis module (GRP, Scintomics GmbH, Germany) similarly to the procedure described previously (190). For animal studies, the ethanol for eluting the labeled tracer from a SPE cartridge was evaporated *in vacuo*.

Tracers for human application were labeled with $^{68}Ga^{III}$ using an automated synthesis module (GRP, Scintomics, Germany) by adapting the procedure as described previously (190, 207). In brief, 25 µg of HBED-CC-Ahx-KuE or **24** were dissolved in 3 mL 1.0 M HEPES buffer for labeling with $^{68}Ga^{III}$ and incubated at 95 °C for 12 min, followed by a purification step using a Waters SepPak C18 light cartridge.

3.3 $^{111}In^{III}$-labeling

[^{111}In]R3: Labeling was optimized using 1.0 MBq [^{111}In]$InCl_3$ (Mallinckrodt, St. Louis, USA) at rt in HEPES, citrate or NaOH at pH 3, 4, 5, 6, 7 and 8 (208-212). Complexation efficiencies with increasing peptide amounts were determined by Radio-TLC (citrate buffer or acetate/methanol (1/1)).

[^{111}In]19: To a solution of 400 - 500 µL [^{111}In]$InCl_3$ (246 - 378 MBq: 1 day before calibration; A_s > 205 GBq/µmol on the day of calibration, Mallinckrodt Pharmaceuticals, Dublin, Ireland) was added 7 µL 2 mM **24** (14 nmol, 21 µg) and the pH was adjusted to 5.3 using 0.6 mL aqueous NaOAc (0.15 M, pH 5.7) before heating for 25 min to 95 °C. Reaction yield was determined via Radio-TLC being > 99%. The reaction mixture was loaded onto a Waters Sep Pak C18 light cartridge (preconditioned with 5 mL ethanol followed by 5 mL water), washed with 5 mL water, and eluted in fractions of app. 50 µL using ethanol (0.5% acetic acid). The activity containing fractions (2 - 4) were diluted with 8 mL PBS and after sterile filtration applied in patients. Radio-TLC (purity > 98%), Radio-HPLC (Nucleosil-column, 1 mL/min, activity detector settings ^{123}I, 10 to 45% B in 15 min): t_R = 16.8 min, pH 6.5 - 7, γ-counter-half-life measurement (2 × on the day of synthesis and one week later) and γ-spectrum determination.

3.4 $^{177}Lu^{III}$-labeling

DOTAGA-conjugated PSMA inhibitors: To a 0.1 mM aqueous solution of DOTAGA-conjugated peptide (0.66 nmol) was added 25 MBq [^{177}Lu]$LuCl_3$ (170 GBq/µmol, 17 GBq/mL 0.05 M HCl, IDB Radiopharmacy bv). The pH was adjusted to pH 5 by the addition of app. 150 µL 0.1 M NH_4OAc solution. After 45 min at 95 °C the labeling efficiency was examined by Radio-TLC and HPLC.

[^{177}Lu]19: [^{177}Lu]**19** for clinical use was prepared after incubation of 150 - 200 µg **19** with 6 - 8 GBq [^{177}Lu]$LuCl_3$ (ITG, Garching, Germany) at 90 °C for 30 min in 800 µL 0.4 M NaOAc (pH 5.5). To this buffer, 5 - 10 mg of gentisic acid was added to prevent radiolysis. The reaction solutions were diluted with saline and after sterile filtration, a sample was taken for quality control (radio-HPLC, radio-TLC, pH, LAL, sterility testing, retention sample).

3.5 Complexation of $[Al^{18}F]^{2+}$

Radiolabeling using the $Al^{18}F$-method was achieved by combination of several literature methods (150, 213, 214). The $^{18}F^-$ (Cyclotek (Aust) Pty Ltd, Bundoora, VIC, Australia) was trapped on a Chromafix PS-HCO_3^- cartridge (Macherey-Nagel GmbH & Co KG, Düren, Germany). After washing with 3 mL of trace select water and purging with air, the activity was eluted dropwise with 0.4 M $KHCO_3$. The second fraction, containing approximately 25 µL and 40% of the activity (200 - 400 MBq), was used for labeling. After addition of 10 µL aq. $AlCl_3$ solution (1.0 mM; 10 nmol), 10 µL aq. NOTA-ligand **34** (2.0 mM; 20 nmol) and 40 µL DMSO, the pH was adjusted to 4.5 with 4 µL acetic acid. The reaction mixture was heated to 105 °C for 15 min and finally diluted with 400 µL 0.5 M NaOAc. Purification was performed with HPLC or cartridge. HPLC (Phenomenex Luna C18 column), 1 mL/min, 21% B isocratic, t_R = 12 min. Cartridge purification: A Waters SepPak Vac C18 cartridge was preconditioned with 1 mL ethanol, followed by 2 mL water. After applying the crude product, the cartridge was washed with 10 mL water and purged with air. The product was eluted with 0.3 mL ethanol and diluted with 0.7 mL saline before analysis.

3.6 $^{64}Cu^{II}$-labeling

For quantitative labeling of NOTA-ligand **34** with n.c.a. [^{64}Cu]$CuCl_2$ (74 MBq in 200 µL 0.02 M HCl, pH 1.7), 10 nmol (10 µL of a 1 mM solution) **34** was buffered to pH 6.5 using 100 µL 0.4 M NH_4OAc (pH 7 - 8) and heated to 100 °C for 10 min. Cartridge purification was performed as described for $[AlF]^{2+}$ complexation of **34**.

4 DETERMINATION OF LIPOPHILICITY AND PLASMA-PROTEIN BINDING

log$P_{(o/w)}$: To a solution of 0.5 - 1 MBq of radiolabeled peptide in 500 µL PBS (pH 7.4), 500 µL n-octanol were added (n = 6). Vials were vortexed vigorously for 3 min. To achieve quantitative phase separation, the vials were centrifuged at 6000 × g for 5 min in a Biofuge 15 (Heraeus Sepatech, Osterode, Germany). The activity concentrations in 100 µL-samples of both the aqueous and the organic phase were measured in a γ-counter. Both the partition coefficient $P_{(o/w)}$, which is defined as the molar concentration ratio of a single species A between n-octanol and water at equilibrium, and log$P_{(o/w)}$, which is an important parameter used to characterize lipophilicity of a compound, were calculated.

Plasma-protein binding: To distinguish free PSMA inhibitor and the bound fraction to plasma-proteins, a 500 µL sample of human blood from a Heparin- or EDTA coated vial was centrifuged at 3,000 × g (6,000 rpm, Biofuge 15) for 3 min. The plasma was incubated with app. 1.0 MBq of the radiolabeled PSMA inhibitor at 37 °C for 15 min before ultra-filtration in a modified polyethersulfone ultrafiltration vial (low-protein binding, 30 kDa, VWR International GmbH, Darmstadt, Germany). A sample of the plasma and an equal volume of ultra-filtered plasma (plasma-protein free) were measured in a γ-counter. The resulting value was corrected for unspecific adhesion to the ultra-filtration vials.

5 CELL EXPERIMENTS

$PSMA^+$ LNCaP cells (CLS: 300265) were grown in Dulbecco's Modified Eagle Medium/Nutrition Mix F-12 with Glutamax-I (1:1) (DMEM/F-12) (Invitrogen, Life Technologies, Darmstadt, Germany) supplemented with 10% fetal calf serum (FCS). Cultures were maintained at 37 °C in a 5% CO_2/humidified air atmosphere. One day prior to the experiment, cells were harvested using Trypsin/EDTA (0.05% and 0.02%) in PBS, centrifuged and resuspended with culture medium. For cell counting, a Countesse automated cell counter (Invitrogen, Carlsbad, USA) was used. All *in vitro* binding- and internalization studies were performed using live cells seeded one day prior to the experiment. For IC_{50} determination, 150,000 cells/mL were transferred to 24-well plates (1.0 mL/well) and for internalization studies 125,000 cells/mL were transferred into PLL-coated 24-well plates.

5.1 Affinity determination to PSMA (IC_{50})

The culture medium was removed and the cells were washed once with 500 µL of HBSS (Hank's balanced salt solution, Biochrom, Berlin, Germany, containing 1% bovine serum albumin (BSA)), before being left to equilibrate in 200 µL of HBSS (1% BSA) on ice for 15 min. Then, 25 µL/well of either HBSS (1% BSA; Control) or of solutions containing the respective unlabeled PSMA inhibitor (or cold metal complex) of interest in increasing concentrations (10^{-10}-10^{-4} M in HBSS (1% BSA)) were added, followed by the addition of 25 µL of [^{125}I]**7** in HBSS (1% BSA). The final radioligand concentration was 0.2 nM in all binding assays. Experiments were carried out in triplicate for each concentration. Cells were incubated on ice for 60 min. Incubation was terminated by removal of the incubation medium. Cells were thoroughly rinsed with 250 µL of HBSS. The wash medium was combined with the supernatant of the previous step. This fraction represents the amount of free radioligand. Cells were then lysed using 250 µL of 1 N NaOH, the lysate was transferred to vials and combined with 250 µL of HBSS used for rinsing the wells. Quantification of the amount of free and bound activity was performed in a γ-counter.

5.2 Internalization and cell binding kinetics

The culture medium was removed and the cells were washed once with 500 µL DMEM-F12 (5% BSA) before being left to equilibrate in 200 µL DMEM-F12 (5% BSA) at 37 °C for a minimum of 15 min. Then, 25 µL (per well) of either DMEM-F12 (5% BSA) or of a 100 µM PMPA solution (blocking) were added, followed by the addition of 25 µL of ^{68}Ga/^{177}Lu-labeled PSMA inhibitor. The final radioligand concentration was 0.2/0.5 nM in all internalization assays. To determine internalization kinetics, cells were then incubated at 37 °C for 5, 15, 30 and 60 min, respectively. Experiments were carried out in triplicate for each time point (Control and Blocking). Incubation was terminated by placing the plate on ice for app. 1 min and by subsequent removal of the incubation medium. Cells were thoroughly rinsed with 250 µL of PBS. The wash medium was combined with the supernatant of the previous step. This fraction represents the amount of free radioligand. To remove enzyme surface bound radioactivity, the cells were then incubated for 10 min with 250 µL of ice cold PMPA solution (10 µM in PBS). After removal of the supernatant, the cells were thoroughly rinsed with another 250 µL of ice cold PBS. Both fractions were combined. The internalized activity was released by incubation with 250 µL of 1 N NaOH, transferred to vials and combined with 250 µL of 1 N NaOH used for rinsing the wells. Quantification of the amount of free, PMPA-releasable and internalized activity was performed in a γ–counter.

6 ANIMAL EXPERIMENTS

All animal experiments were conducted in accordance with German Animal Welfare Act (Deutsches Tierschutzgesetz, approval #55.2-1-54-2532-71-13). The [Al^{18}F]**39** study was conducted at the Peter MacCallum Cancer Center in Melbourne in accordance with the general animal welfare regulations in Australia. The prostate cancer cell line LNCaP was suspended 1/1 in serum-free medium and matrigel (BD Biosciences, Germany) and approximately 10^7 cells in 200 µL were inoculated subcutaneously on the right shoulder of 6 - 8 weeks old mice (CD-1 nu/nu or SCID, Charles River Laboratories, Germany). Tumors were grown for 2 - 4 weeks (males) and 4 - 6 weeks (females) to reach 4 - 8 mm in diameter.

6.1 Metabolite analysis

The ^{177}Lu-labeled PSMA inhibitors [^{177}Lu]**12** and [^{177}Lu]**13** were incubated in 80 µL of human serum (37 °C) and after 1, 24 and 48 h the stability of the complexes was analyzed by Radio-TLC (sodium citrate buffer and ammonium acetate buffer/methanol (1/1)). The respective ^{68}Ga-labeled tracers (40 - 45 MBq) were injected into the tail vein of anaesthetized CD-1 nu/nu mice. The animals were sacrificed after 30 min and urine, blood and kidney were taken. The kidney was frozen in liquid nitrogen, homogenized with a ball mill and extracted with 0.2 - 1 mL PBS containing 200 nmol PMPA. The suspension was first centrifuged (15,000 g) and after ultrafiltration the extracts were analyzed by HPLC. The blood samples were centrifuged to separate the plasma from the blood cells. Plasma proteins were removed by precipitation with acetonitrile (50% (v/v), 10 min, 4 °C) and subsequent centrifugation and ultrafiltration. The blood extract was also analyzed by HPLC. For all extracts the extraction efficiency was determined in a γ–counter.

6.2 Biodistribution

The radiolabeled PSMA inhibitors (0.15 - 0.25 nmol) were injected into the tail vein of mice under isoflurane anesthesia. The uptake of the radiopharmaceuticals in selected organs, tissues and body fluids (e.g. blood, heart, lungs, liver, spleen, pancreas, stomach (without content), intestine (with content), kidney, muscle, bone, brain, tumor, tail) was examined at 1 h post injection (p.i.) and for ^{177}Lu-labeled PSMA inhibitors at 24 h p.i.. Weighted samples were quantified in a γ–counter.

6.3 Small-animal PET imaging

Imaging studies were performed at a Siemens Inveon small animal PET, followed by data analysis using the Inveon Research Workplace software. The animals were anesthetized with isoflurane and injected via tail vein with 14 - 18 MBq (0.15 - 0.25 nmol) of tracer. Dynamic imaging was performed after on-bed injection for 1.5 h. Static images were recorded at 1 h p.i. with an acquisition time of 15 min. For the blockade image, animals were co-injected with 8 mg/kg of PMPA. Images were reconstructed using 3D ordered-subsets expectation maximization (OSEM3D) algorithm without scanner and attenuation correction.

For the [Al^{18}F]**34** PET study, LNCaP-tumor bearing NOD SCID mice were injected with app. 15 MBq (3.0 nmol) [Al^{18}F]**39**. At 1 h and 3 h post-injection animals were anaesthetized in 2.5% isoflurane and 50% O_2 in air and placed on the bed of a Philips Mosaic small animal PET scanner (Philips Medical Systems, Ohio, USA; resolution 2.7 mm at the center of the FOV) and imaged over 10 min. The images were reconstructed using a 3D RAMLA algorithm as described previously (215). Quantification was performed using software developed in-house (MARVn) (216). All data are presented as mean ± standard error, n = 3.

7 HUMAN APPLICATIONS

All human studies were approved by the institutional review boards of the participating medical institutions. Patients provided signed informed consent.

7.1 [^{68}Ga]PSMA I&T PET imaging

Initial PET/CT imaging (Biograph mCT PET/CT, Siemens Medical Solution AG) at 60 min after intravenous (i.v.) administration of 133.2 MBq [^{68}Ga]**19** ([^{68}Ga]PSMA I&T) was performed. Contrast enhanced CT was carried out after i.v. administration of nonionic iodinated contrast material (100 mL, 300 mg/mL (Ultravist 300; Bayer AG, Berlin, Germany) at 1 mL/s, 90 s delay). The further imaging/reconstruction parameters were: 120 kV, effective mAs was 44, gantry rotation time 0.6 s, reconstruction thickness 1.5 mm with an increment of 0.8 mm, reconstruction kernel B30f, matrix 512 × 512. Immediately after CT scan, whole-body PET scanning was performed from the base of the skull through the mid-thigh with a 3 min acquisition time per bed position (16.2 cm) in 3D. Reconstruction was conducted with an OSEM algorithm with 2 iterations/8 subsets and Gauss-filtered to a transaxial resolution of 5 mm at full-width at half-maximum. Attenuation correction was performed using the contrast enhanced CT dataset. Circular regions of interest (ROIs) were drawn around areas with increased uptake in transaxial slices for calculation of the maximum standardized uptake

value (SUV_{max}). ROIs were automatically adapted to a three dimensional volume of interest with Syngovia™ (Siemens Medical Solutions, Erlangen, Germany) at a 40% isocontour.

Patient 1, 70 years old, was diagnosed with PCa in 2011 with an initial Gleason score of 10 (5+5). The patient had initially undergone palliative transurethral resection of the prostate, followed by androgen deprivation therapy using abiraterone acetate. Further treatment with docetaxel plus prednisolone was initiated after development of mCRPC with multiple bone metastases displayed by bone scan. At the time of imaging the serum total PSA level was 10.1 ng/mL.

7.2 [^{111}In]PSMA I&T SPECT and radioguided surgery

Patients, which might benefit from a surgical resection of single lymph node metastases were selected based on [^{68}Ga]**R3** ([^{68}Ga]HBED-CC-Ahx-KuE) PET/CT (157, 217). 24 hours before surgery the patient received an intravenous injection of 146 MBq [^{111}In]**19** ([^{111}In]PSMA I&T). SPECT imaging was performed 6 h p.i. to confirm the PET results. This image was then coregistered with a live video stream of the surgical field to provide an augmented reality display during PSMA-targeted radioguided surgery showing the position of hotspots corresponding to [^{111}In]PSMA I&T accumulation (I.4).

The 75 years old patient 2 was diagnosed with PCa in 2006 with an initial Gleason score of 8 and had undergone radical prostatectomy and radiation therapy in 2006. The patient had a PSA of 4.4 ng/mL at the day of examination and revealed four suspicious lesions on preoperative [^{68}Ga]HBED-CC-Ahx-KuE PET.

7.3 [^{177}Lu]PSMA I&T endoradiotherapy

Patient assessment for [^{177}Lu]**19** ([^{177}Lu]PSMA I&T) therapy was also performed by [^{68}Ga]**R3** ([^{68}Ga]HBED-CC-Ahx-KuE) PET/CT using Syngovia™. Contrast-enhanced PET/CT was done 1 - 5 days prior to endoradiotherapy and for follow-up at 65 ± 4 minutes after i.v. administration of 170 ± 23 MBq [^{68}Ga]HBED-CC-Ahx-KuE. Two patients with progressive mCRPC underwent therapy with 5.7 and 8.0 GBq [^{177}Lu]PSMA I&T, administered as an infusion over 15 min, respectively. Complete blood counts, parameters of renal function (serum creatinine, blood urea nitrogen) and liver function (albumin, bilirubin, enzymes), as well as tubular extraction rate measured by [^{99m}Tc]mercaptoacetyltriglycine scintigraphy were documented before and after therapy. Response to therapy was assessed by [^{68}Ga]HBED-

CC-Ahx-KuE PET combined with contrast-enhanced CT 8 - 10 weeks post-therapy. In addition, biochemical response was documented by means of PSA monitoring.

The 68-year-old patient 3 was diagnosed with progressive metastatic prostatic adenocarcinoma (Gleason Score 7) and multiple mediastinal lymph node metastases. Patient 4, 54-years of age, with adenocarcinoma of the prostate (Gleason Score 9: 4+5) status post hormonal therapy and external beam radiation therapy, presented with progressive mediastinal and retroperitoneal lymph node metastases as well as multifocal osseous lesions.

III RESULTS AND DISCUSSION

1 PSMA INHIBITOR SYNTHESIS

The *tert*-butyl protected PSMA-binding motif KuE ((S)-5-amino-1-carboxypentyl)carbamoyl)-L-glutamic acid) was synthesized in solution applying a simplified procedure (Fig. 8) from a literature protocol (126). Without need for activation (using methyltriflate), the intermediate **1** was directly reacted with H-Lys(Cbz)-O*t*Bu. After Cbz-deprotection the synthesis of **3** resulted in 73% yield over three reaction steps.

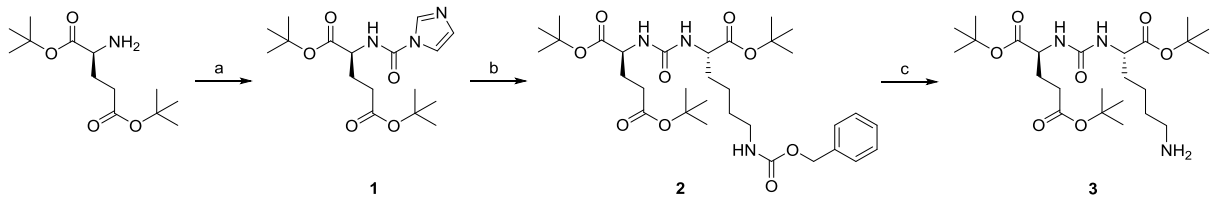

(a) DCI, TEA, DMAP [DCM]; (b) H-Lys(Z)-OtBu, TEA [DCE]; (c) Pd/C (10%), H_2 [EtOH];

Figure 8. Synthesis scheme of the *t*Bu-protected PSMA binding motif (O*t*Bu)$_2$KuE(O*t*Bu) (**3**).

1.1 Small molecule PSMA inhibitors

To allow comparability to the literature and for *in vitro* assay validation, the literature known PSMA inhibitors (I-BA)KuE (**R1**) and (F-BA)KuE (**R2**) (201) were synthesized (II.2.3). The synthesis of **R1**, **R2** and a new PSMA inhibitor for silicon-based fluoride acceptor-radiofluorination (SiFA-BA)KuE (**5**) was accomplished by coupling of **3** to 4-iodo-/4-fluoro/4-di-*tert*-butylfluorosilanebenzoic acid using *in situ* activation (DIC, HOAt, DIPEA). After acidic (TFA) deprotection of the *t*Bu-protection groups of the KuE motif and HPLC purification, the PSMA inhibitors were isolated. Conventional radiofluorination is based on multi-step procedures and involves prosthetic groups, such as *N*-hydroxysuccinimidyl-4-[^{18}F]fluorobenzoate. With this method radiolabeling of a PSMA inhibitor was reported in 30 - 35% decay corrected yield after 3 h, resulting in specific activities of 9.1 - 11.1 GBq/µmol (201). The silicon-based fluoride acceptors are synthons for isotope exchange radiofluorination (191). Di-*tert*-butylphenylfluorosilane (SiFA-phenyl) was shown to display ideal ^{19}F - ^{18}F exchange using [^{18}F]fluoride and the resulting [^{18}F]SiFA was shown to be inert towards hydrolysis under physiological conditions (218-220). SiFA-benzoic acid (SiFA-BA) and SiFA-BA-derivatives of D_2-receptor ligands were radiolabeled in 40 - 70% radiochemical yield (RCY) and cartridge purification yielded the radiolabeled D_2-receptor ligands within

10 min (202, 221). Thus, the SiFA-motif is expected to become a valuable new method for fast and high yield isotope exchange radiofluorination.

The influence of variations of the spacer length between the lipophilic SiFA-BA-motif and the PSMA-binding motif KuE on the binding affinity of the inhibitors to PSMA was investigated. Therefore, an Ahx-lysine-spacer was inserted in between the KuE motif and the SiFA-BA resulting in SiFA-BA-K-Ahx-KuE (**6**) and K(SiFA-BA)-Ahx-KuE (**7**) (II.2.3). Both, **6** and **7** were synthesized by fragment condensation of **3** and SiFA-benzoic acid conjugated to either the *N*-terminus (**6**) or the side chain amino group (**7**) of lysine-Ahx, which was assembled via Fmoc-strategy solid phase peptide synthesis. After acidic deprotection (*tert*-butyl and Boc) and HPLC purification, both inhibitors were obtained in only 10% yield, most likely due to non-quantitative coupling of SiFA-BA to the resin-bound Ahx-lysine. Reaction control was complicated by the low UV-detectability (λ = 220 nm) of Ahx-lysine.

1.2 DUPA-Pep-based inhibitors

To investigate the effect of multimerization (trimerization), the prochelator DOTAGA-anhydride was coupled to the commercially available PSMA inhibitor DUPA-Pep (ABX, Radeberg, Germany; Fig. 6) yielding DUPA-Pep-DOTAGA (**9**) in 11% yield after HPLC purification. This ´monomeric´ reference peptide and DUPA-Pep-DOTA (obtained from cooperation partner Prof. S. Reske) were compared with a trimeric DUPA-Pep-based inhibitor with the ^{68}Ga-chelator TRAP as the junction (**10**). **10** was prepared from HATU-preactivated azido-pentanoic acid and DUPA-Pep, followed by Cu(I)-catalyzed click-reaction with TRAP(propyne)$_3$ and final copper trans-chelation using an excess of NOTA in 30% overall yield (222). For evaluation, this set of PSMA inhibitors was radiolabeled with ^{68}Ga due to the fast and automated module synthesis resulting in high specific activities (223).

1.3 Chelator-conjugated PSMA inhibitors

Based on DOTA-FFK(Sub-KuE) (**R4**) (153) (Fig. 6, 7), PSMA inhibitors for theranostic application by exchange of the radiometal were synthesized, and subsequently either optimized for diagnostic or therapeutic application. The lead structure **R4** contains a three amino acid peptide spacer (phenylalanine-phenylalanine-lysine - FFK) between the KuE motif and the radiometal chelator. The novel PSMA inhibitors based on this structure design (II.2.5 - II.2.11) were synthesized by fragment condensation between the activated ester of

Sub-(*Ot*Bu)KuE(O*t*Bu)$_2$ and a modified three-amino acid peptide (chelator-conjugated or acetylated, respectively), final *t*Bu-deprotection and HPLC purification.

Peptide synthesis: The three-amino acid spacer FFK was synthesized according to a standard Fmoc-protocol solid-phase peptide synthesis (using HOBt, TBTU, DIPEA in NMP) as illustrated in Figure 9. The peptides ffk, YFK, (I-Y)FK, F(I-Y)K, (I-Y)(I-Y)K, (I-y)fk, (I-y)fGK, (I-y)fGk, K(I-Y)(I-Y)K and y-2-nal-k were prepared similarly. Usually, coupling steps were quantitative within 1 h, whereas for Fmoc-L/D-3-iodo-tyrosine (I-Y/I-y) the coupling time had to be prolonged to 18 h. To confirm quantitative coupling yields, a small amount of peptide was cleaved from the resin and analyzed by HPLC and MS. For optimal synthesis yields, all side chain functionalities have to be orthogonally protected. Due to the limited commercial availability of side chain protected Fmoc-L/D-3-iodo-tyrosine, both amino acids were used with unprotected side chains, however no influence on the synthesis yields of subsequent coupling steps (with DOTAGA-anhydride) were observed.

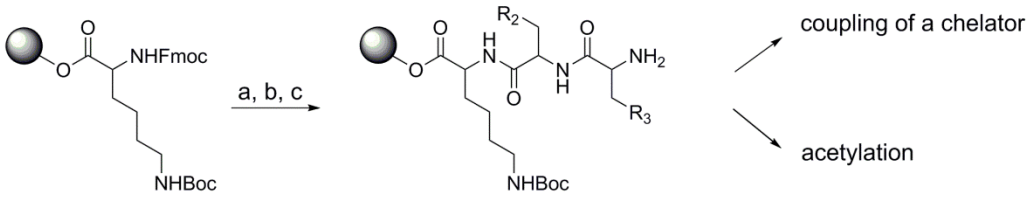

(a) 20% piperidine in NMP, Fmoc-AA$_2$-OH, HOBt, TBTU, DIPEA [NMP]; (b) 20% piperidine in NMP, Fmoc-AA$_3$-OH, HOBt, TBTU, DIPEA [NMP]; (c) 20% piperidine in NMP;

Figure 9. Schematic illustration of the resin-bound synthesis of the tripeptides H-AA$_3$-AA$_2$-Lys(Boc)-OH for *N*-terminal acetylation or functionalization with chelators (in solution or resin-bound).

Peptide acetylation: The *N*-terminal acetylated peptides (II.2.9), Ac-FFK and Ac-YXK (X = F, W, Benzothienyl-A, Biphenyl-A, 1-Nal, 2-Nal, 4-NO$_2$-F, 3,5-di-I-Y, 3-CH$_3$-Y), were synthesized applying the same Fmoc-solid phase peptide synthesis strategy. For quantitative acetylation of the unprotected *N*-terminal amine, the resin-bound tripeptides were incubated with acetic anhydride and DIPEA. Due to unprotected side chain functionalities (hydroxyl group), acetyl esters of 3,5-di-iodo-tyrosine (**31**) and 3-methyl-tyrosine (**32**) formed during acetylation of the *N*-terminus of these peptides. Thus, after cleavage of the peptides from the resin using TFA, the esters were hydrolyzed using methanol/sat. NaHCO$_3$/H$_2$O (4/2/2; v/v/v) in almost quantitative yields within 4 h.

Chelator conjugation: Besides DOTA in **R4**, the alternative chelators DOTAGA and NOPO were conjugated to the FFK spacer. For the on-resin coupling of NOPO a maximum of 60% conversion was achieved (HATU as the coupling reagent in DMSO, reaction overnight). DOTAGA-coupling could either be performed in solution or to a resin-bound peptide. Coupling in solution required a three-fold molar excess of DOTAGA-anhydride, whereas a 1.5-fold excess yielded quantitative conjugation to the resin-bound peptides. On-resin DOTA-tris-*t*Bu-ester conjugation was quantitative, but the final *tert*-butyl-deprotection step was incomplete, and therefore decreased overall yield. Further, the expensive tris-*t*Bu-ester of DOTA had to be used. Quantitative coupling of DOTA (203) and NOTA in solution via *in situ* formation of the NHS ester (203) was achieved by preincubation of unprotected DOTA (4.0 eq.) or NOTA (3.0 eq.) with NHS, EDC and DIPEA for 10 min and subsequent reaction with the peptides for another 15 min. Thus, for conjugation of DOTA and NOTA reaction in solution and for NOPO and DOTAGA resin-bound-conjugation is cost-optimized and leads to higher reaction yields.

Fragment condensation: For the fragment condensation between the respective peptides (acetylated or chelator-conjugated) and the *tert*-butyl-protected Sub-KuE-motif, either NHS-Sub-(O*t*Bu)KuE(O*t*Bu)$_2$ (**11**, II.2.5) or OPfp-Sub-(O*t*Bu)KuE(O*t*Bu)$_2$ (**33**, II.2.10) were used. The synthesis of **11** (NHS ester) from the commercially available Sub(NHS)$_2$ was performed as described in the literature (204), and the crude **11** was coupled to the respective peptides without further purification. An excess of crude **11** was applied to the peptides, to compensate for the side product (O*t*Bu)$_2$EuK(O*t*Bu)-Sub-(O*t*Bu)KuE(O*t*Bu)$_2$, which was not separated from **11**.

On the other hand, the pentafluorophenyl ester Sub(OPfp)$_2$ was synthesized in an optimized strategy according to literature procedures (224) and was purified by flash chromatography in 87% yield. A high excess (4 eq.) of Sub(OPfp)$_2$ was applied for the reaction with *tert*-butyl-protected KuE (**3**), either to avoid the formation of the above mentioned side product and since unreacted equivalents could be recovered during silica gel chromatographic purification of the crude OPfp-ester **33**, resulting in 68% yield. With this cost optimized strategy the subsequent peptide coupling resulted in increased purity and yield.

Cy5-conjugation: To expand the imaging modalities of PSMA inhibitors to optical imaging, the near infrared dye Cy5 (obtained from cooperation partner Prof. F. van Leeuwen, D. van Willigen) was conjugated to a PSMA inhibitor (with a (I-Y)(I-Y)K spacer). The conjugation of the fluorescent dye to a small molecule inhibitor/ligand is often challenging, due to the size

and lipophilicity of the dyes negatively influencing the molecule properties, such as affinity and pharmacokinetics (225). Therefore, based on the linear construct of DOTAGA-(I-Y)(I-Y)K(Sub-KuE) (**18**) a branched PSMA inhibitor **22** was developed by an additional orthogonally protected (side chain Dde-protected) lysine (DOTAGA-**K(Dde)**-(I-Y)(I-Y)K(Sub-KuE)) for conjugation of Cy5. Coupling of Cy5 to the DOTAGA-bound lysine side chain of DOTAGA-K-(I-Y)(I-Y)K(Sub-KuE) was initially conducted using the NHS-ester of the dye. Unfortunately, under the applied reaction conditions, NHS-ester hydrolysis occurred. Pre-activation of the carboxylate of Cy5 using HATU and TEA, *in situ* coupling to the peptide, and final acidic deprotection yielded **22**. High losses, caused by low resolution of the peaks in semi-preparative HPLC chromatography (Multospher column) demanded purification on an analytical column (Nucleosil column).

1.4 Addressing of the S1-accessory lipophilic pocket

To address the S1-accessory binding pocket (details described in III.3.9), a PSMA inhibitor with an aromatic moiety (4-iodo-D-phenylalanine; I-f) was developed on the basis of DOTAGA-y-nal-k(Sub-KuE) (**35**). Substitution of the suberic acid spacer with glutaric acid-(I-f) resulted in DOTAGA-y-nal-k(Glut-(I-f)-KuE (**36**). Further, reduced tracer uptake in the kidneys was reported for radiopharmaceuticals modified with an albumin-binding entity (226). For antibody fragments conjugated to an albumin-binding entity their circulation time in the blood was prolonged, resulting in an increased tumor-to-kidney-ratio (227). Also for a small-molecule folic acid derivative, increased plasma protein binding and therefore an extended plasma half-life was reported (228). Thus, the plasma-protein avidity of halogenated aromatic rings, such as para-iodo-phenylalanine (I-f) (229), was explored for increased plasma-protein binding (III.4).

For the synthesis of PSMA inhibitor **36**, Glut(OPfp)$_2$ was prepared from glutaric acid using pyridine and pentafluorophenol as described for Sub(OPfp)$_2$. After flash chromatography Glut(OPfp)$_2$ was isolated in 87% yield. Fmoc-D-4-iodo-phenylalanine was reacted with **3** in the presence of DIC, HOAt and DIPEA in solution and purified over silica. After Fmoc-deprotection, the construct was purified by HPLC. Due to insufficient purity of OPfp-Glut-(I-f)-(O*t*Bu)KuE(O*t*Bu)$_2$, after reaction with a four-fold excess of Glut(OPfp)$_2$ and DIPEA, another flash chromatography purification step was included. Finally this building block was condensed with the peptide DOTAGA-y-2-nal-k, *tert*-butyl deprotected and purified (HPLC). Due to very low yields (1.1%) of **36**, caused by high losses during multiple precipitation and purification steps of OPfp-Glut-(I-f)-(O*t*Bu)KuE(O*t*Bu)$_2$, resin-bound synthesis might improve the outcome for such peptidic constructs.

1.5 Metal complexation

All novel PSMA inhibitors and reference ligands, as well as their metal complexes evaluated in this study, are summarized in Table 4. The nat. metal complexes of the PSMA inhibitors were prepared by incubation of the respective PSMA inhibitor with an equimolar amount of aqueous $Ga(NO_3)_3$ at 40 °C or a 2.5-fold molar excess of $LuCl_3$, $Cu(OAc)_2$ or $InCl_3$ at 95 °C within 30 min, respectively. Quantitative metal complex formation was confirmed by HPLC and MS.

For complexation of $[AlF]^{2+}$ in NOTA-y-nal-k(Sub-KuE) (**34**) an excess of PSMA inhibitor (4.6 eq.) and F^- (2.0 eq.) were added to $AlCl_3$ (1.0 eq.) and heated to 105 °C. The reaction mixture was purified by HPLC to separate the product from the Al-complex and the free inhibitor as described for another PSMA inhibitor (150). Applying equal molar ratios exclusively the Al-complex was formed even after addition of 12.0 eq. of fluoride. This finding correlates with the radiolabeling data in the literature, revealing comparably low radiolabeling yields for $[Al^{18}F]$NOTA and its conjugates (192).

2 RADIOLABELING

2.1 Radioiodination using [^{125}I]NaI

[^{125}I]**R1** (([^{125}I]I-BA)KuE) serves as the reference ligand in a competitive binding assay for IC_{50} determination of novel PSMA inhibitors and as an external reference in internalization experiments. The 4-iodobenzoyl-ε-lysine in **R1** was reported to increase the affinity to PSMA by a factor of ten compared to inhibitors lacking this motif (88). For radiolabeling with an established experimental radionuclide, ^{125}I ($E_{max,\gamma}$ = 35 keV, $t_{1/2}$ = 59.4 days) was selected.

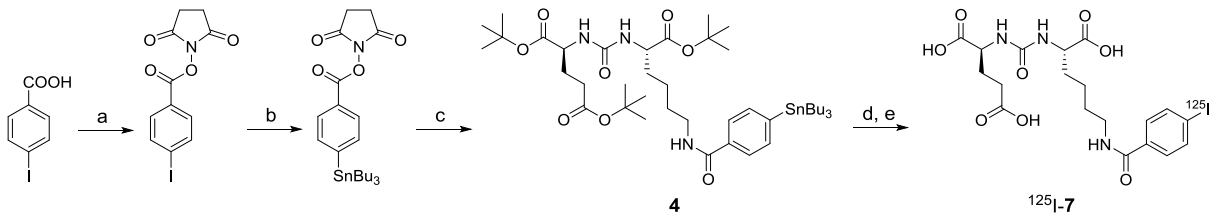

(a) NHS, DCC [DCM]; (b) $(SnBu_3)_2$, $Pd(PPh_3)_4$ [Tol]; (c) **3**, TEA [DCM]; (d) [^{125}I]NaI, peracetic acid [MeCN/H_2O]; (e) TFA;

Figure 10. Synthesis scheme of the radioiodinated reference PSMA inhibitor [^{125}I]**R1** starting from 4-iodo-benzoic acid.

Based on commercially available reagents and according to previously published methods (126, 199, 200), the reference ligand [^{125}I]**R1** was synthesized from ($SnBu_3$-BA)(O*t*Bu)KuE(O*t*Bu)$_2$ (**4**) as summarized in Figure 10. The radioiodination precursor **4** was prepared in three reaction steps starting from 4-iodo-benzoic acid in an overall yield of 44%. For ^{125}I-radioiodination app. 0.1 mg **4** was destannylated with [^{125}I]NaI within 10 min at rt using peracetic acid as the oxidizing agent. After cartridge purification, subsequent *tert*-butyl-deprotection and HPLC purification, the final product was obtained in a radiochemical yield of 44 ± 5% and radiochemical purity of > 99%. Radiolysis or degradation of the radioligand was precluded using HPLC for quality control on day 1 and 60 after synthesis.

To open a perspective for therapeutic application (^{131}I) of NOPO-conjugated PSMA inhibitors, radioiodination of a tyrosine residue in the spacer was investigated. Radioiodination with [^{125}I]NaI using the Iodogen-method (203, 205, 206), resulted in NOPO-F([^{125}I]I-Y)K(Sub-KuE) ([^{125}I]**15**) in a radiochemical yield of 63% (A([^{125}I]**15**) = 13.3 MBq) and radiochemical purity of > 99%. Thus, the tracer was used for initial *in vitro* evaluation.

2.2 $^{68}Ga^{III}$-labeling

Preparation of $^{68}Ga^{III}$ for labeling of NOTA-, DOTA-, DOTAGA-, NOPO- and TRAP-conjugated PSMA inhibitors was performed by combination of previously described methods (190, 207) with minor modifications. The $^{68}Ga^{3+}$ eluted with 1 M HCl from a ^{68}Ge/^{68}Ga generator (iThemba Labs, South Africa) was retained on a strong cation exchange cartridge followed by elution with 0.5 mL 5 M NaCl, resulting in highly concentrated ^{68}Ga activity. By the addition of 2.7 M aq. HEPES the pH was adjusted to 2.0 (NOPO or TRAP), 2.8 (NOTA), 3.5 (DOTA) or 4.5 (DOTAGA), respectively. Using 3 nmol of the respective PSMA inhibitor (95 °C, 5 min), quantitative ^{68}Ga-complexation for all PSMA inhibitors could be achieved. Quantitative complex formation of all tracers resulted in specific activities of 250 – 300 GBq/µmol and allowed their use in *in vitro* studies without further purification.

The ^{68}Ga-labeling for *in vivo* biodistribution and PET imaging studies was carried out using a fully automated GMP-compliant procedure on a GRP synthesizer (Scintomics GmbH, Germany) (207). In these cases, the obtained specific activities were 80 - 120 GBq/µmol.

Tracers for use in patients were prepared by means of an automated process in a radiochemical yield of 67 ± 10% (non-decay corrected), radiochemical purity of 98 ± 2% (ITLC-SG strips, Varian) and in calculated specific activities of 40.0 MBq/µg (37.8 GBq/µmol) for [^{68}Ga]HBED-CC-Ahx-KuE ([^{68}Ga]**R3**) and 13.6 MBq/µg (20.4 GBq/µmol) for [^{68}Ga]DOTAGA-(I-y)fk(Sub-KuE) ([^{68}Ga]PSMA I&T; [^{68}Ga]**19**), respectively.

2.3 $^{111}In^{III}$-labeling

R3 (HBED-CC-Ahx-KuE): At pH 7 (pH optimum), complexation yields for 20 MBq $^{111}In^{III}$ with 1 nmol **R3** were > 90%. Due to instability of the complex in TFA-containing HPLC solvents, and partial decomplexation or separation problems in water/acetonitrile and aqueous acetate/methanol buffers, respectively, radiochemical yields were only determined using radio-TLC. Strengthened by a two-fold decreased affinity of [^{nat}In]**R3** compared to the respective ^{nat}Ga-analog (Table 4) and reported *in vivo* decomplexation (210), low complex stability most likely limits the application of [^{111}In]HBED-CC-Ahx-KuE.

DOTAGA-conjugates: For quantitative $^{111}In^{III}$-labeling of DOTAGA-conjugated inhibitors, a 10-fold molar excess of precursor was incubated with app. 300 MBq [^{111}In]$InCl_3$ (A_S > 205 GBq/µmol) in NaOAc buffer (pH 5.3, 25 min, 95 °C) resulting in radiochemical purity of > 98% and specific activities of app. 15 GBq/µmol. For application in patients C18 light cartridge purification was conducted before dilution with 8 mL PBS and sterile filtration.

2.4 $^{177}Lu^{III}$-labeling

To obtain RCY > 95% for complexation of DOTA- and DOTAGA-conjugated PSMA inhibitors with [^{177}Lu]$LuCl_3$, 0.66 nmol of precursor were reacted with 25 MBq [^{177}Lu]$LuCl_3$ (A_S = 170 GBq/µmol) at pH 5 (0.1 M NH_4OAc, 95 °C, 30 min) resulting in specific activities of A_S ≥ 38 GBq/µmol. For application in patients 6 – 8 GBq [^{177}Lu]PSMA I&T ([^{177}Lu]**19**) were prepared in a radiochemical purity of 99.0 ± 1.0% as determined from HPLC (LiChroCART 250-4, Lichrospher100, RP18, Merck) and specific activities of 40.0 MBq/µg (59.9 GBq/µmol) were achieved.

2.5 Complexation of $[Al^{18}F]^{2+}$

$Al^{18}F$-labeling of 20 nmol NOTA-conjugated PSMA inhibitor **34** using 10 nmol $AlCl_3$ and app. 350 MBq [^{18}F]F^- (concentrated on a Chromafix PS-HCO_3^- cartridge) in NaOAc buffer (pH 4), HPLC purification and reformulation on a SepPak Vac C18 cartridge resulted in app. 40% uncorrected yield (70% RCY) after 78 min. The radiochemical purity was > 95%. Since the precursor most likely was not separated from the radiolabeled product during HPLC purification (UV signal coelution), a specific activity of ≥ 5 GBq/µmol was achieved.

Presence of DMSO increased the labeling yield, but lead to formation of a (not further characterized) side product. To reduce the synthesis time below 1 h, the reaction mixture

(reaction without adding DMSO) was purified on a SepPak Vac C18 cartridge, resulting in a radiochemical purity of > 95%, but app. 20% lower radiochemical yields.

2.6 $^{64}Cu^{II}$-labeling

Quantitative complexation of 74 MBq $^{64}Cu^{II}$ was achieved with 10 nmol NOTA-conjugate **34** in NH_4OAc buffer at pH 6.5, resulting in a specific activity of 7 GBq/µmol. For 5 nmol **34**, the labeling yield decreased to 20% (determined via radio-HPLC). Waters SepPac Vac C18 cartridge purification (conditions as described for $[Al^{18}F]^{2+}$ complexation) yielded [^{64}Cu]**34** in a specific activity of 3 GBq/µmol, respectively.

3 *IN VITRO* EVALUATION

To compare the binding of the various inhibitors to PSMA, the half maximal inhibitory concentration (IC_{50}) of each candidate was measured in a competitive binding assay on LNCaP cells (androgen sensitive human prostate adenocarcinoma cell line; Fig. 11) using [^{125}I]**R1** as radiolabeled reference inhibitor. The LNCaP cell line is derived from a left supraclavicular lymph node metastasis of prostate cancer in a 50-year old Caucasian male in 1977 (230, 231) and exhibits documented PSMA expression (54).

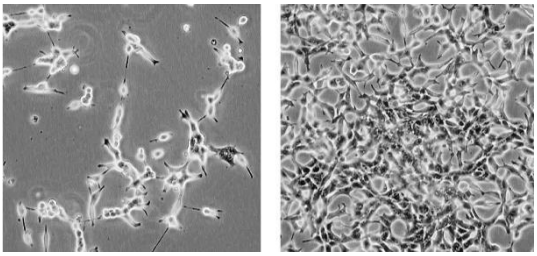

Figure 11. Microscope images of LNCaP cells with low and high confluency.

Affinity to PSMA (IC_{50}): A variety of different assays for affinity determination of PSMA inhibitors are reported in the literature, some based on the inhibition of the enzymatic activity of PSMA, others (including the assay in this work) use a competitive binding assay with a reference ligand (36, 71, 99, 125, 147, 152, 201). To establish a reproducible system, simulating the *in vivo* binding situation as realistic as possible, living cells with endogenous PSMA expression were preferred over transfected cell lines, trypsinized cells (99), membrane aliquots (232) or recombinant PSMA (99). A constant low concentration of the radioligand [^{125}I]**R1** (0.2 nM) ensures low occupancy of the PSMA binding sites (number of cells!) and allows robust measurements my means of a γ-counter (suitable count rate). To avoid PSMA inhibitor internalization, the assay was performed at 4 °C on ice. The buffer HBSS was preferred over PBS to maintain vitality of the cells during the assay, and over conventional culture medium to exclude potentially influencing supplements, such as glutamate (µM affinity to PSMA). BSA was added to avoid non-specific association to vials and plates.

Table 4. The half maximal inhibitory concentration (IC_{50} [nM]) of PSMA inhibitors determined in a competitive binding assay on LNCaP cells (1 h, 4 °C, HBSS + 1% BSA) using ([^{125}I]**R1** (c = 0.2 nM) as the radiolabeled reference. Data is expressed as mean ± SD of three independent determinations.

PSMA inhibitor	IC_{50}
Reference ligands	
(I-BA)KuE (**R1**)	7.1 ± 2.4
(F-BA)KuE (**R2**)	15.7 ± 3.7
HBED-CC-Ahx-KuE (**R3**)	5.7 ± 0.5
[^{nat}Ga]**R3**	6.1 ± 0.8
[^{nat}In]**R3**	14.2 ± 2.0
DOTA-FFK(Sub-KuE) (**R4**)	13.1 ± 2.3
[^{nat}Ga]**R4**	29.5 ± 6.6
[^{nat}Lu]**R4**	54.7 ± 6.1
Small molecule PSMA inhibitors	
(SiFA-BA)KuE (**5**)	820.0 ± 246.1
SiFA-BA-K-Ahx-KuE (**6**)	5865.5 ± 768.6
K(SiFA-BA)-Ahx-KuE (**7**)	2772.0 ± 1108.0
DUPA-Pep-based inhibitors	
DUPA-Pep-[^{nat}Ga]DOTA ([^{nat}Ga]**8**)	31.4 ± 5.8
DUPA-Pep-DOTAGA (**9**)	17.1 ± 6.5
[^{nat}Ga]**9**	36.0 ± 4.3
(DUPA-Pep-PA)$_3$-[^{nat}Ga]TRAP ([^{nat}Ga]**10**)	2.0 ± 0.1
Choice of chelator-peptide spacer unit	
DOTAGA-FFK(Sub-KuE) (**12**)	10.2 ± 1.5
[^{nat}Ga]**12**	12.1 ± 3.9
[^{nat}Lu]**12**	15.1 ± 1.5
[^{nat}Y]**12**	11.8 ± 3.2
DOTAGA-ffk(Sub-KuE) (**13**)	13.9 ± 0.4
[^{nat}Ga]**13**	15.9 ± 0.5
[^{nat}Lu]**13**	13.1 ± 2.2
[^{nat}In]**13**	9.4 ± 2.2
NOPO-FFK(-Sub-KuE) (**14**)	11.4 ± 3.1
[^{nat}Ga]**14**	33.0 ± 7.2
[^{nat}Ga]NOPO-YFK-Sub-KuE ([^{nat}Ga]**15**)	11.6 ± 4.2
Iodo-tyrosine-derivatives	
DOTAGA-(I-Y)FK(Sub-KuE) (**16**)	5.5 ± 0.3
[^{nat}Ga]**16**	4.6 ± 0.4
DOTAGA-F(I-Y)K(Sub-KuE) (**17**)	5.3 ± 1.4
[^{nat}Ga]**17**	5.3 ± 0.8
[^{nat}Ga]DOTAGA-(I-Y)(I-Y)K(Sub-KuE) ([^{nat}Ga]**18**)	5.2 ± 0.2
DOTAGA-(I-y)fk(Sub-KuE) (**19**, PSMA I&T)	10.2 ± 3.5
[^{nat}Ga]**19**	9.4 ± 2.9
[^{nat}Lu]**19**	7.9 ± 2.4
[^{nat}In]**19**	7.5 ± 1.5

PSMA inhibitor	***IC*** $_{50}$
"Kidney cleavable" sequence	
DOTAGA-(l-y)fGK(Sub-KuE) (**20**)	9.9 ± 0.3
[^{nat}Ga]**20**	9.6 ± 1.2
DOTAGA-(l-y)fGk(Sub-KuE) (**21**)	8.8 ± 1.6
[^{nat}Ga]**21**	5.1 ± 2.6
Fluorescent ligand	
DOTAGA-K(Cy5)-(l-Y)(l-Y)K(Sub-KuE) (**22**)	13.9 ± 1.7
[^{nat}Ga]**22**	12.8 ± 2.8
Linker-peptide modifications (lipophilic binding pocket)	
Ac-FFK(Sub-KuE) (**23**)	11.8 ± 1.8
Ac-YFK(Sub-KuE) (**24**)	15.0 ± 1.3
Ac-YWK(Sub-KuE) (**25**)	6.8 ± 3.3
Ac-Y-(Benzothienyl-A)-K(Sub-KuE) (**26**)	10.2 ± 4.0
Ac-Y-(Biphenyl-A)-K(Sub-KuE) (**27**)	139.4 ± 117.0
Ac-Y-1-Nal-K(Sub-KuE) (**28**)	4.3 ± 0.9
Ac-Y-2-Nal-K(Sub-KuE) (**29**)	3.9 ± 1.7
Ac-Y-(4-NO_2-F)-K(Sub-KuE) (**30**)	7.4 ± 0.5
Ac-Y-(3,5-di-I-Y)-K(Sub-KuE) (**31**)	3.8 ± 0.6
Ac-Y-(3-CH_3-Y)-K(Sub-KuE) (**32**)	7.2 ± 0.9
NOTA-ligand	
Al-NOTA-y-nal-k(Sub-KuE) ([Al]**34**)	4.9 ± 1.3
[^{nat}Ga]**34**	8.5 ± 1.6
[^{nat}Cu]**34**	8.0 ± 1.3
Addressing of S1-accessory lipophilic pocket	
DOTAGA-y-nal-k(Sub-KuE) (**35**)	8.5 ± 2.5
[^{nat}Ga]**35**	9.8 ± 3.2
[^{nat}Lu]**35**	2.1 ± 0.8
DOTAGA-y-nal-k(Glut-(l-f)-KuE) (**36**)	4.6 ± 0.9
[^{nat}Ga]**36**	9.3 ± 2.9
[^{nat}Lu]**36**	6.1 ± 1.6

Caused by the variety of assays and assay conditions in the literature (different incubation time; temperature: 4 °C, rt, 37 °C; radioligand/inhibitor concentration etc.), making a direct and quantitative comparison impossible, the K_i value (concentration independent value) was not calculated. For data normalization and comparison to the literature, as well as assay validation, the IC_{50} for the literature compounds **R1** (201), **R2** (201), **R3** (153) and **R4** (99) were included in our assay, all of which revealed low nanomolar IC_{50}'s to PSMA. Thus, only the values determined in this assay, which are summarized in Table 4 are used in the following paragraphs for the comparative assessment and discussion.

Internalization and cell binding kinetics: PSMA inhibitors with IC_{50}'s < 100 nM were evaluated for cell binding and internalization into PSMA-expressing cells. A high internalization rate may be important for therapeutic interventions, where a long retention of the radioactive isotope in the target tissue may have beneficiary influence.

To allow for radiopharmaceutical internalization in the assay, LNCaP cells were incubated with the radiolabeled PSMA inhibitors for up to one hour at 37 °C in cell culture medium (DMEM/F-12, Invitrogen) supplemented with 5% BSA. Based on comparable IC_{50}'s of the free PSMA inhibitor and the respective (radio)metal complexes, the specific activity of the tracer preparation (total amount of peptide used in the assay) has a significant effect on the cellular uptake kinetics as shown for NOPO-conjugated inhibitor [^{68}Ga]**14** (maximal achievable specific activity of app. 0.8 TBq/µmol) in Fig. 12. Concentrations above 1 nM caused a reduction of the tracer binding capacity due to increased occupancy of the binding sites by the unlabeled peptide precursor. Consequently, to minimize these effects, radiolabeling conditions have been optimized prior to these binding experiments. As an example, the ^{68}Ga-labeling (nuclide with the shortest half-life in this study) yielded specific activities of A_s = 250 – 300 GBq/µmol for DOTA- and DOTAGA-conjugated peptides after optimization (III.2.2). Due to differences in the obtained specific activity and to ensure sufficient count rates, concentrations of 0.2 nM have been selected for all ^{68}Ga- and ^{111}In-labeled compounds and concentrations of 0.5 nM for Al^{18}F-, ^{177}Lu- and ^{64}Cu-labeled PSMA inhibitors.

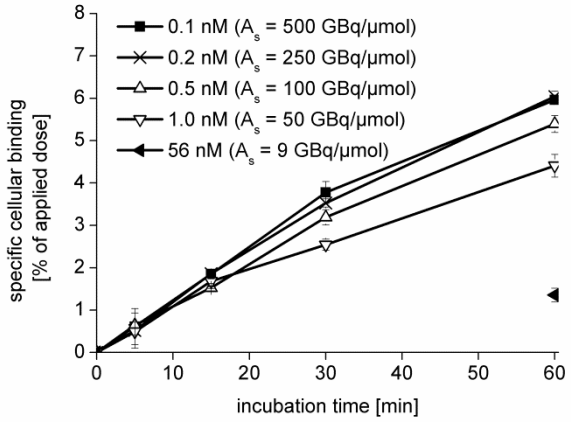

Figure 12. Cellular uptake kinetics of increasing concentrations of [^{68}Ga]**14** in LNCaP cells (37 °C, DMEM/F-12 + 5% BSA). The total cellular activity was corrected for non-specific binding (10 µM PMPA). All data are expressed as mean ± SD (n = 3).

All incubations were also performed in the presence of 10 µM PMPA (blocking) and accompanied by the reference ligand [^{125}I]**R1**. The cell binding and internalization data was corrected for non-specific binding (co-incubation with 10 µM PMPA), which was below 0.5% in all experiments. To avoid fluctuations in cell count and viability between experiments (differences in the absolute uptake of [^{125}I]**R1** in Fig. 13 - 15), data were normalized to the reference ligand [^{125}I]**R1**. For all radiolabeled PSMA inhibitors the total cellular activity and the internalized activity after an incubation of 1 h on LNCaP cells is summarized in table 5.

Table 5. Summary of the total cellular activity and the internalized activity at 1 h as % of external reference ([^{125}I]**R1**) as determined on LNCaP cells (37 °C, DMEM/F-12 + 5% BSA, 125,000 cells/well, PLL-coated plates, c = 0.2 nM for ^{68}Ga-, ^{111}In-, ^{125}I-labeled PSMA inhibitors and c = 0.5 nM for ^{177}Lu-, Al^{18}F- and ^{64}Cu-labeled inhibitors). Data is corrected for non-specific binding (10 µM PMPA) and expressed as mean ± SD (n = 3).

PSMA inhibitor	Cell binding	Internalization
Reference ligands		
[^{68}Ga]**R3**	98.9 ± 1.6%	91.1 ± 1.7%
[^{111}In]**R3**	54.2 ± 1.4%	45.4 ± 1.0%
[^{68}Ga]**R4**	18.6 ± 0.6%	14.6 ± 0.8%
[^{177}Lu]**R4**	22.4 ± 1.1%	19.3 ± 0.9%
Choice of chelator-peptide spacer unit		
[^{68}Ga]**12**	34.3 ± 0.6%	28.4 ± 0.7%
[^{177}Lu]**12**	40.9 ± 1.4%	36.1 ± 1.1%
[^{68}Ga]**13**	49.5 ± 1.5%	42.5 ± 1.7%
[^{177}Lu]**13**	51.7 ± 1.5%	44.4 ± 1.8%
[^{68}Ga]**14**	15.1 ± 0.5%	12.4 ± 0.6%
[^{125}I]**15**	45.6 ± 2.0%	39.2 ± 0.6%
Iodo-tyrosine-derivatives		
[^{68}Ga]**19** ([^{68}Ga]PSMA I&T)	65.0 ± 1.7%	59.2 ± 1.7%
[^{177}Lu]**19** ([^{177}Lu]PSMA I&T)	79.6 ± 1.1%	75.5 ± 1.6%
[^{111}In]**19** ([^{111}In]PSMA I&T)	106.3 ± 1.9%	104.2 ± 2.2%
NOTA-ligand		
[Al^{18}F]**34**	36.8 ± 0.4%	27.5 ± 0.5%
[^{68}Ga]**34**	60.5 ± 1.1%	56.6 ± 1.0%
[^{64}Cu]**34**	42.7 ± 0.4%	43.5 ± 0.4%
Addressing of S1-accessory lipophilic pocket		
[^{68}Ga]**35**	112.6 ± 2.1%	105.1 ± 2.1%
[^{177}Lu]**35**	77.3 ± 0.7%	71.7 ± 0.7%
[^{68}Ga]**36**	107.6 ± 1.3%	107.0 ± 1.2%
[^{177}Lu]**36**	119.6 ± 0.6%	118.6 ± 0.5%

3.1 Small molecule PSMA inhibitors

The formal substitution of fluorine or iodine in PSMA inhibitor **R1** and **R2** (201) by the lipophilic and bulky SiFA-motif in PSMA inhibitor **5** caused a more than 50-fold decrease in affinity (IC_{50} = 820 ± 247 nM). This might be explained by unfavorable interactions of SiFA with the narrow 8 - 20 Å wide funnel shaped tunnel leading to the S1 pocket of PSMA (active site, binding site of the KuE motif) (82, 233). To increase the distance between the active site and the SiFA motif an Ahx-lysine-spacer was introduced in PSMA inhibitors **6** and **7**, resulting in even lower affinity, which might be the result of steric hindrance or the negative interaction of the introduced positive charge of the free amino group at the lysine *N*-terminus for **7** or lysine side chain for **6** with PSMA. Therefore, a free amino group at that position was avoided during the further inhibitor development. However, due to the high steric demand and lipophilicity of the SiFA motif, resulting in highly decreased affinity and most likely unfavorable pharmacokinetics *in vivo* (as reported for other biomolecules, see also *(191, 234)*), the focus of the further PSMA inhibitor development was set to radiometal chelates, such as ^{68}Ga.

3.2 Multimerization (DUPA-Pep-based inhibitors)

The commercially available PSMA inhibitor DUPA-Pep (Fig. 6) (120) was conjugated to the metal chelators DOTA (monomeric PSMA inhibitor **8**, obtained from cooperation partner Prof. S. Reske), DOTAGA (monomeric inhibitor **9**), and TRAP (homo-trimetric inhibitor **10**). Subsequently the resulting compounds were comparatively evaluated *in vitro*. The ^{nat}Ga-complexes of **8** and **9** revealed IC_{50}'s of 31.4 ± 5.8 nM and 36.0 ± 4.3 nM, respectively, whereas the affinity of the trimeric **10** was 15-fold higher (IC_{50} = 2.0 ± 0.1 nM). Thus, multimerization is a powerful tool for affinity improvement of PSMA inhibitors. The ^{68}Ga-chelator TRAP, or potentially also its tetrameric counterpart 1,4,7,10-tetraazacyclododecane-triphosphinic acid (DOTPI) as a ^{177}Lu/^{90}Y-chelator for the multimerization of biomolecules, as reported for RGD peptides (235), open new perspectives for multimeric PSMA inhibitors with increased affinity.

3.3 Choice of chelator-peptide spacer-unit

The literature reference [^{68}Ga]HBED-CC-Ahx-KuE ([^{68}Ga]**R3**) (99) exhibited an IC_{50} of 6.1 ± 0.8 nM in our competitive binding assay. Due to complex instability, indium or lutetium labeling is not possible with the HBED-CC chelator. Thus, to maintain comparability to the compounds in the literature, [^{68}Ga]**R3** and [^{68}Ga/^{177}Lu]DOTA-FFK(Sub-KuE) ([^{68}Ga/^{177}Lu]**R4**) were evaluated in parallel with the new inhibitors. Based on **R4** (Fig. 7), PSMA inhibitors for improved ^{68}Ga-labeling were developed by the substitution of DOTA by NOPO (inhibitor **14**). To investigate the influence of the metal chelator and the metal complex on the IC_{50} of the resulting diagnostic and therapeutic PSMA inhibitors, the ^{nat}Ga/^{nat}Lu/^{nat}Y analogs of DOTAGA-conjugate **12** were evaluated.

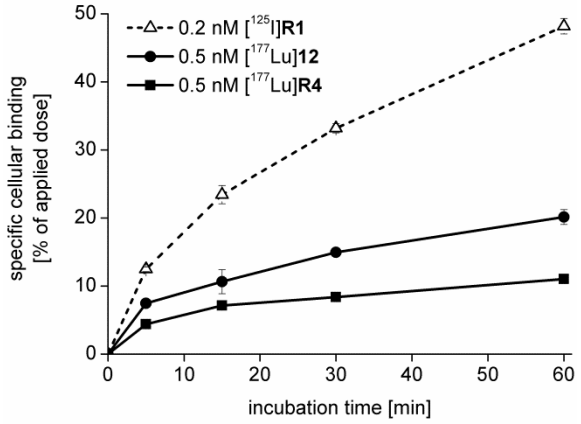

Figure 13. Cellular uptake kinetics of [^{177}Lu]**R4** and [^{177}Lu]**12**, in comparison to [^{125}I]**R1** (dashed curve) in LNCaP cells (37 °C, DMEM/F-12 + 5% BSA). The total cellular activity was corrected for non-specific binding (10 µM PMPA). All data are expressed as mean ± SD (n = 3).

Chelator modification: Comparison of the ^{68}Ga-complexes of PSMA inhibitors **R4** (DOTA-conjugated), **12** (DOTAGA-FFK(Sub-KuE)), and **14** (NOPO-FFK(Sub-KuE)) demonstrated an influence of the chelator on the binding affinity of the PSMA inhibitors. The DOTAGA-conjugate [^{nat}Ga]**12** exhibited a two-fold increased affinity compared to [^{nat}Ga]**R4** and [^{nat}Ga]**14**. For [^{nat}Lu]**12** the affinity improvement was more than three-fold compared to [^{nat}Lu]**R4** (IC_{50} = 54.7 ± 6.1 vs. 15.1 ± 1.5 nM). In correlation to the affinity improvement of ^{nat}Ga- and ^{nat}Lu-complexes of **12** compared to **R4**, the radiolabeled counterparts revealed increased cell binding and internalization (Fig. 13). Thus, DOTAGA was chosen as the chelator for the further developed PSMA inhibitors, especially for therapeutic application (^{177}Lu^{III}-complexation). Recently, the influence of chelator modifications (and the peptidic

spacer) on the targeting properties was confirmed for a series of structurally related ^{64}Cu-labeled PSMA inhibitors (236).

Stereochemistry of linker amino acids: The stereochemistry of the PSMA-binding motif (KuE) was reported to be restricted to L-amino acids (36, 96, 99). To investigate the influence of the amino acid stereochemistry in the spacer region of **12**, a substitution of the L-amino acids (FFK-spacer) by D-amino acids (ffk-spacer) was performed. This alteration did not change the affinity to PSMA, whereas for the radiolabeled D-amino acid inhibitor **13** an increased internalization was observed ([^{68}Ga]**13**: 49.5 ± 1.5% of [^{125}I]**R1**) compared to the L-amino acids containing inhibitor ([^{68}Ga]**12**: 34.3 ± 0.6% of [^{125}I]**R1**).

The NOPO-conjugated PSMA inhibitor **14** was not further evaluated for ^{68}Ga- and ^{64}Cu-PET imaging (237) because of the suboptimal affinity to PSMA (IC_{50}([^{nat}Ga]**14**) = 33.0 ± 7.2 nM). Since complexation of therapeutic radionuclides, such as ^{177}Lu or ^{90}Y is not possible with NOPO, a therapeutic option for NOPO-conjugated inhibitors might be ^{131}I-radioiodination of the peptidic spacer by substitution of one of the phenylalanine residues by tyrosine. The affinity of the tyrosine-containing inhibitor [^{nat}Ga]NOPO-fyk(Sub-KuE (**15**) was increased by a factor of three and the resulting radioiodinated NOPO-conjugated inhibitor [^{125}I]**15** exhibited a three-fold higher internalization (Table 5) compared to [^{68}Ga]**14**. Thus, the amino acid composition, as well as stereochemistry opens perspectives for PSMA inhibitor optimization.

3.4 Iodo-tyrosine derivatives

Based on the increased affinity and internalization of the NOPO-F(I-)YK(Sub-KuE) (**15**) compared to the phenylalanine-counterpart **14**, the influence of the amino acid composition of the spacer on the affinity to PSMA was investigated for the DOTAGA-conjugated inhibitors, which revealed the highest affinity and internalization in a NOPO-DOTA-DOTAGA comparison (inhibitors **R4**, **12** and **14**).

Thus, the F by I-Y substitution was investigated for the optimal position of I-Y in the tripeptide of DOTAGA-conjugated PSMA inhibitors applying the spacers (I-Y)FK, F(I-Y)K, (I-Y)(I-Y)K and (I-y)fk. All four resulting inhibitors (**16** - **19**) showed affinities below 10 nM, with no significant differences between [^{nat}Ga]**16**, [^{nat}Ga]**17**, [^{nat}Ga]**18** and [^{nat}Ga]**19** (Table 4). This finding leads to the conclusion that the substitution of one F-by-I-Y increases the affinity. In accordance with the affinity improvement of all iodo-tyrosine containing inhibitors (**16** - **19**) compared to the FFK-conjugate **12** and ffk-conjugate **13**, the total cellular uptake and internalization of both [^{68}Ga] and [^{177}Lu]**19** was increased by a factor of two compared to

[^{68}Ga]- and [^{177}Lu]**13** as shown in Fig. 14. Including biochemical, crystallographic and computational investigations, an increased interaction of aromatic rings with a lipophilic binding pocket (arene binding site) was described (233). From the S1 pocket a 20 Å funnel shaped tunnel is leading to the enzyme surface (88). A non-covalent interaction (π-cation and π-stacking) of the PSMA side chains of Trp541 and Arg511 with aromatic systems is reported to create this lipophilic pocket (233). An increased interaction of I-Y (compared to F) most likely is the explanation for an increased PSMA affinity of I-Y-containing PSMA inhibitors **15** - **19**.

However, the substitution position of iodo-tyrosine only has negligible effect on PSMA affinity most likely due to the high flexibility of the PSMA entrance loop (238). Trp541 and Arg511 are part of the PSMA 'entrance lid' (Trp541-Gly548) of the funnel-shaped tunnel of PSMA (88, 94). Crystallographic studies reveal two major conformations of the lid – open or closed. The transition between the two is enabled by flipping of the amide bond between Asn540 and Trp541 and flexibility of Gly548 (91). It was shown, that the lipophilic pocket is generated by the open conformation of the entrance lid loop and leads to a 60-fold increase in affinity for PSMA inhibitors containing a dinitrophenyl-group to bind the lipophilic pocket (233, 238). The conformation of the entrance lid is obviously dependent on the structure of the inhibitor (presence of aromatic moiety), whereas the hydrolytic activity of PSMA is not necessarily reduced by the open conformation of the entrance lid, as pteroylpoly-γ–glutamate is a functional substrate of PSMA (I.2.1). To address anticipated effects beyond affinity and internalization on the pharmacokinetics, both the L-amino acid derivative [^{68}Ga/^{177}Lu]**16** and the D-amino acid inhibitor [^{68}Ga/^{177}Lu]**19**, were comparatively evaluated in mice.

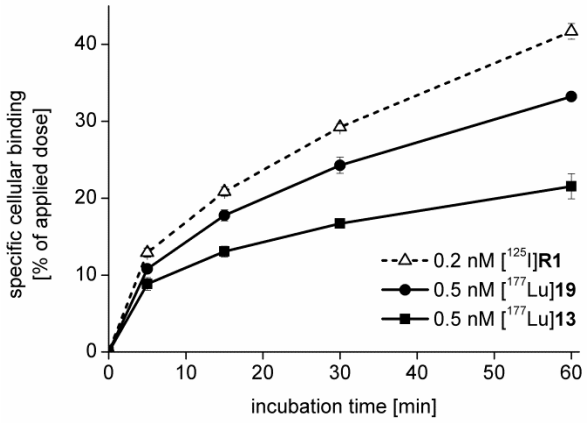

Figure 14. Cellular uptake kinetics of [^{177}Lu]**13** and [^{177}Lu]**19**, in comparison to [^{125}I]**R1** (dashed curve) in LNCaP cells (37 °C, DMEM/F-12 + 5% BSA). The total cellular activity was corrected for non-specific binding (10 μM PMPA). All data are expressed as mean ± SD (n = 3).

3.5 “Kidney cleavable” sequence

Due to the high and persistent radioactivity accumulation of PSMA inhibitors in the kidneys, strategies for decreasing renal tracer uptake are desirable, especially for a therapeutic application. Earlier studies on reduction of kidney activity of radiolabeled antibody fragments or peptides indicate, that they are reabsorbed via luminal endocytosis after glomerular filtration (239). A common approach to block reabsorption of peptides and small proteins at the proximal tubular cells from the luminal fluid, is the administration of basic amino acids such as L-lysine resulting in direct urinary elimination of the radiopharmaceuticals (195). Due to the high PSMA-expression in the kidneys, amino acids might not effectively block PSMA inhibitor uptake in the kidneys. Thus, another approach involving interposition of a cleavable linkage between the biomolecule and the liberated radio-metabolite of rapid urinary excretion was investigated.

For the introduction of the glycyl-lysine motif, the so called “kidney cleavable” sequence into a [^{188}Re]organorhenium-labeled antibody fragment decreased kidney uptake was reported, with an equal radioactivity level in blood and tumor (240). When the biomolecule is attached to the lysine side chain and the *C*-terminal carboxylate of the lysine remains unbound even higher efficiency was reported (241, 242). Thus, we introduced the glycyl-lysine-motif into the (I-y)fk spacer of PSMA inhibitor **19**. To maintain ligand geometry and to allow an additional glycine to be inserted into the peptidic backbone in between the lysine and the phenylalanine residue, the suberic acid spacer was replaced by glutaric acid resulting in PSMA inhibitor **20**. Selective cleavage was reported for glycine-L-lysine, which might cause metabolic instability of the PSMA inhibitor in the blood. Thus, the glycine-D-lysine (**21**) derivative was also included in this evaluation. These structural modifications in inhibitors **20** and **21** did not alter the affinity towards PSMA compared to **19** as summarized in Table 4. To determine differences in inhibitors **20** and **21**, especially concerning the intended kidney cleavable property, the next evaluation step was a metabolite analysis in mice (chapter III.5.1).

3.6 Fluorescent ligand

For application of a PSMA inhibitor in bimodal and optical imaging, cooperation to the Leiden University Medical Center (LUMC) was established. Synthesis of PSMA-targeted DTPA conjugates containing near-infrared fluorescent dyes, such as Cy3 and Cy7 has successfully been performed in Leiden (unpublished data).

Based on DOTAGA-(I-Y)(I-Y)K(Sub-KuE) (**18**), an additional lysine was used as the junction for conjugation of a fluorescent dye to combine both, fluorescence imaging and radioactivity

based imaging in one molecule. The near-infrared dye Cy5 (obtained from the LUMC) was inserted at a position, where the narrow funnel-shaped tunnel of PSMA (82) was expected to be broad enough to tolerate such a bulky, lipophilic modification. In consistence with this hypothesis, [^{nat}Ga]DOTAGA-K(Cy5)-(I-Y)(I-Y)K(Sub-KuE) ([^{nat}Ga]**22**) revealed an IC_{50} of 12.8 ± 2.8 nM, being only slightly lower than the respective PSMA inhibitor without the lysine-Cy5-modification (IC_{50} of [^{nat}Ga]**18** was 5.2 ± 0.2 nM). Thus, modification of PSMA inhibitors with optical dyes without drastically reducing the PSMA affinity seems feasible and investigations on the sub-cellular level and future application in image-guided surgery might be possible.

3.7 Lipophilic modification in the spacer

Based on an increased affinity of iodo-tyrosine-derivatives (III.3.4) compared to the phenylalanine-counterparts (III.3.3), the effect of lipophilic (aromatic) modifications in the spacer of the PSMA inhibitors were investigated. Therefore, a series of acetylated derivatives **23 - 32** was synthesized and the affinity to PSMA was determined on LNCaP cells. Substitution of DOTAGA by the acetyl group was performed, because acetylation is entirely sufficient for exploration of structure-activity relationships on the "pure" influence of the spacer geometry. For data normalization the acetylated inhibitors Ac-FFK(Sub-KuE) (**23**) (IC_{50} = 11.8 ± 1.8 nM) and the respective YFK-derivative **24** (IC_{50} = 15.0 ± 1.3 nM) were synthesized. Both compounds exhibited a similar affinity compared to the DOTAGA-counterparts **12** (FFK spacer; IC_{50} = 10.2 ± 1.5 nM) and the DOTAGA-YFK(Sub-KuE (data not shown in table 4; IC_{50} = 12.5 ± 3.2 nM).

The bulky substituent biphenylalanine in PSMA inhibitor **27** showed the lowest affinity in this series, most likely due to steric repulsion within the 20 Å deep amphipathic funnel leading to the active center of PSMA (82) and suboptimal fit into the lipophilic pocket. Iodo-tyrosine like substituents, exhibiting comparable lipophilicity and steric demand, were introduced resulting in inhibitors **30** (4-nitro-phenylalanine) and **32** (methyl-tyrosine). Both, **30** and **32**, as well as the tryptophan-containing inhibitor **25** and the benzothienylalanine-containing inhibitor **26** exhibited comparable affinities to **19**. The diiodo-tyrosine-containing inhibitor **31**, and naphthylalanine-containing **28** (1-Nal) and **29** (2-Nal), revealed two-fold higher affinities. Due to synthetic problems caused by the unprotected diiodo-tyrosine side chain of **31** resulting in an additional deprotection step (cleavage of the acetyl ester formed on the side chain hydroxy group, III.1.5) and the good availability of the naphthylalanine-derivatives, peptide **29** (Y-2-Nal-K spacer) was selected for further PSMA inhibitor development.

3.8 NOTA ligand

Taking the optimized peptide spacer y-2-nal-k from the acetylated PSMA inhibitor **29**, and to open more perspectives on radioisotopes, a NOTA-conjugated inhibitor **34** was synthesized primarily for $[Al^{18}F]^{2+}$-labeling, but also for complexation of $^{64}Cu^{II}$ and $^{68}Ga^{III}$. Affinities (IC_{50}) of the cold complexes were 4.9 ± 1.3 nM, 8.5 ± 1.6 nM and 8.0 ± 1.3 nM, respectively. Unlike for the PSMA inhibitors discussed so far, e.g. iodo-tyrosine derivative **19**, the cell binding and internalization kinetics were less effective for radiolabeled **34** as expected from the affinities. [Al/^{nat}Ga/^{nat}Cu]**34** showed comparable affinity to [^{nat}Ga/^{nat}In/^{nat}Lu]**19**, but the internalization in LNCaP cells after 1 h incubation was 27 to 57% for radiolabeled **34**, compared to 60 to 104% for radiolabeled **19** (after 60 min in LNCaP cells; as % of [^{125}I]**R1**). This might be caused by the increased lipophilicity, prolonging the tracer internalization kinetics, which might influence the pharmacokinetics *in vivo* and needs to be further investigated in animal studies.

3.9 Addressing of the S1-accessory lipophilic pocket

In the literature, the DOTA-conjugated PSMA inhibitor MB-17 (243) was reported to show increased affinity compared to **R3** and **R4** by introduction of an aromatic moiety (1-naphtylalanine) directly conjugated to the KuE-unit. As discussed in III.3.1, a variety of small molecule inhibitors like **R1** and **R2** (201), as well as MIP-1072 and MIP-1095 (125) (Fig. 4) exhibit high affinity to PSMA. Further, the accessory tunnel leading to the active center of PSMA is reported to be highly flexible in inhibitor binding (238). Crystal structure based characterization of the active center of PSMA revealed an additional (second) lipophilic binding pocket (88, 244), the so-called S1-accessory lipophilic pocket. The S1-accessory lipophilic pocket is formed from the arginine-patch exosite (Arg463, Arg534 and Arg536), Glu457 and Asp465 near the S1 site by conformational change of Arg463. Recent findings confirm an interaction of aromatic moieties with the S1-accessory lipophilic pocket, as reported for **R1** (PDB code: 3D7H). In consistence with the lower affinity, only a partial interaction of the fluorobenzyl-group of DCFBC (145) with the S1-accessory pocket is reported (PDB code: 3D7D), whereas the pocket appears to be closed for PSMA inhibitors with shorter P1 side chains, such as DCIT (245) and DCMC (143) (PDB codes: 3D7G and 3D7F).

Para-halogenated aromatic systems are reported to increase plasma-protein binding (229) and conjugated to the N_ε-amino group of KuE seem favorable in terms of PSMA-affinity (126). Thus, combining the plasma-protein binding strategy and the interaction with the S1-

accessory lipophilic pocket, 4-iodo-phenylalanine was introduced in PSMA inhibitor **35**, resulting in (DOTAGA-y-nal-k(Glut-(I-f)-KuE)) (**36**).

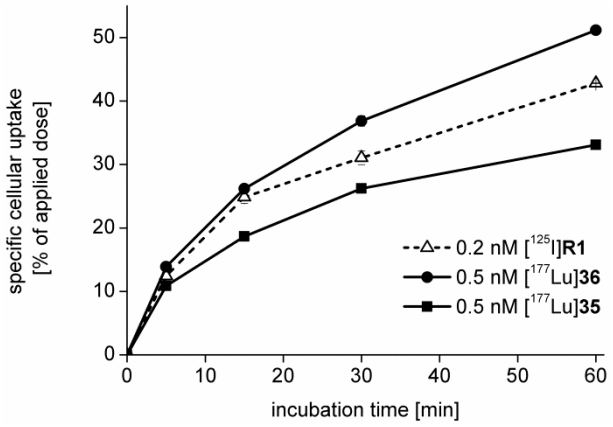

Figure 15. Cellular uptake kinetics of [^{177}Lu]**35** and [^{177}Lu]**36** in comparison to [^{125}I]**R1** (dashed curve) in LNCaP cells (37 °C, DMEM/F-12 + 5% BSA). The total cellular activity was corrected for non-specific binding (10 µM PMPA). All data are expressed as mean ± SD (n = 3).

The ^{nat}Ga- and ^{nat}Lu-complexes of **35** and **36**, both containing the y-2-nal-k-peptide, revealed affinities in the low nanomolar range, but unlike reported for MB-17 in the literature (243) no increase in affinity to PSMA was observed by substitution of the suberic acid spacer (inhibitor **35**) by glutaric acid-(iodo-phenylalanine) (inhibitor **36**). Interestingly, the cell binding and internalization kinetics (Fig. 15) revealed a significant increase in [^{177}Lu]**36** uptake in LNCaP cells compared to [^{177}Lu]**35** and [^{125}I]**R1**. Whereas for [^{177}Lu]**35** the internalization into LNCaP cells was lower than the reference (71.7%), although the affinity was 2.1 ± 0.8 nM, [^{177}Lu]**36** (IC_{50} = 6.1 ± 1.6 nM) exhibited 118.6 ± 0.5% of [^{125}I]**R1** internalized after an incubation of 1 h on LNCaP cells. The high affinity, but comparably low internalization of **35** is in consistence with the differences between affinity and internalization for NOTA ligand **34** (III.3.8), indicating differences in cell uptake kinetics compared to previous inhibitors, such as radiolabeled **19**. However, **36** seems to be highly effective in cell internalization, which has to be investigated in animal models.

4 LIPOPHILICITY AND PLASMA-PROTEIN BINDING

Lipophilicity: The partition coefficient of the novel PSMA inhibitors between n-octanol and PBS (pH 7.4) was determined using the shake-flask method. All radiolabeled PSMA inhibitors in this study were highly hydrophilic (Table 6), with the reference ligand [^{125}I]**R1** and the NOPO-conjugate [^{125}I]**15** being the most lipophilic PSMA inhibitors. The reference compound [^{68}Ga]**R3**, which was shown to exhibit favorable pharmacokinetics *in vivo* (99), was more hydrophilic compared to the radiolabeled DOTA-conjugate **R4**.

Table 6. Lipophilicity expressed as log$P_{(o/w)}$ (distribution coefficient in n-octanol/PBS) of radiolabeled PSMA inhibitors. Data are expressed as mean ± SD (n = 6).

PSMA inhibitor	**log$P_{(o/w)}$**
Reference ligands	
[^{125}I]**R1**	-2.41 ± 0.03
[^{68}Ga]**R3**	-4.11 ± 0.08
[^{68}Ga]**R4**	-3.18 ± 0.21
[^{177}Lu]**R4**	-2.66 ± 0.02
DUPA-Pep-based inhibitors	
[^{68}Ga]**8**	-3.62 ± 0.21
[^{68}Ga]**10**	-2.89 ± 0.11
Choice of chelator-peptide spacer unit	
[^{68}Ga]**12** ([^{68}Ga]**13**)	-3.60 ± 0.07
[^{177}Lu]**12** ([^{177}Lu]**13**)	-3.89 ± 0.08
[^{68}Ga]**14**	-3.55 ± 0.07
[^{125}I]**15**	-1.77 ± 0.05
Iodo-tyrosine-derivatives	
[^{68}Ga]**19** ([^{68}Ga]PSMA I&T)	-4.31 ± 0.32
[^{177}Lu]**19** ([^{177}Lu]PSMA I&T)	-4.12 ± 0.11
[^{111}In]**19** ([^{111}In]PSMA I&T)	-4.51 ± 0.06
NOTA-ligand	
[Al^{18}F]**34**	-3.67 ± 0.33
[^{68}Ga]**34**	-3.95 ± 0.02
Addressing of S1-accessory lipophilic pocket	
[^{68}Ga]**35**	-3.83 ± 0.06
[^{177}Lu]**35**	-4.11 ± 0.06
[^{68}Ga]**36**	-3.53 ± 0.06
[^{177}Lu]**36**	-3.05 ± 0.02

Whereas NOPO-conjugate [^{68}Ga]**14** was even less hydrophilic, the ^{68}Ga- and ^{177}Lu-labeled DOTAGA-conjugated PSMA inhibitors **12** (= **13**), and **19**, showed increased hydrophilicity (and higher affinities) compared to [^{68}Ga/^{177}Lu]**R4**. Thus, hydrophilicity due to negative charges at the chelator unit of PSMA inhibitors, such as DOTAGA-(l-y)fk(Sub-KuE) (**19**) seems to increase the affinity to PSMA.

The NOTA-ligand [Al^{18}F/^{64}Cu/^{68}Ga]**34**, as well as the ^{68}Ga- and ^{177}Lu-labeled inhibitors **35** and especially **36**, designed for optimized lipophilic interaction with lipophilic PSMA pockets, revealed correspondingly higher log$P_{(o/w)}$ values, however having the hydrophilic KuE-motif and the chelator (NOTA or DOTAGA) at both ends of the molecule, radiolabeled PSMA inhibitors **34**, **35** and **36** were still highly hydrophilic compared to the lipophilicity of other peptides, such as peptides binding the CXCR-4 receptor (log$P_{(o/w)}$ ([^{68}Ga]CPCR4-2) = -2.90 ± 0.08) (246).

Plasma-protein binding: High *in vivo* plasma-protein binding increases the plasma half-life of the radiopharmaceutical and therefore might offer beneficiary effects on the tracer distribution (higher uptake into target tissue), but could also increase the background activity level especially at early time points. In general, drugs binding to plasma-proteins with high affinity feature moderate to high lipophilicity, in many cases due to halogenated aromatic groups. Others provide a structural motif containing two negatively charged motifs (carboxyl- or hydroxyl-groups) connected to each other via a lipophilic spacer moiety of variable length (226).

To estimate the bioavailability of [^{177}Lu]**19**, [^{177}Lu]**35** and [^{177}Lu]**36** in blood circulation, the extent of plasma-protein binding was determined by ultrazentrifugation. In accordance with an almost similar lipophilicity of [^{177}Lu]**19** and [^{177}Lu]**35**, the plasma-protein binding of these PSMA inhibitors was 82% and 81%, respectively. These high values might be explained by the multiple negative charges (carboxylates of KuE and DOTAGA) at both ends of the molecules, being connected over a lipophilic peptide spacer, one of the structural motifs reported to bind plasma proteins (226). In addition, the intercalation of an additional iodo-phenylalanine residue increased the lipophilicity of [^{177}Lu]**36** compared to [^{177}Lu]**35**. As expected, the iodo-phenyl group insertion resulted in an increased log$P_{(o/w)}$ of -3.05 ± 0.02 and almost quantitative plasma-protein binding of 97%. An observed increased internalization of [^{177}Lu]**36** compared to [^{177}Lu]**35**, although both compounds revealed comparable IC_{50}'s, and other effects on the pharmacokinetic behavior of radiolabeled **36** related to the higher lipophilicity and the increased plasma-protein binding were further investigated *in vivo*.

5 *IN VIVO* EVALUATION

5.1 Metabolite analysis

In a first *in vitro* assessment, the complex stability of [^{177}Lu]DOTAGA was confirmed by incubation of [^{68}Ga]**12** in human serum (37 °C) and DTPA solution (0.4 M, rt), respectively.

Stereochemistry of spacer amino acids: To investigate the influence of the amino acid composition on the metabolic stability of the radiopharmaceuticals *in vivo*, a HPLC-based metabolite analysis of PSMA inhibitors [^{68}Ga]**12** (FFK spacer) and [^{68}Ga]**13** (ffk spacer) was performed. Animals were sacrificed 30 min p.i. of the ^{68}Ga-labeled inhibitors to come to a compromise between the short half-life of ^{68}Ga and an increasing metabolic degradation with time. Kidney homogenate, blood extract and the urine of CD-1 nu/nu mice were subsequently extracted and analyzed by HPLC. Representative HPLC profiles of extracts and body fluids are shown in Figure 16.

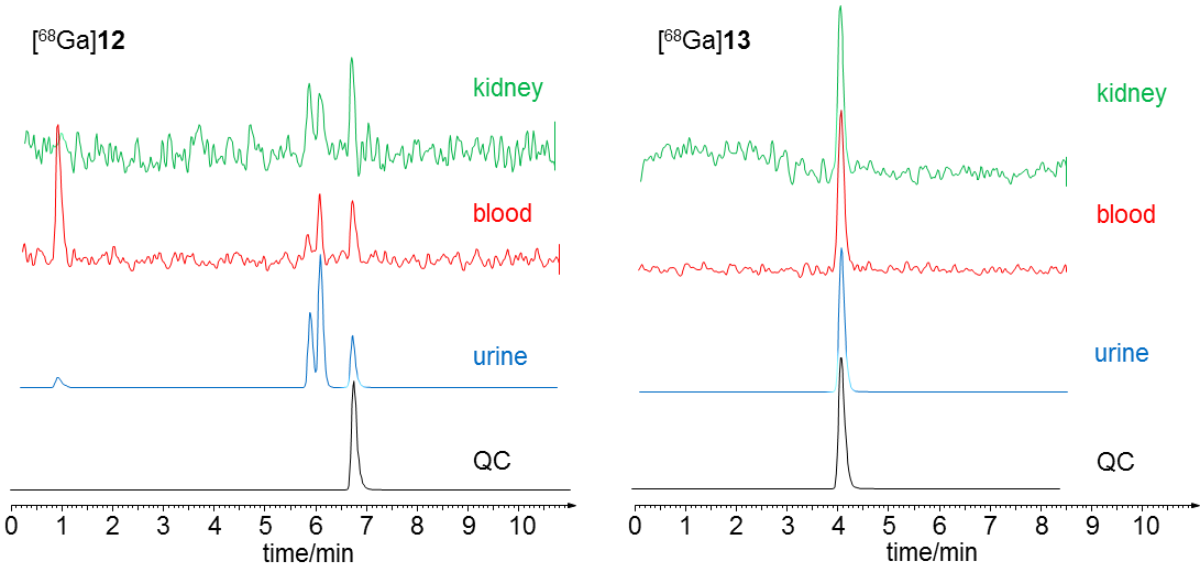

Figure 16. Exemplary radio-HPLC analyses of extracts from homogenized organs and body fluids from CD-1 nu/nu mice (30 min p.i. of 40 to 45 MBq of ^{68}Ga-labeled tracer, Chromolith column, flow rate 3 mL/min) for [^{68}Ga]**12** (3% for 3 min, 3% to 95% in 6 min, 95% for 3 min) and [^{68}Ga]**13** (3% to 95% in 6 min, 95% for 3 min).

Extraction efficiencies from the blood and from the kidney were 56% and 43% for [^{68}Ga]**12** and 61% and 62% for [^{68}Ga]**13**, respectively. Rapid *in vivo* degradation was observed for [^{68}Ga]**12** containing the L-amino acid tripeptide FFK, resulting in only 21% intact tracer in blood after 30 min. [^{68}Ga]**13** (D-amino acid spacer ffk) was found to be stable in blood (100%

intact tracer) at 30 min p.i.. Further, we observed significant inter-individual differences in metabolization kinetics for [^{68}Ga]**12** (with its L-amino acid spacer) in mice, which might explain inconsistent *in vivo* results obtained with other PSMA inhibitors with L-amino acid spacers in the literature (151, 152).

Also for the iodo-tyrosine derivative [^{68}Ga]**16** (L-amino acid spacer) high metabolic degradation was observed, whereas [^{68}Ga]**R3** ([^{68}Ga]HBED-CC-Ahx-KuE) was stable in the examined time frame (data not shown). These findings are in consistence with an unfavorable tumor uptake of [^{68}Ga]**R4** (L-amino acid spacer) in a comparative evaluation with [^{68}Ga]**R3** *in vivo* (99). Therefore high stability of the D-amino acid spacers seems to be beneficiary over L-amino acid spacers in terms of tumor targeting efficiency *in vivo*.

For [^{177}Lu]**19**, containing a D-amino acid linker, the *in vivo* stability of the aromatic C-I bond of the iodo-tyrosine was investigated at 1 h p.i. in urine, blood and kidney and at 24 h p.i. in the urine (blood and kidney extracts revealed unsatisfactory signal-to-noise ratios in the HPLC, respectively). De-iodination was not observed using a HPLC-method able to discriminate the tyrosine-peptide from the iodo-tyrosine peptide (data not shown).

"Kidney-cleavable" sequence: To investigate the glycyl-lysine sequence and to determine the intended metabolic degradation in the kidney, both "kidney cleavable" PSMA inhibitors **20** and **21** were subjected the same metabolite analysis. Although the glycyl-lysine sequence is reported to be cleaved selectively by the brush border membrane bound enzyme carboxypeptidase M and to be stable in blood (247, 248), for [^{68}Ga]**20** and [^{68}Ga]**21** no radiometabolites were detected in kidney extracts and the urine. Thus, the affinity of the glycyl-lysine-motif to carboxypeptidase M might be much lower than the affinity of inhibitors **20** and **21** to PSMA and fast internalization might prevent metabolic degradation. However, due to the high metabolic instability of these inhibitors (more than 80% after 30 min in blood), both **20** and **21** are not expected to possess any beneficiary effect *in vivo*, but to have a lower tumor targeting potential compared to **19**. Therefore, **20** and **21** were not further evaluated. The insertion of highly charged linkers in PSMA inhibitors was reported to decrease kidney uptake of the PSMA inhibitors (196, 197). If this approach or other modifications, like the injection of an excess of PMPA, as described for MIP-1095 (249) allow the reduction of kidney-toxic radiation dose in humans has to be investigated in further studies.

5.2 Biodistribution

5.2.1 PET tracers

The organ distribution of the PSMA inhibitors at 1 h p.i. was investigated in LNCaP-tumor xenograft bearing mice (CD-1 nu/nu or SCID) after injection of 0.15 - 0.25 nmol of the respective radiopharmaceutical. For tumor inoculation serum-free medium/matrigel (1/1) was used and due to the androgen-sensitivity of LNCaP cells, tumors grew faster in males (2 - 4 weeks) compared to females (4 - 6 weeks) (231). To provide comparability to the literature by exclusion of differences in the mouse model, in the applied molar amount of peptide, and the experimental setup, the reference compounds [^{68}Ga]**R3** and [^{68}Ga]**R4** were included in the *in vivo* evaluation of the novel PSMA inhibitors. The biodistribution of ^{68}Ga-labeled PSMA inhibitors at 1 h p.i. in CD-1 nu/nu mice is summarized in Table 7.

Multimerization: Initial biodistribution data (n = 2) indicate a valuable improvement in tumor targeting by the multimerization concept, which led to a 15-fold increase in affinity for [^{68}Ga]**10** compared to the DOTAGA-monomer [^{68}Ga]**9**. The practical suitability of this metabolically instable homo-multimeric-PSMA inhibitor was investigated in detail in PET imaging studies (III.5.3).

PSMA inhibitors with moderate metabolic stability: Compared to the reference compound [^{68}Ga]**R3** ([^{68}Ga]HBED-CC-Ahx-KuE), the metabolically instable DOTAGA-derivative [^{68}Ga]**12**, as well as the corresponding iodo-tyrosine derivative [^{68}Ga]**16**, revealed low PSMA-mediated tumor- and kidney-uptake (Fig. 17). In combination with higher activity levels in PSMA-unspecific tissues such as the blood, the lungs and the liver, it reflects the metabolic degradation and circulation, or PSMA-unspecific uptake of radiometabolites in other organs. This finding is in consistence with the unfavorable tumor targeting properties of [^{68}Ga]**R4** reported recently (99).

Table 7. Biodistribution (in %ID/g) at 1 h p.i. in LNCaP-tumor bearing CD-1 nu/nu mice: the reference compound [^{68}Ga]**R3** (n = 4), the moderately stable inhibitors [^{68}Ga]**12** and [^{68}Ga]**16** (n = 5, respectively), the metabolically stable inhibitor [^{68}Ga]**13** (n = 5), dual-tracer biodistribution of the iodo-tyrosine derivative [^{68}Ga/^{177}Lu]**19** (n = 4), PSMA inhibitor [^{68}Ga]**35**, [^{68}Ga]**36** (n = 4, respectively) targeting the S1-accessory lipophilic pocket, and initial data for the DUPA-Pep-trimer [^{68}Ga]**10** (n = 2).

	[^{68}Ga]**R3**	[^{68}Ga]**12**	[^{68}Ga]**16**
blood	0.38 ± 0.18	1.40 ± 0.66	1.63 ± 0.23
heart	0.43 ± 0.07	0.59 ± 0.17	0.65 ± 0.18
lung	1.87 ± 0.28	2.89 ± 0.95	1.59 ± 0.49
liver	0.47 ± 0.19	2.27 ± 0.36	0.88 ± 0.10
spleen	14.68 ± 3.65	2.75 ± 0.92	4.13 ± 4.22
pancreas	0.88 ± 0.35	0.50 ± 0.15	0.63 ± 0.60
stomach	0.44 ± 0.04	0.56 ± 0.15	0.54 ± 0.18
intestine	0.38 ± 0.12	0.39 ± 0.08	0.36 ± 0.15
kidney	100.22 ± 4.79	57.56 ± 18.79	64.57 ± 14.88
muscle	0.29 ± 0.06	0.40 ± 0.17	0.29 ± 0.09
brain	0.03 ± 0.01	0.08 ± 0.03	0.05 ± 0.02
bone	0.32 ± 0.06	0.54 ± 0.31	0.34 ± 0.05
tumor	4.75 ± 1.38	2.50 ± 0.44	1.64 ± 0.58
	[^{68}Ga]**13**	[^{68}Ga]**19**	[^{177}Lu]**19**
blood	0.31 ± 0.11	0.45 ± 0.23	0.44 ± 0.19
heart	0.25 ± 0.08	0.26 ± 0.08	0.29 ± 0.08
lung	1.13 ± 0.31	1.49 ± 0.38	1.65 ± 0.56
liver	0.17 ± 0.04	1.00 ± 0.39	1.10 ± 0.41
spleen	5.55 ± 2.39	3.88 ± 1.46	5.85 ± 2.26
pancreas	0.36 ± 0.11	0.54 ± 0.15	0.57 ± 0.24
stomach	0.39 ± 0.19	0.42 ± 0.10	0.42 ± 0.14
intestine	0.18 ± 0.05	0.27 ± 0.07	0.69 ± 0.14
kidney	96.12 ± 55.89	53.26 ± 9.02	107.24 ± 15.61
muscle	0.26 ± 0.15	0.35 ± 0.08	0.56 ± 0.36
brain	0.03 ± 0.01	0.03 ± 0.02	0.04 ± 0.03
bone	0.13 ± 0.05	0.27 ± 0.08	0.22 ± 0.05
tumor	5.23 ± 1.70	4.95 ± 1.57	7.96 ± 1.76
	[^{68}Ga]**10** (n = 2)	[^{68}Ga]**35**	[^{68}Ga]**36**
blood	0.43 ± 0.14	1.48 ± 0.09	1.29 ± 0.14
heart	0.19 ± 0.03	0.68 ± 0.06	0.65 ± 0.13
lung	1.06 ± 0.25	1.58 ± 0.24	2.06 ± 0.23
liver	0.50 ± 0.16	0.72 ± 0.09	1.08 ± 0.13
spleen	4.42 ± 1.44	3.70 ± 0.74	8.40 ± 2.15
pancreas	0.35 ± 0.06	0.48 ± 0.08	0.60 ± 0.13
stomach	0.32 ± 0.09	0.89 ± 0.11	0.62 ± 0.06
intestine	0.32 ± 0.14	0.50 ± 0.06	0.63 ± 0.13
kidney	114.94 ± 35.43	93.95 ± 6.94	104.82 ± 14.34
muscle	0.14 ± 0.03	0.36 ± 0.10	0.42 ± 0.12
brain	0.02 ± 0.01	0.17 ± 0.18	0.44 ± 0.06
bone	0.50 ± 0.15	0.46 ± 0.24	0.05 ± 0.01
tumor	6.18 ± 0.95	4.97 ± 0.97	6.29 ± 2.22

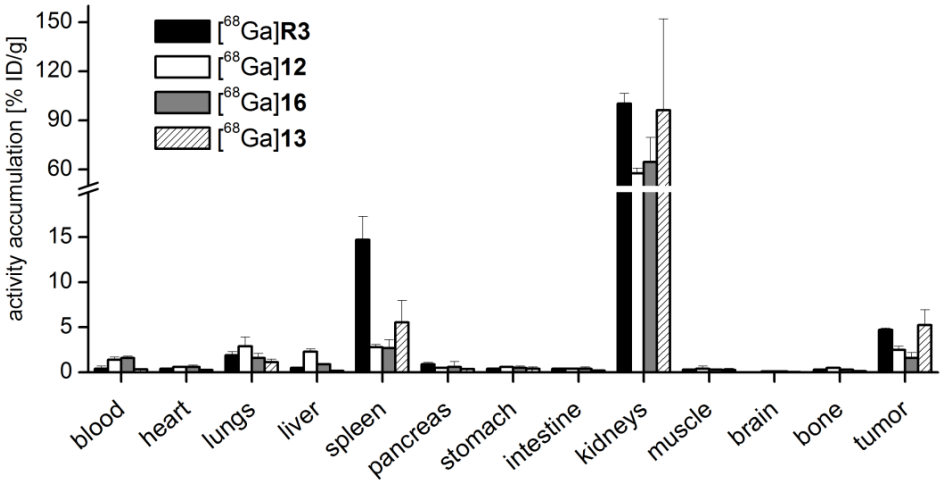

Figure 17. Biodistribution (in % ID/g) of the metabolically instable PSMA inhibitors [^{68}Ga]**12** and [^{68}Ga]**16** and the stable inhibitor [^{68}Ga]**13** (n = 5, respectively) in comparison to [^{68}Ga]**R3** (n = 4) at 1 h p.i. in LNCaP-tumor bearing CD-1 nu/nu mice.

Metabolically stable inhibitors (ffk spacer): As expected from the metabolite analysis, the metabolically stabilized D-amino acid derivative [^{68}Ga]**13**, showed lower activity accumulation organs without PSMA-expression and higher tracer uptake in both kidneys and tumor (Fig 17). Although the affinity and internalization kinetics were less efficient for [^{68}Ga]**13** compared to [^{68}Ga]**R3**, the (PSMA-specific) tumor and kidney uptake at 1 h p.i. was almost identical (even slightly higher). Further, lower [^{68}Ga]**13** uptake in spleen and PSMA-unspecific tissues, such as lung, liver, pancreas, and intestine compared to [^{68}Ga]**R3** were observed.

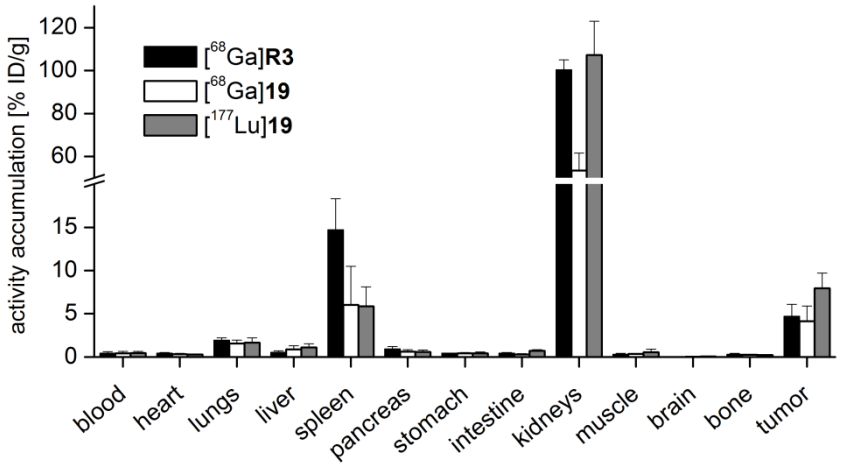

Figure 18. Dual-tracer biodistribution (in % ID/g) of [^{68}Ga]**19** and [^{177}Lu]**19** plotted in comparison to [^{68}Ga]**R3**. Studies were conducted at 1 h p.i. of the radiopharmaceuticals in LNCaP-tumor bearing CD-1 nu/nu mice (n = 4, respectively).

Iodo-tyrosine derivatives: The metabolically stable (D-amino acid spacer) iodo-tyrosine derivative **19** was examined in a dual-tracer biodistribution of [^{68}Ga]- and [^{177}Lu]**19** at 1 h p.i. in LNCaP-tumor bearing CD-1 nu/nu mice. In accordance with the findings for [^{68}Ga]**12** and [^{68}Ga]**13**, the tumor uptake significantly increased by exchange of the L- by the D-amino acids in the spacer of iodo-tyrosine derivatives [^{68}Ga]**16** and [^{68}Ga]**19**. Compared to [^{68}Ga]**13** (ffk spacer), [^{68}Ga]**19** ((I-y)fk spacer) revealed a comparable biodistribution. In comparison to [^{68}Ga]**R3** (Fig. 18), radiolabeled **19** shows equal tumor uptake, lower uptake in the spleen and [^{68}Ga]**19** revealed lower kidney accumulation. Interestingly, although the PSMA-affinity of [^{nat}Lu]**19** is only marginally increased compared to [^{nat}Ga]**19**, internalization of [^{177}Lu]**19** into LNCaP cells was significantly enhanced. This improved internalization is well reflected by an increased uptake of [^{177}Lu]**19** in the LNCaP-tumor xenografts and in all organs with documented PSMA expression (54, 68, 250), like kidneys and spleen in the biodistribution study. As opposed to the spleen, for kidneys a high PSMA expression is reported in the literature (68). However, in PSMA-blocking experiments the uptake of radiolabeled PSMA inhibitors in the spleen was reduced (250), indicating (at least partial) PSMA-specific tracer uptake in the spleen.

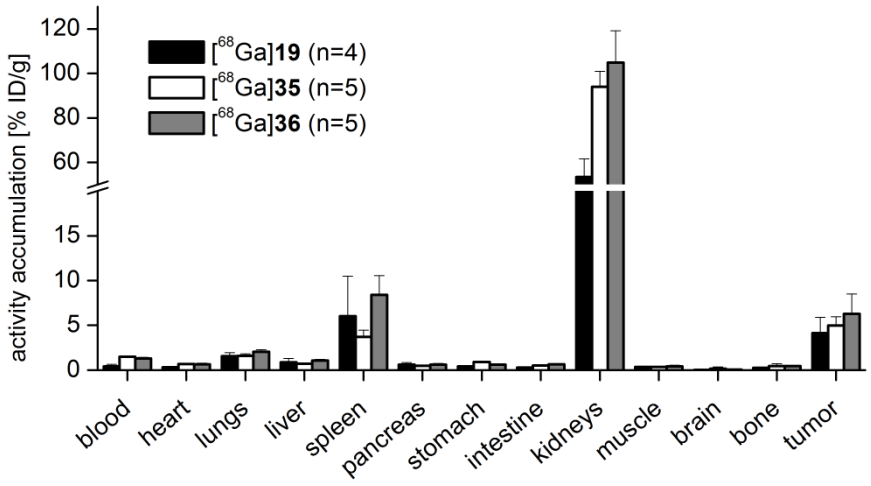

Figure 19. Comparison of the biodistribution of [^{68}Ga]**19**, [^{68}Ga]**35** and [^{68}Ga]**36** (in % ID/g) in LNCaP-tumor bearing CD-1 nu/nu mice at 1 h p.i. (n = 4, respectively).

S1-accessory lipophilic pocket (imaging): Comparison of the biodistribution of the ^{68}Ga-labeled PSMA inhibitors **19**, **35** and **36** at 1 h p.i. in LNCaP-tumor bearing CD-1 nu/nu mice is shown in Fig. 19. No significant differences in the organ distribution of these radiotracers were observed. However, the activity levels in the blood were increased for [^{68}Ga]**35** and [^{68}Ga]**36**. Also in the internalization experiment differences in cell uptake was observed for

radiolabeled **35** compared to radiolabeled **19**. Thus, the higher blood activity for [^{68}Ga]**35** compared to [^{68}Ga]**19** might be due to altered pharmacokinetics of this PSMA inhibitor, but needs to be further investigated. For [^{68}Ga]**36**, an increased blood activity can be explained by an increased lipophilicity and a higher plasma-protein binding for [^{68}Ga]**36**. Unlike reported for MB-17 in the literature, reporting of an increased tumor uptake caused by the affinity improvement, the affinity, as well as the uptake of [^{68}Ga]**36** in the tumor was comparable to that of [^{68}Ga]**35**. With respect to a potential endoradiotherapeutic benefit of the higher blood levels, caused by 97% plasma-protein binding for [^{177}Lu]**36**, [^{177}Lu]**36** was further investigated at a later time point (24 h p.i.).

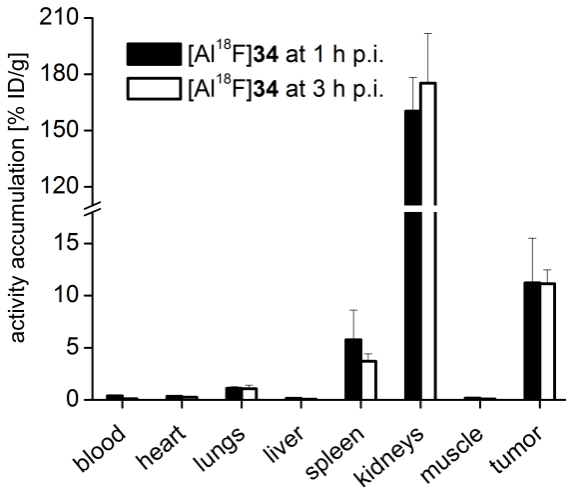

	[Al^{18}F]**34** (1 h)	[Al^{18}F]**34** (3 h)
blood	0.39 ± 0.08	0.11 ± 0.02
heart	0.35 ± 0.07	0.26 ± 0.1
lungs	1.12 ± 0.14	1.08 ± 0.35
liver	0.16 ± 0.02	0.08 ± 0.04
spleen	5.75 ± 2.86	3.71 ± 0.72
kidneys	160.41 ± 17.84	175.3 ± 26.41
muscle	0.17 ± 0.05	0.09 ± 0.02
tumor	11.22 ± 4.29	11.14 ± 1.33

Figure 20. Biodistribution (in % ID/g) of 1.4 - 1.5 MBq (≤ 0.3 nmol) [Al^{18}F]**34** in LNCaP-tumor bearing NOD-SCID mice at 1 h and 3 h p.i. (n = 3, respectively).

Radiofluorinated NOTA-ligand [Al^{18}F]34: Due to the longer half-life of ^{18}F, the biodistribution of [Al^{18}F]**34** (app. 0.3 nmol peptide) in LNCaP-tumor bearing NOD-SCID mice was investigated at 1 h and 3 h p.i. (Fig. 20). As expected from the biodistribution of ^{68}Ga-labeled PSMA inhibitors **13** and **19**, for [Al^{18}F]**34** low activity levels in PSMA-non-specific organs and high PSMA-mediated uptake in kidneys (160 ± 17.8% ID/g after 1 h), tumor (11.2 ± 4.3% ID/g after 1 h) and spleen (5.8 ± 2.9% ID/g after 1 h) were observed. None of the tracer accumulating organs showed activity wash-out from 1 h to 3 h p.i., indicating a PSMA-mediated internalization of the radiopharmaceutical followed by retention of the activity in the interior of the cells (81). Interestingly, the blood activity at 1 h p.i. (0.4 ± 0.1% ID/g) is lower as compared to [^{68}Ga]**35** (1.5 ± 0.1% ID/g; Table 7), which might either be caused by differences in the mouse strain or be the result of the molecular differences, especially in the chelate of [Al^{18}F]NOTA-conjugate **34** and [^{68}Ga]DOTAGA-conjugate **35**.

5.2.2 ^{177}Lu-labeled radiopharmaceuticals for endoradiotherapeutic application

To investigate the long-term biodistribution of the potential ^{177}Lu-labeled endoradiotherapeutics with respect to optimize the radiopharmaceutical's retention in the tumor, mice were sacrificed 24 h p.i.. The biodistribution of 2 - 3 MBq (app. 0.15 nmol) [^{177}Lu]**19**, [^{177}Lu]**35** and [^{177}Lu]**36** in LNCaP-tumor bearing mice at 24 h p.i. is summarized in Table 8.

Table 8. Biodistribution (in % ID/g) at 24 h p.i. in LNCaP-tumor bearing mice: [^{177}Lu]**19** (n = 4 in CD-1 nu/nu mice), [^{177}Lu]**35** (n = 5 in SCID mice) and [^{177}Lu]**36** (n = 4 in SCID mice). n.d. = not determined

	[^{177}Lu]**19**	[^{177}Lu]**35**	[^{177}Lu]**36**
blood	0.01 ± 0.00	0.02 ± 0.00	0.05 ± 0.02
heart	0.02 ± 0.00	0.04 ± 0.01	0.10 ± 0.03
lung	0.14 ± 0.03	0.10 ± 0.03	0.26 ± 0.10
liver	1.34 ± 0.14	0.04 ± 0.00	0.16 ± 0.06
spleen	0.93 ± 0.33	1.38 ± 0.47	6.63 ± 3.25
pancreas	0.04 ± 0.02	0.05 ± 0.01	0.20 ± 0.11
stomach	0.06 ± 0.01	0.07 ± 0.02	0.13 ± 0.04
intestine	0.20 ± 0.07	0.10 ± 0.03	0.14 ± 0.06
kidney	7.38 ± 1.51	28.08 ± 15.84	100.92 ± 45.43
adrenals	n. d.	3.35 ± 3.85	2.37 ± 0.41
muscle	0.04 ± 0.03	0.04 ± 0.01	0.07 ± 0.04
brain	0.01 ± 0.00	0.02 ± 0.01	0.11 ± 0.03
bone	0.15 ± 0.02	0.16 ± 0.12	0.03 ± 0.01
tumor	2.67 ± 0.45	4.50 ± 1.14	16.05 ± 2.51

Compared to the biodistribution of [^{177}Lu]**19** at 1 h p.i. (dual-tracer experiment with [^{68}Ga]**19**) in LNCaP-tumor bearing CD-1 nu/nu mice, the accumulation of [^{177}Lu]**19** 24 h p.i. revealed washout from all organs, especially the kidneys (107 ± 16% ID/g at 1 h and 7 ± 2% ID/g at 24 h p.i.), but also from the tumor (8 ± 2% ID/g at 1 h and 3 ± 1% ID/g at 24 h p.i.) as shown in Figure 21 (left panel).

To investigate the influence of a higher blood activity level of PSMA inhibitor **35** (biodistribution of [^{68}Ga]**35** at 1 h p.i. in Fig. 19), the biodistribution of [^{177}Lu]**35** was investigated at 24 h p.i. (Fig. 21, right panel). The tumor retention at 24 h was slightly higher (5 ± 1% ID/g) compared to [^{177}Lu]**19**, which might be caused by different mouse models, but more likely is due to the higher blood activity at 1 h p.i. which delivers the activity subsequently to the tumor.

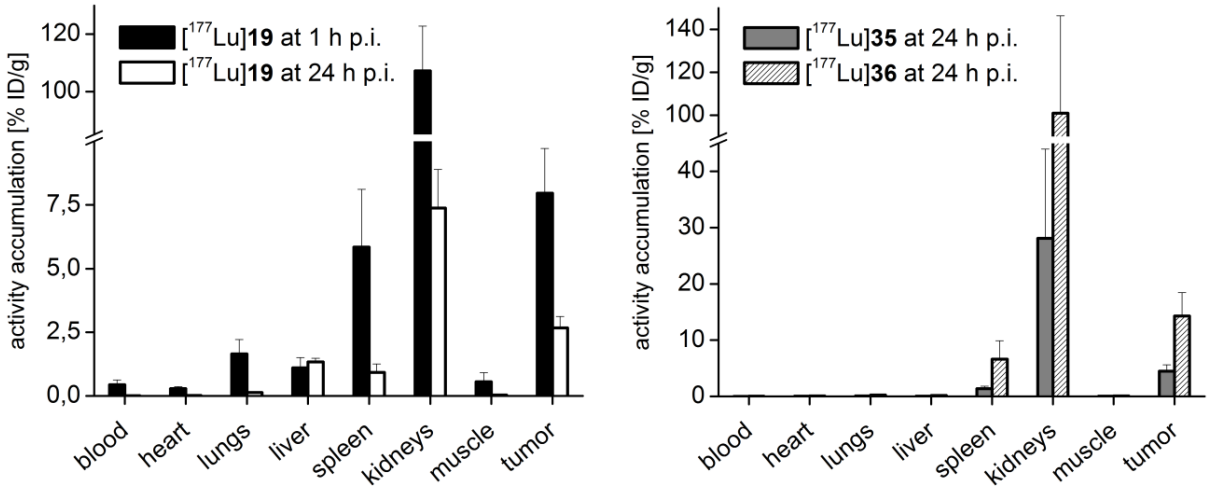

Figure 21. Biodistribution of ^{177}Lu-labeled PSMA inhibitors. **Left panel.** [^{177}Lu]**19** at 1 h (dual-tracer biodistribution with [^{68}Ga]**19**, n = 4) and 24 h p.i. (n = 5) in LNCaP-tumor bearing CD-1 nu/nu mice. **Right panel.** [^{177}Lu]**35** and [^{177}Lu]**36** at 24 h p.i. in LNCaP-tumor bearing SCID mice (n = 5, respectively).

Compared to [^{177}Lu]**19** and [^{177}Lu]**35**, a significant increase in tumor activity at 24 h p.i. was observed for [^{177}Lu]**36** (16 ± 3% ID/g). This finding is in accordance with *in vitro* results, since radiolabeled **36** exhibited the highest internalization rate in this study. Further, the plasma-protein binding of [^{177}Lu]**36** was 97% compared to app. 82% for [^{177}Lu]**19** and [^{177}Lu]**35**. The high [^{177}Lu]**36** retention in the tumor is either explained by the concept, that plasma-protein binding decelerates the excretion of biomolecules, therefore increasing the uptake in PSMA-specific tissues primarily the kidneys and the tumor. On the other hand, interaction of [^{177}Lu]**36** with the S1-accessory pocket might influence the uptake and cellular processing of this radiopharmaceutical. The [^{177}Lu]**36** activity in the spleen (6 ± 3% ID/g) and the kidneys (101 ± 45% ID/g) at 24 h p.i. was accordingly also higher compared to [^{177}Lu]**35** and [^{177}Lu]**19**, indicating PSMA-specific uptake in these organs. A proof of *in vivo* binding specificity was performed in PET imaging.

5.2.3 Mouse model

Whereas all biodistributions of ^{68}Ga-labeled tracers were performed in CD-1 nu/nu mice, biodistribution of [^{177}Lu]**35** and [^{177}Lu]**36** was performed in SCID mice (Fig. 21), since SCID mice were found to be an alternative mouse strain with more reliable tumor growth rates. Although we could not detect any differences in the tumor uptake and whole body

biodistribution of radiolabeled PSMA inhibitors between male and female mice bearing LNCaP-tumor xenografts, male mice were preferred over females due to the androgen-dependent growth of LNCaP cells. The use of male mice for implantation of LNCaP-tumor xenografts resulted in faster tumor-induction, although same growth rates of the tumors compared to females (231).

5.3 Small-animal PET imaging

5.3.1 PET images

To determine the suitability of ^{18}F- and ^{68}Ga-labeled PSMA inhibitors for PET diagnostics, images were recorded on a small animal PET scanner (Siemens Inveon PET Scanner). Therefore, LNCaP-tumor bearing mice were injected (i.v.) with the radiolabeled PSMA inhibitors and imaged at 1 h p.i. with an acquisition time of 15 min.

Multimerization: The DUPA-Pep-based PSMA inhibitors [^{68}Ga]**9** (DOTAGA monomer) and [^{68}Ga]**10** (TRAP trimer) were used to investigate the influence of multimerization of a PSMA inhibitor on the imaging properties *in vivo*. The monomer [^{68}Ga]**9** showed similar PET images than [^{68}Ga]**R4**, [^{68}Ga]**12** and [^{68}Ga]**16**, which indicates metabolic degradation for DUPA-Pep based radiopharmaceuticals. However, at 1 h p.i. no differences in metabolic degradation could be observed in comparison to the latter mentioned radiotracers, although DUPA-Pep does not contain a free carboxylate in the spacer (as a proposed attack point for carboxypeptidases in the blood). Thus, in linear peptidic constructs, the amino acid stereochemistry highly influences metabolic stability *in vivo*.

The trimer [^{nat}Ga]**10** combining three identical DUPA-Pep-molecules conjugated to the TRAP chelator revealed an 15-fold higher PSMA affinity (IC_{50} = 2.0 ± 0.1 nM) compared to the monomers [^{nat}Ga]**8** (DOTA-conjugated) and [^{nat}Ga]**9** (DOTAGA-conjugated). Due to the homotrimeric structure, [^{68}Ga]**10** (three PSMA-targeting groups) the influence of the metabolic degradation is reduced, which is well reflected in a much higher tumor to background ratio for [^{68}Ga]**10** (Fig. 22). The tumor and the majority of the kidney uptake can be blocked by co-injection of the structurally independent PSMA inhibitor PMPA, proving the specificity of the tracer uptake in these tissues (Fig. 22). Therefore, multimerization of PSMA inhibitors is not only a powerful tool to increase the affinity of the inhibitor, but also useful to compensate for metabolic degradation *in vivo*.

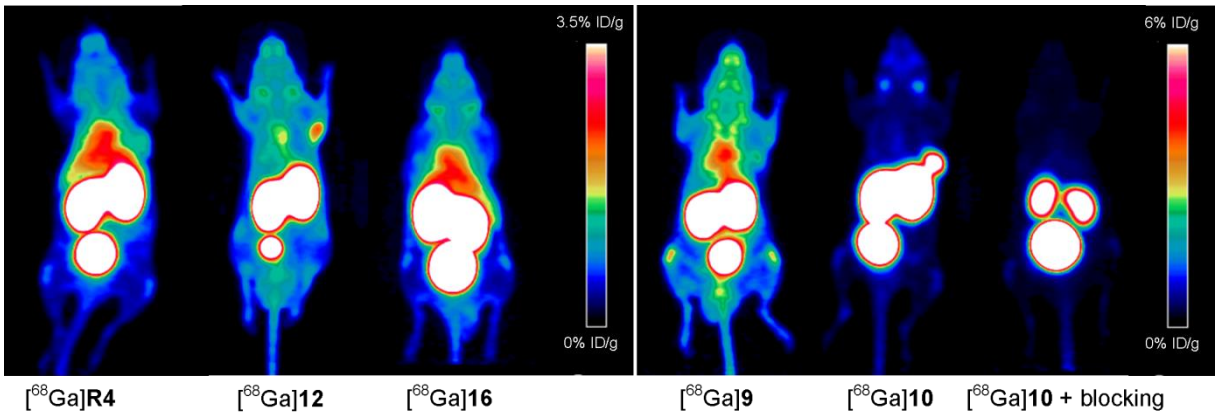

Figure 22. PET images (MIP at 1 h p.i.) of app. 15 MBq (0.15 - 0.25 nmol) [^{68}Ga]**R4** (DOTA) and [^{68}Ga]**12** (DOTAGA), iodo-tyrosine derivative [^{68}Ga]**16**, DUPA-Pep-based inhibitors [^{68}Ga]**9** and [^{68}Ga]**10** and co-injection of 8 mg/kg PMPA and [^{68}Ga]**10** in LNCaP-tumor bearing CD-1 nu/nu mice.

PSMA inhibitors with moderate metabolic stability: In Figure 22, the PET study of the metabolically instable inhibitors (L-amino acid spacer) is summarized, namely [^{68}Ga]**R4** (DOTA-FFK(Sub-KuE)), and the DOTAGA-conjugated inhibitors [^{68}Ga]**12** (FFK spacer) and [^{68}Ga]**16** ((I-Y)FK spacer). In accordance with the data from the metabolite analysis and the biodistribution, all PSMA inhibitors revealed inefficient tumor-targeting and high background activity in the blood pool and thorax organs at 1 h p.i.. Due to differences in the metabolic activity, inter-individual differences between the animals were observed (comparison of [^{68}Ga]**12** and [^{68}Ga]**16**). Therefore, PSMA inhibitors with L-amino acid spacers are not expected to provide reliable information on the metastatic spread of PCa in humans.

Metabolically stable PSMA inhibitors: In contrast to the metabolically instable L-amino acid spacers (e.g. in [^{68}Ga]**12**), D-amino acid-containing inhibitors like [^{68}Ga]**13** (ffk spacer), which were shown to be fully stable over an 30 min observation period in mice (Fig. 16), revealed an increased tumor and kidney uptake and reduced blood pool activity in biodistribution studies (Fig. 17). This finding is in consistence with reported PSMA expression (68) and PSMA-mediated tracer uptake into kidneys and tumor during PET imaging at 1 h p.i. (Fig. 23). Both, PET images of [^{68}Ga]**13** and [^{68}Ga]**19** ((I-y)fk spacer) revealed clear delineation of the LNCaP xenografts and the kidneys, as well as low background activity in the blood, resulting in higher tumor to organ ratios as compared to [^{68}Ga]**R3** ([^{68}Ga]HBED-CC-Ahx-KuE) (Fig. 23). Interestingly, the observed bladder activity of [^{68}Ga]**R3** was lower at 1 h p.i. as compared to [^{68}Ga]**13** and [^{68}Ga]**19**, indicating differences in the tracer excretion kinetics *in*

vivo, which might lead to differences in the optimal imaging time point for human applications.

In accordance with the biodistribution data, no significant increase in tumor-targeting for [^{68}Ga]**19** compared to [^{68}Ga]**13** was observed. Based on the higher affinity and the increased cell uptake and internalization of [^{68}Ga/^{177}Lu/^{111}In]**19**, and its favorable pharmacokinetic profile in mice, radiolabeled **19** was selected for initial patient applications.

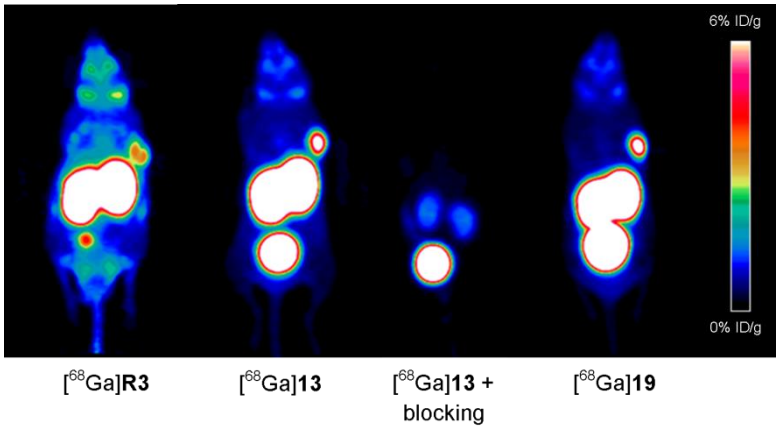

Figure 23. PET images (MIP at 1 h p.i.) of app. 15 MBq (0.15 - 0.25 nmol) [^{68}Ga]**R3** ([^{68}Ga]HBED-CC-Ahx-KuE), [^{68}Ga]**13** (ffk spacer), [^{68}Ga]**13** co-injected with PMPA (8 mg/kg), and [^{68}Ga]**19** ((I-y)fk spacer) in LNCaP-tumor bearing CD-1 nu/nu mice.

Specificity of binding: Besides the high PSMA-specificity of the tracers *in vitro* (III.3), the tracer binding specificity to PSMA was also investigated *in vivo.* LNCaP-tumor bearing mice were co-injected with 8 mg/kg PMPA (as shown for [^{68}Ga]**10**, [^{68}Ga]**13**, [^{68}Ga]**36**, [Al^{18}F]**34** + blocking). After PMPA-co-injection a drastically reduced tracer uptake in the tumor, the kidneys, and the background (blood pool, thorax organs of the mice) was observed (Fig. 22 - 25). Thus, blocking experiments prove the PSMA-specificity of the tracer uptake especially in tumor for all radiopharmaceuticals in this study.

S1-accessory lipophilic binding pocket: Figure 24 shows exemplary PET images of [^{68}Ga]**35** (y-nal-k spacer) and [^{68}Ga]**36** in LNCaP-xenograft bearing SCID mice. As expected from the *in vitro* data, both tracers were primarily taken up into the tumor and the kidneys, with excretion into the bladder. Due to differences in tumor size and position, as well as the high positron energy of ^{68}Ga ($E_{\beta^+,max}$ = 1.9 MeV), the xenograft appears less radiating for the mouse with the smaller tumor (close to the kidney) after injection of [^{68}Ga]**36** as compared to

[^{68}Ga]**35** (partial-volume effect). However, the biodistribution of both compounds (Table 7, Fig. 20) revealed no differences in tumor uptake 1 h p.i.. Compared to [^{68}Ga]**19** and [^{68}Ga]**35** at 1 h p.i., the background signal in the blood pool was slightly increased for [^{68}Ga]**36**, which can be explained by the higher plasma-protein binding (97% vs 81%).

With respect to endoradiotherapeutic application of the PSMA inhibitor **36**, a plasma-protein bound "tracer reservoir" related effect on the tumor uptake at late time points has been studied with the longer-lived isotope ^{177}Lu (III.5.2). Therefore, PSMA inhibitors with a S1-accessory lipophilic pocket targeting moiety (aromatic amino acid directly conjugated to the Nε of the KuE motif), which additionally binds to plasma-proteins leads to an increase in tracer uptake in PSMA-specific tissues, which seems to be highly beneficial for endoradiotherapeutic application of these radiopharmaceuticals. However, due to the lower background activity at 1 h p.i., PSMA inhibitor **35** was preferred over **36** as the basis for the further development of imaging agents, such as ^{68}Ga- and Al^{18}F-labeled inhibitors for PET or ^{99m}Tc-labeled PSMA inhibitors for SPECT imaging.

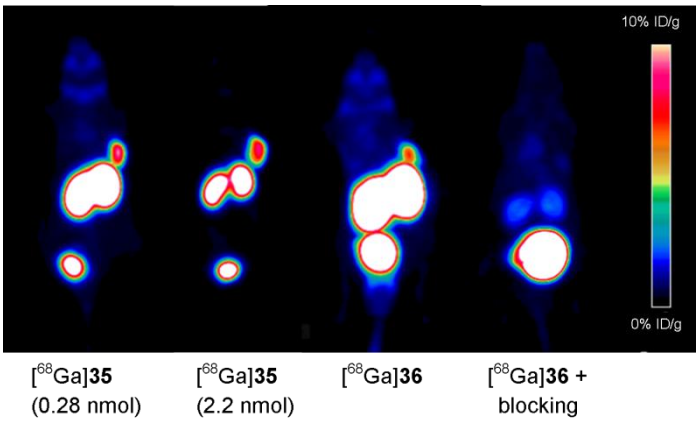

Figure 24. PET images (MIP at 1 h p.i.) of app. 15 MBq [^{68}Ga]**35** (0.28 nmol), [^{68}Ga]**35** (2.2 nmol), [^{68}Ga]**36** (0.23 nmol), and [^{68}Ga]**36** + PMPA (8 mg/kg) in LNCaP-tumor bearing SCID mice.

Effect of molar amount of peptide: To ensure comparability of all so far discussed imaging and biodistribution data, the animals were injected with similar peptide amounts of 0.15 - 0.25 nmol. Based on the tracer principle for PET and SPECT imaging agents introduced by von Hevesy and Paneth, low amounts of radiolabeled peptide (pmol to nmol range) allow displaying of biological processes without interfering with these processes. To avoid the risk of pharmacological intervention in endoradiotherapeutic treatment,

radiolabeling procedures were optimized to high specific activities to keep the peptide amount as low was possible (≤ 200 µg/patient/intervention).

In a first proof-of-concept PET study using [^{68}Ga]**35** in LNCaP-tumor bearing SCID mice, the influence of increasing PSMA inhibitor amounts (0.27 ± 0.03 nmol, 2.3 ± 0.1 nmol, 4.5 ± 0.1 nmol, 9.1 ± 0.1 nmol; n = 3, respectively) was investigated. The activity accumulation of [^{68}Ga]**35** in static PET scans at 1 h p.i. in kidneys and tumor-xenograft was quantified and the images were compared optically. Exemplary PET images of the same mouse (1 h p.i. of 0.28 nmol and 2.2 nmol [^{68}Ga]**35**, respectively) are shown in figure 24. Interestingly, the [^{68}Ga]**35** uptake in the LNCaP-tumor was marginally affected by increasing the amount of PSMA inhibitor by a factor of 16 (0.28 - 4.5 nmol). However, the tracer uptake in the kidneys was significantly reduced from 75.0 ± 9.4% ID/mL (mean value after injection of 0.27 ± 0.03 nmol [^{68}Ga]**35**) to 17.1 ± 8.4% ID/mL (mean value after injection of 2.3 ± 0.1 nmol [^{68}Ga]**35**) and 8.2 ± 1.9% ID/mL (mean value after injection of 4.5 ± 0.1 nmol [^{68}Ga]**35**). Application of 9.1 ± 0.1 nmol led to a decrease of tumor uptake of app. 50% and further reduction of kidney uptake to 2.6 ± 0.5 %ID/g (mean value).

This finding is in consistence with a recently reported new approach for nephroprotection in mice (249). In this study, the structurally independent PSMA inhibitor PMPA was injected into LNCaP-tumor bearing mice at 16 h p.i. of [^{125}I]MIP-1095 and at 1 h p.i. of [^{99m}Tc]MIP-1404, sustaining nearly complete tumor uptake while simultaneously achieving nearly total blocking of specific renal PSMA binding. The most efficient PMPA dose for injection of PMPA 16 h p.i. of [^{125}I]MIP-1095 in mice was 0.2 - 1 mg/kg (corresponding to 22.1 – 110.6 nmol in a 25 g mouse). However, since PMPA is not an approved pharmaceutical, the exclusion of potential pharmacologic effects is of major importance. Co-injection of PMPA or cold compound (as shown for [^{68}Ga]**35** in Fig. 24) seems to lead to a similar nephroprotective effect with application of significantly lower amounts of PSMA inhibitor and additionally provides a less complicated injection protocol.

Radiofluorinated NOTA-ligand [Al^{18}F]34: Due to the favorable *in vitro* results for PSMA inhibitor **34** and to investigate the tracer uptake at median time points (3 h p.i.), LNCaP-tumor bearing NOD-SCID mice were injected with [Al^{18}F]**34** and imaged at 1 h and 3 h p.i., respectively. At both time points, the tracer primarily accumulates in the tumor xenografts, kidneys and bladder, with high contrast to all other tissues (Fig. 25). No detectable activity in the bones proves the [Al^{18}F]NOTA-complex inertness against *in vivo* de-fluorination.

In accordance to the biodistribution data, PET images at 1 h p.i. and 3 h p.i. reveal a constant tumor uptake of [Al^{18}F]**34** in this time frame. In the biodistribution of [Al^{18}F]**39**, the

uptake in kidneys was also constant from 1 h to 3 h p.i., whereas a decrease in kidney SUV_{max} values was observed from 1 h to 3 h p.i. during PET imaging, resulting in tumor to kidney ratios of 0.6 ± 0.1 at 1 h p.i. (SUV_{max}(tumor) = 2.2 ± 0.3, SUV_{max} (kidney) = 3.8 ± 0.3; derived from PET data) increasing to 1.2 ± 0.3 at 3 h p.i. (SUV_{max}(tumor) = 2.0 ± 0.5, SUV_{max} (kidney) = 1.7 ± 0.2). This finding might be related to the 10-fold higher peptide amount injected for PET imaging of [Al^{18}F]**34** (3.0 nmol compared to 0.3 nmol in the biodistribution and 0.15 – 0.25 nmol in the previous studies with ^{68}Ga-labeled PSMA inhibitors).

Compared to [^{68}Ga]**R3** PET imaging (in the same animals), app. 20-fold higher peptide amounts were injected for [Al^{18}F]**34** (Fig. 25), since the specific activity of [Al^{18}F]**34** was significantly lower (92 GBq/µmol and 5 GBq/µmol, respectively). In accordance with the [^{68}Ga]**35** PET study on the "effect of the molar amount of peptide" (Fig. 24), a higher tracer uptake in all tissues, especially in the kidneys, was observed for [^{68}Ga]**R3** compared to [Al^{18}F]**34**. At 1 h p.i., the SUV_{max} values for tumor and kidneys were higher for [^{68}Ga]**R3** (SUV_{max}(tumor) = 5.4 ± 0.5, SUV_{max} (kidney) = 24.4 ± 1.4) compared to [Al^{18}F]**34**. On the other hand, the extent of renal excretion as determined by the bladder activity at 1 h p.i. was much lower for [^{68}Ga]**R3** compared to [Al^{18}F]**34**. If this finding is caused by differences in the two tracers or might be an effect of the applied amount of peptide needs to be investigated in further studies.

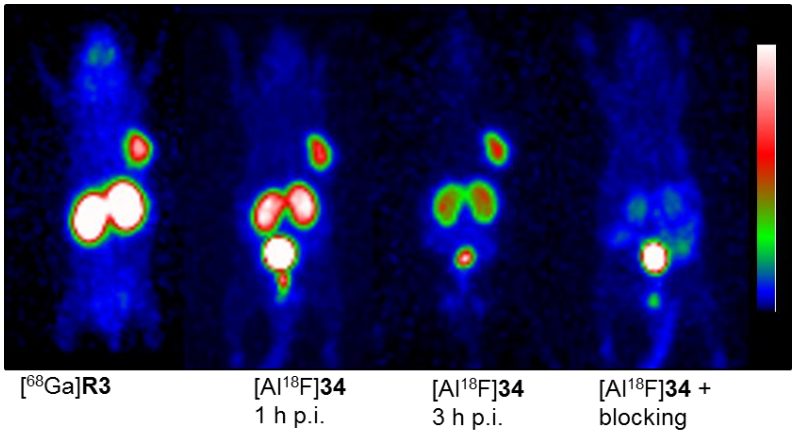

Figure 25. PET images of a LNCaP-tumor bearing NOD-SCID mouse (MIP) imaged at 1 h and 3 h p.i. of app. 15 MBq [Al^{18}F]**34** (app. 3.0 nmol) and after injection of [^{68}Ga]**R3** (app. 0.16 nmol) on the consecutive day. Other LNCaP-tumor bearing NOD-SCID mice were co-injected with [Al^{18}F]**34** and 8 mg/kg PMPA and PET images (MIP at 1 h p.i.) were recorded.

5.3.2 Tracer kinetic analysis (TACs)

With respect to comparability to the literature, the half-life of ^{68}Ga, and the excretion of the reference ligand [^{68}Ga]**R3**, all PET imaging and biodistribution studies (of the imaging agents) were performed at 1 h p.i.. Dynamic PET imaging offers determination of the optimal imaging/biodistribution time point, as well as investigation of organ uptake and excretion kinetics. Assuming a two-compartment model (136, 137) for the tracer kinetics *in vivo*, the activity signal should be steady in target-specific tissues, whereas non-specifically accumulated activity is characterized by a linear decrease of the graph in the logarithmic plot of time-activity curves (TACs). To investigate the tracer kinetics *in vivo*, LNCaP-tumor-bearing CD-1 nu/nu mice under isoflurane anaesthesia were injected with the radiotracers on bed and PET images were recorded for 90 min. In OSEM 3D reconstructed images, three dimensional ROIs were drawn, quantified and the resulting TACs for representative PSMA inhibitors are shown in figure 26.

Multimerization: Approaches to increase the targeting properties of PSMA inhibitors, like the DUPA-Pep-monomer [^{68}Ga]**9** (identical tracer uptake in tumor and muscle, which was constant over time), comprised multimerization resulting in a TRAP-based trimer [^{68}Ga]**10**. In contrast to the monomer, the trimeric [^{68}Ga]**10** exhibited higher tumor uptake and wash-out from non-target tissue, caused by the homotrimeric structure, which most likely conserves the targeting capacity for radiometabolites of [^{68}Ga]**10** in contrast to [^{68}Ga]**9**. The observed inter-individual differences were also reported for (monomeric) DUPA-Pep-based PSMA inhibitors in the literature (151). Thus, metabolic stabilization would be of major importance for monomeric inhibitors and might further increase the pharmacokinetics of multimeric PSMA inhibitors. However, the affinity of monomeric DUPA-Pep-based inhibitors was comparably lower than the affinity of the other PSMA inhibitors developed in this work (II.2.5 – II.2.11).

PSMA inhibitors with moderate metabolic stability: In consistence with the metabolite analysis (III.5.1) and the biodistribution data (III.5.2), the TACs of metabolically instable PSMA inhibitors [^{68}Ga]**R4**, [^{68}Ga]**12** and [^{68}Ga]**16** revealed unfavorable tumor-targeting due to unsatisfactory stability. Differences in the metabolic activity *in vivo* led to unintended retention of radio-metabolites in blood (ROI over the heart) and muscle ([^{68}Ga]**R4**, [^{68}Ga]**12**) or to a loss of specific accumulation in target tissue ([^{68}Ga]**16**), or both ([^{68}Ga]**9**). Due to the fast metabolization, the TACs representing the sum of all radiometabolites cannot provide additional information on the pharmacokinetics of the intact tracers.

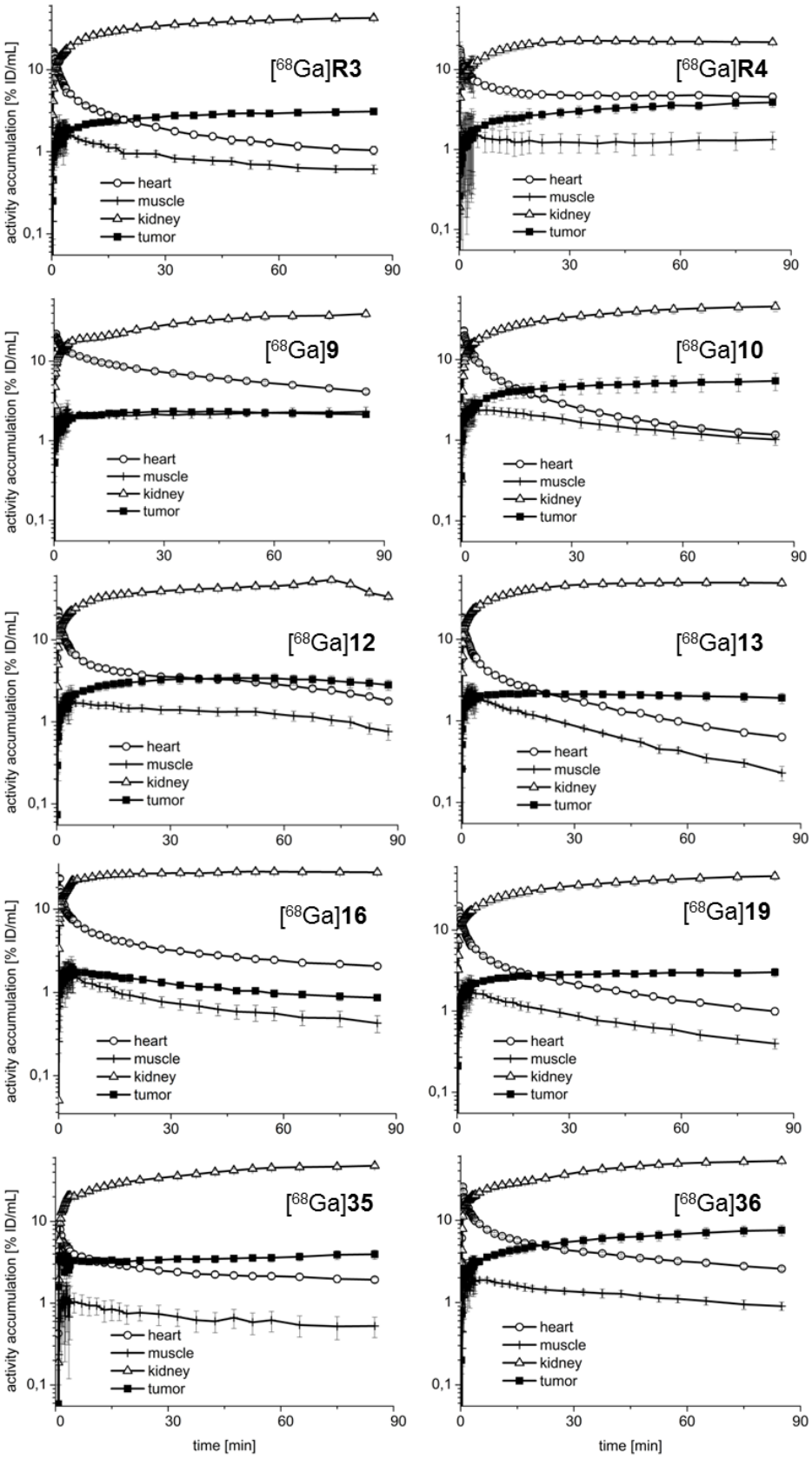

Figure 26. TACs (logarithmic plot) in % ID/mL derived from dynamic PET data (90 min acquisition time, OSEM 3D reconstruction) in blood pool (heart), muscle, kidneys and LNCaP tumor xenograft. Tumor-bearing CD-1 nu/nu mice were injected with app. 15 MBq (0.15 - 0.25 nmol) [^{68}Ga]R3, [^{68}Ga]**R4**, [^{68}Ga]**9**, [^{68}Ga]**10**, [^{68}Ga]**12**, [^{68}Ga]**13**, [^{68}Ga]**16**, [^{68}Ga]**19**, [^{68}Ga]**35** and [^{68}Ga]**36**, respectively.

Metabolically stable PSMA inhibitors: Metabolic stabilization via substitution of L-amino acid spacers by D-amino acid spacers, led to the metabolically stable PSMA inhibitor [^{68}Ga]**13** (ffk spacer). The TACs (Fig. 26) obtained from [^{68}Ga]**13**-PET (Fig. 26) represent the optimal situation of a two-compartment model, which is considered to be ideal for an imaging agent. A plateau in PSMA-positive (tumor and kidney) and logarithmic washout from PSMA-negative compartments (blood and muscle) were observed. The reference ligand [^{68}Ga]**R3** ([^{68}Ga]HBED-CC-Ahx-KuE) revealed PSMA-specific uptake in tumor and kidneys (steady signal from 30 to 90 min) and wash-out from blood pool and muscle (both PSMA-unspecific). Besides [^{68}Ga]**R3**, a non-logarithmic decrease of the TACs (Fig. 26) in blood and muscle were also observed for [^{68}Ga]**19** ((I-y)fk spacer) and for [^{68}Ga]**35** (y-nal-k spacer), indicating a more complicated uptake/excretion mechanism than described by the two-compartment model. However, the metabolically stable PSMA inhibitors [^{68}Ga]**13**, [^{68}Ga]**19** and [^{68}Ga]**35** exhibited a high and persistent tumor uptake, together with fast and efficient clearance kinetics from non-target tissue, which are important parameters for PET imaging agents.

S1-accessory lipophilic pocket: The higher retention of [^{68}Ga]**36** in the blood pool and a slight increase of kidney and tumor activity over the 1.5 h observation period (Fig. 26) are in consistence with the increased plasma-protein binding of this radiopharmaceutical. In the [^{68}Ga]**36** TACs of a 1.5 h observation period, the plasma-protein bound activity seems to be delivered to PSMA-specific organs and therefore leads to an increase in tumor uptake with time. However, due to the comparably high blood level, the image contrast at 1 h p.i. was lower compared to [^{68}Ga]**19** or [^{68}Ga]**35**.

For endoradiotherapeutic application, the increased activity in the blood together with high metabolic stability of the radiopharmaceutical led to a high and persistent tumor retention of [^{177}Lu]**36** in the biodistribution at 24 h p.i. (Fig. 21). Compared to [^{177}Lu]**19** and [^{177}Lu]**35**, the deceleration of the pharmacokinetics and the excretion of radiolabeled **36** delivers higher radiation doses to the target tissue during endoradiotherapy. However, the likewise increased renal uptake of the endoradiotherapeutic (Fig. 21) has to be considered in terms of kidney toxicity. At early time points (up to 3 h) an increased peptide amount (Fig. 24 and 25) improved the tumor to kidney ratio by reducing the renal uptake of the radiopharmaceuticals [^{68}Ga]**35** and [Al^{18}F]**34**. If the combination of a PSMA inhibitor with decelerated pharmacokinetics ([^{177}Lu]**36**) and increased peptide concentrations might synergistically improve tumor radiation or/and reduce nephrotoxicity has to be further investigated in humans.

6 HUMAN APPLICATIONS

The most promising candidates in preclinical evaluation are transferred to the clinic for first in human applications. The radiolabeled PSMA inhibitor **19** was used for ^{68}Ga-PET imaging, ^{111}In-SPECT/radioguided surgery, and ^{177}Lu-endoradiotherapeutic treatment of PCa patients. Due to the theranostic applicability, **19** was termed PSMA I&T (for imaging and therapy).

6.1 [^{68}Ga]PSMA I&T PET imaging

First clinical application of [^{68}Ga]PSMA I&T ([^{68}Ga]**19**) in PET/CT of a patient suffering from mCRPC (Fig. 27A) successfully demonstrated detection of multiple metastatic foci in different organs and tissues with very high lesion to background ratios of 17.6 - 35.2 as early as 1 h p.i.. The primary tumor (SUV_{max}: 65.1, Fig. 27B), periprostatic tissue and urinary bladder invasion was not concealed by tracer excretion into the bladder. The liver lesion (Fig. 27C), not known before PET scanning, showed a SUV_{max} of 10.9 and 2 cm in diameter. Multiple paraaortic and pelvic lymph nodes showed high contrast in [^{68}Ga]PSMA I&T PET, as shown for a 8 mm sized paraaortic lymph node with a SUV_{max} of 39.4 in Fig. 27D. Further, a sclerosis in a sternal lesion, that had been barely visible in the CT image, exhibited very high [^{68}Ga]PSMA I&T uptake (SUV_{max}:76.4; Fig. 27E). Background activity was determined in gluteal musculature (SUV_{max} = 1.5). Comparable to previously reported data for [^{68}Ga]HBED-CC-Ahx-KuE ([^{68}Ga]**R3**) in PET/CT (154), low physiological tracer uptake was observed in liver (251), spleen (251) and intestine (18), and - to a higher extent - in proximal tubules of the kidneys (18) and salivary glands (74), all of which are organs with documented moderate to high PSMA expression. However, the reasons for the observed high tracer uptake into salivary glands is still a matter of debate, since the PSMA expression level would suggest lower uptake.

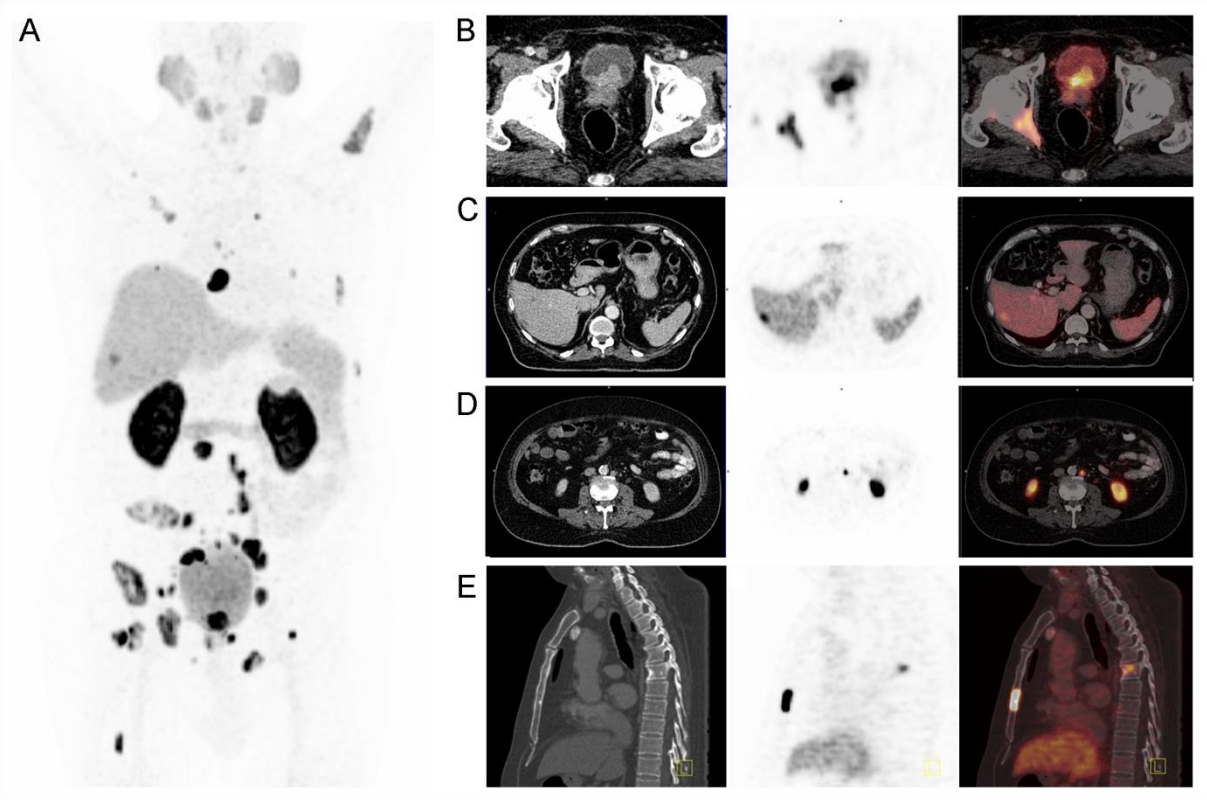

Figure 27. [^{68}Ga]PSMA I&T PET/CT of patient 1. **A.** Whole body MIP showing one liver lesion as well as multiple lymph node and bone metastases. **B.** Transaxial slices show infiltration of a soft-tissue mass with increased tracer uptake in the urinary bladder, and periprostatic tissue. **C.** Transaxial slices revealing [^{68}Ga]PSMA I&T uptake in the right lobe of the liver with a hypodense lesion in corresponding CT slice. **D.** Transaxial slices presenting a small paraaortic lymph node with intense PSMA-expression indicative of a lymph node metastasis. **E.** Sagittal reformatted CT reveals only minimal sclerosis of a sternal bone metastasis with high [^{68}Ga]PSMA I&T uptake. All slices are shown on CT (left), PET (middle), and fused PET/CT (right panel).(252)

6.2 [^{111}In]PSMA I&T radioguided surgery

In patients with primary PCa the use of near-infrared-fluorescence or radioguided surgery after injection of indigocyanine green or ^{99m}Tc-labeled nanocolloids into the prostate has been proposed for guiding sentinel lymph node resection (253). However, the tracer injection site remains unclear and in recurrent disease lymph drainage might be altered.

For initial PSMA-targeted radioguided surgery an ^{111}In-labeled PSMA inhibitor was selected because of its favorable half-life of 2.8 days. Preoperative PET was performed using [^{68}Ga]HBED-CC-Ahx-KuE ([^{68}Ga]**R3**) to ensure comparability to the literature (157, 217). However, due to complex instability of [^{111}In]HBED-CC-Ahx-KuE (III.2.4), the DOTAGA-

conjugated PSMA inhibitor PSMA I&T (**19**) was used for ^{111}In-labeling and PSMA-targeted radioguided surgery in an initial proof-of-concept human study (161).

Intraoperatively, the use of PSMA-targeted radioguided surgery after administration of [^{111}In]PSMA I&T increased surgeon confidence to detect and completely resect especially small metastatic lesions seen in preoperative [^{68}Ga]HBED-CC-Ahx-KuE PET hybrid imaging. The γ-sonde together with resected tissue specimens is exemplarily shown in Fig. 28. Macrometastases (high signal in radioguided surgery) were also detected by preoperative [^{68}Ga]HBED-CC-Ahx-KuE PET. In patient 2 PSMA-targeted [^{111}In]PSMA I&T-guided surgery detected additional lesions nearby the known tumor deposits corresponding to very small metastatic lesions of 2 – 4 mm. All resected tissue specimens exhibiting positive measurements *in vivo* and *ex vivo,* demonstrated PSMA expression in immunohistochemistry (161). No patient experienced complications related to i.v. administration of [^{111}In]PSMA I&T (161). Therefore, based on these initial results, PSMA-targeted radioguided surgery using [^{111}In]PSMA I&T seems to be of additional value in the treatment of local metastatic PCa, and therefore merits further investigation in a larger group of patients.

Figure 28. The γ-sonde with the optical tracking system (declipseSPECT, SurgicEye, Munich, Germany) was used for [^{111}In]PSMA I&T radioguided surgery. Resected lymph node specimens were rated as negative, weak, medium or strong positive by *ex vivo* acoustic measurement.

6.3 [^{177}Lu]PSMA I&T endoradiotherapy

For initial proof-of-concept PSMA-targeted endoradiotherapy, two patients suffering from mCRPC, which had been confirmed by baseline [^{68}Ga]HBED-CC-Ahx-KuE ([^{68}Ga]**R3**) PET/CT, were treated with [^{177}Lu]PSMA I&T ([^{177}Lu]**19**). Therapy control was performed using [^{68}Ga]HBED-CC-Ahx-KuE PET/CT to ensure comparability to data from the literature (154-156, 158, 217) and thus a more objective interpretation of the therapy outcome.

In patient 3 (PSA = 54.2 ng/mL) the mediastinal lymph node metastases (SUV_{max}: 36.5, determined by [^{68}Ga]HBED-CC-Ahx-KuE PET/CT) exhibited a high, specific and rapid uptake of [^{177}Lu]PSMA I&T (Fig. 29). As expected, significant tracer uptake is also observed for kidneys, spleen and salivary glands, but also in the small intestine. This is consistent with the PSMA expression levels documented for these tissues (18, 74, 251); for example, [^{177}Lu]PSMA I&T uptake in the small intestine most likely is the result of PSMA expression in human intestine (18), where the physiological function of PSMA is mediating folate absorption (43).

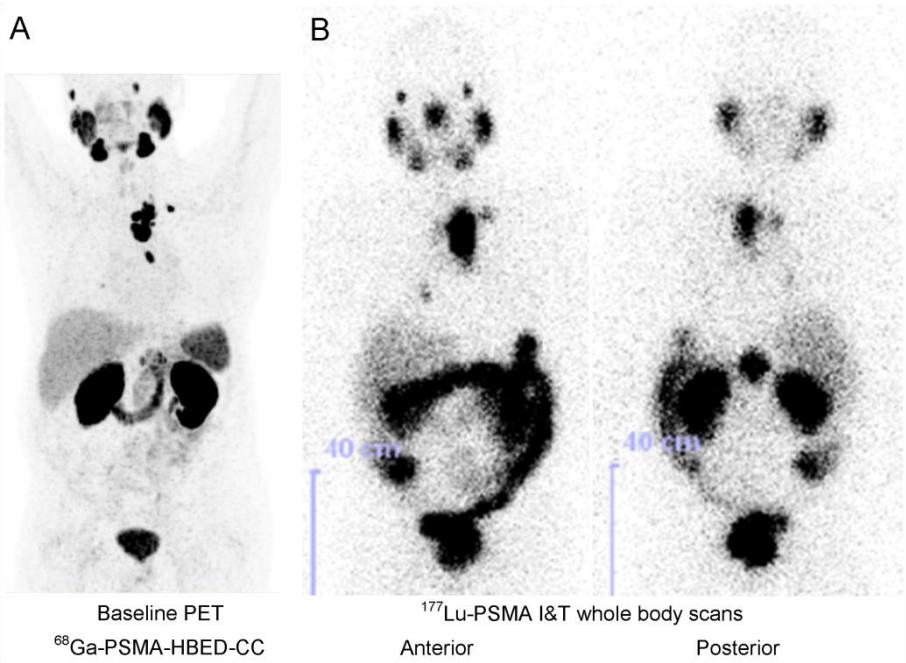

Figure 29. Patient 3. **A.** MIP of [^{68}Ga]HBED-CC-Ahx-KuE PET/CT (164 MBq, 60 min p.i., left) showed intense tracer accumulation in mediastinal lymph node metastases. **B.** Correspondingly, these mediastinal lymph nodes demonstrated a high [^{177}Lu]PSMA I&T uptake 47 h after therapy with 5.7 GBq [^{177}Lu]PSMA I&T.(252)

The baseline [^{68}Ga]HBED-CC-Ahx-KuE PET/CT scan in patient 4 (PSA: 40.2 ng/mL) demonstrated PSMA-mediated uptake in the primary tumor as well as multiple lymph node and bone metastases (Fig. 30A). The SUV_{max} of target lesions were 26.3 in right paraaortic lymph node (transverse PET/CT image in upper row), 25.2 in interaortocaval lymph node (middle row) and 16.4 in the primary tumor in the prostate (lower row). The patient underwent one therapy cycle with 8.0 GBq [^{177}Lu]PSMA I&T. Based on the high PSMA expression in the metastases of mCRPC (254) and the resulting high uptake of [^{177}Lu]PSMA I&T in these lesions, therapeutically effective doses were delivered to the PCa metastases resulting in partial remission of many of the intense PSMA positive metastases depicted by [^{68}Ga]HBED-CC-Ahx-KuE PET/CT (Fig. 30B, SUV_{max} values of 3.0, 3.5 and 5.1 in paraaortic, interaortocaval lymph node metastases and primary tumor, respectively) accompanied by a significant drop in the PSA to 0.7 ng/mL. Clinically, a symptomatic pain relief, especially on the left side of the chest, was reported.

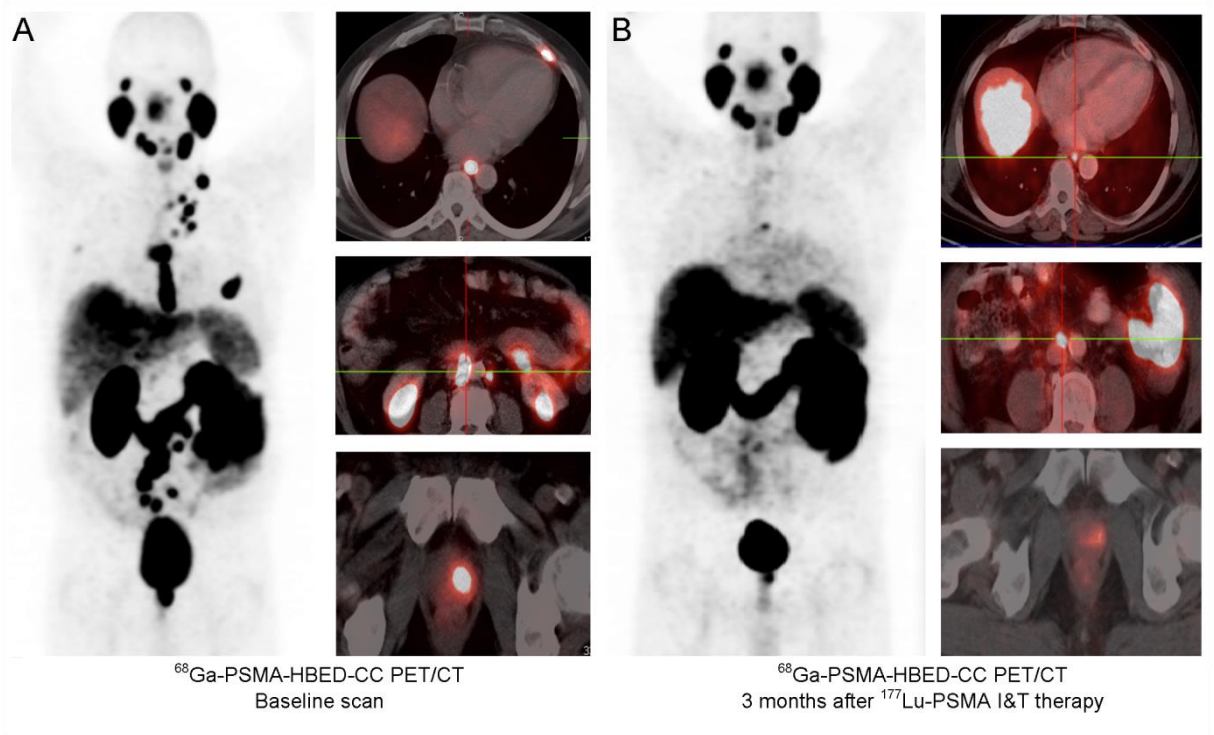

Figure 30. PET/CT in patient 4. **A.** Baseline PET/CT 65 min after i.v. administration of 176 MBq [^{68}Ga]HBED-CC-Ahx-KuE. **B.** Follow-up scan with 180 MBq [^{68}Ga]HBED-CC-Ahx-KuE (60 min. p.i.) performed 3 months after [^{177}Lu]PSMA I&T therapy (8.0 GBq).(252)

Due to the rapid renal wash-out and blood clearance of [^{177}Lu]PSMA I&T, therapy was well tolerated and no significant fall in blood counts, renal function (serum creatinine, tubular extraction rate) or in any of the laboratory parameters was found. However, in a recently published first-in-humans study on endoradiotherapy of PCa using [^{131}I]MIP-1095 (185) dry mouth and one case of mucositis were reported due to high salivary gland retention of the therapeutic agent. Thus, therapeutic effectiveness with no detectable side effects qualifies [^{177}Lu]PSMA I&T to be a valid choice for application in therapy of PCa.

For application in patients ^{131}I-labeling of MIP-1095 resulted in specific activities below 0.24 GBq/µmol (185), whereas 60 GBq/µmol were obtained for ^{177}Lu-labeling of PSMA I&T in this study. Since comparable activity amounts were administered to the patients in both studies (up to 8 GBq), the molar amount of PSMA inhibitor injected was drastically lower for [^{177}Lu]PSMA I&T compared to [^{131}I]MIP-1095. For PET imaging using [^{18}F]DCFBC very high specific activities of 1,190 ± 894 GBq/µmol were applied, resulting in drastically different salivary gland and blood pool activities (159) compared to the above mentioned endoradiotherapeutic agents and other PET or SPECT tracers in the literature (127, 154). Therefore not only the choice of the best radiopharmaceutical for imaging and endoradiotherapy of PCa, but also the influence of the administered molar amount of PSMA inhibitor on the biodistribution of the respective radiopharmaceuticals needs to be elaborated in further studies. In a preclinical study, Kratochwil and co-workers (249) investigated the influence of increasing PMPA concentrations on the [^{125}I]MIP-1095 displacement in mouse xenografts and kidneys. Injection of 0.2 – 1 mg/kg (22 – 110 nmol in a 25 g mouse) PMPA 16 h p.i. appears to be optimal for sustaining nearly complete tumor uptake while simultaneously achieving near-total blocking of specific renal PSMA binding. The PET/biodistribution of [Al^{18}F]**34**, confirmed by PET imaging with increasing peptide amounts using [^{68}Ga]**35** (III.5.3), proved the feasibility of a co-injection of cold peptide with an optimal tumor-to-kidney ratio of 2.3 – 4.5 nmol. Future studies have to show the optimal clinical peptide amount and injection timing (tracer co-injection or PMPA injection at a distinct time after tracer injection).

IV CONCLUSION AND PERSPECTIVES

For targeting of imaging as well as therapeutic agents to PCa, the enzyme PSMA is a valuable choice, due to its selective expression pattern being further increased with advanced malignancy of PCa cells. In this work, three chemical approaches towards the development of PSMA inhibitors were made 1) small molecule PSMA inhibitors for SiFA [^{18}F]radiofluorination, 2) mono- and trimeric inhibitors based on DUPA-Pep and 3) derivatives of DOTA-FFK(Sub-KuE), which were labeled with a variety of radionuclides, such as ^{18}F ([Al^{18}F]**34**), ^{68}Ga ([^{68}Ga]**19**, [^{68}Ga]**35**), ^{111}In ([^{111}In]**19**), ^{64}Cu ([^{64}Cu]**34**), and ^{177}Lu ([^{177}Lu]**19**, [^{177}Lu]**36**).

Most likely due to the high lipophilicity of the SiFA-motif, all SiFA-containing PSMA inhibitors (**5** - **7**) revealed low affinity to PSMA. If the SiFA moiety might be conjugated to a PSMA inhibitor with even longer distance between the KuE motif (PSMA-active center binding) and SiFA (isotope-exchange radiofluorination motif), conjugation of sugar moieties or other polar groups might compensate for lipophilicity and improve binding affinity and pharmacokinetics of these PSMA inhibitors.

In a comparative evaluation of gallium chelates of chelator-conjugated FFK(Sub-KuE)-inhibitors **R4** (DOTA), **12** (DOTAGA) and **14** (NOPO), the affinity as well as internalization was two-fold higher for the DOTAGA-conjugated inhibitor **12**. Since radiolabeling properties of DOTAGA with ^{68}Ga, as well as ^{177}Lu were comparable to that of DOTA, all further developed PSMA inhibitors for theranostic and therapeutic applications were coupled to the DOTAGA-chelator.

To overcome the drawback of metabolic instability (III.5.1), leading to suboptimal tumor targeting and increased background signal (III.5.2) of radiolabeled FFK-derivatives, such as [^{68}Ga]**R4** (99), **12**, and **14**, and iodo-tyrosine derivatives [^{68}Ga]**16** - **18**, the L-amino acids in the spacer between the KuE motif and the radiometal-chelator were substituted by D-amino acids. The D-amino acids containing PSMA inhibitors **13** (ffk spacer) and **19** ((I-y)fk spacer) revealed high metabolic stability and favorable pharmacokinetics *in vivo*. For the metabolically instable DUPA-Pep-based inhibitors [^{68}Ga]**8** and [^{68}Ga]**9**, a TRAP-trimer [^{68}Ga]**10**, synthesized via a click-chemistry strategy, revealed a 15-fold higher affinity and significantly improved tumor targeting *in vivo*. Thus, as shown for RGD-peptides, multimerization is also an efficient tool for affinity improvement of PSMA inhibitors, but with respect to the optimal targeting peptide (DUPA-Pep is metabolically instable *in vivo*) not fully exploited yet.

Besides the chelator and the stereochemistry of the amino acids in the spacer, also the spacer amino acid composition influences the affinity to PSMA. Substitution of

phenylalanine-by-iodo-tyrosine resulted in a three-fold increase in internalization for NOPO-conjugated PSMA inhibitor [^{125}I]**15** in comparison to [^{68}Ga]**14**, and an increase from 44 ± 2% to 75 ± 2% of [^{125}I]**R1** for DOTAGA-conjugated inhibitors [^{177}Lu]**13** (ffk spacer) compared to [^{177}Lu]**19** ((I-y)fk spacer). Bulky lipophilic residues, such as biphenylalanine in PSMA inhibitor **27** revealed lower affinity, most likely due to unfavorable interactions with the narrow 20 Å long funnel leading to the active center of the PSMA-enzyme. The optimized inhibitors **28**, **29**, and **35** with a tyrosine-naphthylalanine-lysine spacer (III.3.7) showed even increased affinity compared to phenylalanine-phenylalanine-lysine or iodo-tyrosine-phenylalanine-lysine spacers.

For initial proof-of-concept, [^{68}Ga]**19** ([^{68}Ga]PSMA I&T) was applied in PET/CT imaging in one patient. As early as 1 p.i. [^{68}Ga]PSMA I&T revealed high uptake in lymph node metastases (average SUV_{max} of 17.6), bone metastases (average SUV_{max} of 35.2) and a liver metastasis (SUV_{max} of 20.7). Together with a low background signal (III.6.1) [^{68}Ga]PSMA I&T leads to favorable image contrast, which is in consistence with recently published dosimetry data calculated from [^{68}Ga]PSMA I&T PET images of five patients (255).

^{111}In-labeling of PSMA I&T was shown to yield a PSMA inhibitor with high affinity to PSMA and even increased internalization into PSMA-expressing cells compared to the ^{68}Ga- and ^{177}Lu-counterparts. Initial proof-of-concept application of [^{111}In]PSMA I&T in radioguided surgery for the resection of lymph node metastases of PCa successfully demonstrated the feasibility of this approach. Increased sensitivity in detection of metastases and higher surgeon confidence for resection of single metastases in PCa patients compared to conventional surgery underlines the potential clinical value of PSMA-targeted [^{111}In]PSMA I&T radioguided surgery.

For development of a bimodal probe, a fluorescent dye was attached to the DOTAGA-conjugated PSMA inhibitor **22** and although dyes are lipophilic and bulky, the inhibitor affinity to PSMA was only marginally affected. Due to metabolic instability of the (I-Y)(I-Y)K-spacer, synthesis of a metabolically stable inhibitor for *in vivo* application is highly recommended.

A first proof-of-concept ^{177}Lu-endoradiotherapy using [^{177}Lu]PSMA I&T was conducted. Initial patient applications of [^{177}Lu]PSMA I&T revealed high uptake in PSMA-positive tumor lesions (determined by [^{68}Ga]HBED-CC-Ahx-KuE PET/CT). Three months after [^{177}Lu]PSMA I&T-endoradiotherapy, partial remission of the intense [^{68}Ga]HBED-CC-Ahx-KuE uptake, a significant drop of PSA, and a subjective pain relief (III.6.3) were observed. However, greater patient cohorts as well as long-term follow-up are needed for [^{68}Ga/^{111}In/^{177}Lu]PSMA I&T to confirm these initial encouraging results and to determine the possible role of radiolabeled PSMA I&T or other PSMA-targeting agents in clinical routine.

Within this work, the affinity of PSMA inhibitors for therapeutic application was increased from 54.7 ± 6.1 nM ([^{177}Lu]**R4**) to 7.9 ± 2.4 nM ([^{177}Lu]**19**) and 6.1 ± 1.6 nM ([^{177}Lu]**36**), correlating with an improved internalization from 19.3 ± 0.9% for [^{177}Lu]**R4** to 118.6 ± 0.5% for [^{177}Lu]**36** (after 60 min on LNCaP cells; as % of [^{125}I]**R1**). [^{177}Lu]**36** contains a iodo-phenylalanine group causing an almost quantitative plasma-protein binding (81% for [^{177}Lu]**35** and 97% for [^{177}Lu]**36**), and an increase in lipophilicity (log$P_{(o/w)}$ = -3.1 ± 0.02). A tumor retention of 16.1 ± 2.5% ID/g compared to 4.5 ± 1.1 and 2.7 ± 0.5% ID/g for [^{177}Lu]**35** and [^{177}Lu]**19** at 24 h p.i., respectively, can be explained by interactions with the S1-accessory lipophilic pocket of PSMA and/or the subsequent delivery of [^{177}Lu]**36** from the plasma-protein bound "reservoir" (III.3.9). Due to the long tumor retention of [^{177}Lu]**36**, endoradiotherapeutic treatment of PCa using [^{177}Lu]**36** might even be more efficient compared to [^{177}Lu]**19**.

Caused by the high PSMA expression in the kidneys, the kidneys are the dose limiting organs for PSMA-targeted endoradiotherapeutic treatment of PCa. Dosimetry calculations from mouse to human showed, that unless more than 9.6 GBq or 14.4 GBq [^{177}Lu]PSMA I&T (depending on the extrapolation method) are administered to humans, the limiting kidney dose of 23 Gy could be exceeded (unpublished data). However, after injection of 150 MBq [^{68}Ga]PSMA I&T a dose of 33 mGy was reported for the kidneys (255), which might be caused by differences in the expression density between mouse and man (I.2.1). Unfortunately, we could not confirm the kidney-specific cleavage of the glycyl-lysine motif to reduce the tracer uptake in the kidneys for [^{68}Ga]**20** and [^{68}Ga]**21** ("kidney cleavable" inhibitors). However, for [^{68}Ga]**35** increasing the amount of peptide to 2.3 – 4.5 nmol lead to a significantly higher tumor-to-kidney ratio (lower kidney uptake) in LNCaP-tumor bearing mice, most likely due to a high first-pass extraction from the blood to the kidneys, which is lower (or slower) for the tumor. A detailed study comparing the co-injection of unlabeled peptide or a recently reported approach on [^{125}I]MIP-1095 displacement by injection of app. 22 – 110 nmol PMPA 16 h p.i. in LNCaP-tumor bearing mice has to show the optimal kidney protection strategy.

V SUPPLEMENTARY MATERIAL

1 FIGURE AND TABLE INDEX

Figures

Tables

2 ABBREVIATIONS

Ahx aminohexanoic acid

A_S specific activity [GBq/µmol]

Boc *tert*-butyloxycarbonyl (protecting group)

BSA bovine serum albumin

CDI carbonyldiimidazole

DCC dicyclohexylcarbodiimide

DCM dichloromethane

DCE dichloroethane

Dde *N*-(1-(4,4-dimethyl-2,6-dioxocyclohexylidene)ethyl) (protecting group)

DIC *N*,*N*-diisopropylcarbodiimide

DMAP 4-(dimethylamino)pyridine

DMF *N,N*-dimethylformamide

DMSO dimethylsulfoxide

DOTA 1,4,7,10-tetraazacyclododecane-1,4,7,10-tetraacetic acid

DOTAGA 1,4,7,10-tetraazacyclododecane,1-(glutaric acid)-4,7,10-triacetic acid

DIPEA *N,N*-diisopropylethylamine

EDC 1-ethyl-3-(3-dimethylaminopropyl)carbodiimide

EDTA ethylenediaminetetraacetic acid

FCS fetal calf serum

[^{18}F]FACBC trans-1-amino-3-[^{18}F]fluorocyclobutanecarboxylic acid

FDA Food and Drug Administration

[^{18}F]FDG 2-[^{18}F]fluorodesoxyglucose

[^{18}F]FDHT 16-β-[^{18}F]fluoro-5-α-dihydrotestosterone

Fmoc 9-fluorenylmethyloxycarbonyl (protecting group)

FOV field-of-view

HATU O-(7-azabenzotriazol-1-yl)-*N,N,N′,N′*-tetramethyluronium hexafluoro-phosphate

HBED-CC *N*,*N′*-bis[2-hydroxy-5-(carboxyethyl)benzyl]ethylenediamine-*N*,*N′*-diace-tic acid

HBSS Hank's buffered salt solution (Biochrom AG, Germany)

HEPES 2-(4-(2-hydroxyethyl)-1-piperazinyl)-ethanesulfonic acid

HOAt 1-hydroxy-7-azabenzotriazole

HOBt 1-hydroxybenzotriazole

HPLC high-performance liquid chromatography

IC_{50}	half maximal inhibitory concentration
Iodogen	1,3,4,6-tetrachloro-3R,6R-diphenylglycoluril
I-Y / I-y	3-iodo-L-tyrosine / 3-iodo-D-tyrosine
KuE	((S)-5-amino-1-carboxypentyl)carbamoyl)-L-glutamic acid
NAAG	*N*-acetyl-L-aspartyl-L-glutamate
NAALADase	*N*-acetylated-α-linked acidic dipeptidase
NMP	*N*-methyl-pyrrolidon
NOPO	1,4,7-triazacyclononane-1,4-bis[methylene (hydroxymethyl)phosphinic acid]-7-[methylene(2-carboxyethyl)phosphinic acid]
NOTA	1,4,7-triazacyclononane-triacetic acid
NHS	*N*-hydroxysuccinimide
PBS	phosphate-buffered saline (Biochrom AG, Germany)
PHI	prostate health index
PCa	prostate cancer
PET	positron-emission tomography
PMPA	2-(phosphonomethyl)pentane-1,5-dioic acid
PSA	prostate-specific antigen
PSMA	prostate-specific membrane antigen
rt	room temperature
SiFA-BA	4-di-*tert*-butylfluorosilanebenzoic acid
SPECT	single-photon emission computed tomography
tBu	*tert*-butyl (protecting group)
TBTU	*O*-(1H-benzotriazol-1-yl)-*N,N,N',N'*-tetramethyluronium-tetrafluoro-borate
TCP	tritylchloride polystyrene
TEA	triethylamine
TFA	trifluoroacetic acid
TIPS	triisopropylsilane
TLC	thin-layer chromatography
TRAP	1,4,7-triazacyclononane-triphosphinic acid

3 REFERENCES

1. Haberland J WU, Barnes B, Bertz J, Dahm S, Laudi A, Kraywinkel K. Kurzfristige Prognosen der Krebsmortalität in Deutschland bis 2015. UMID. 2012;3/2012: 17-23.
2. Schröder FH, Hugosson J, Roobol MJ, Tammela TLJ, Ciatto S, Nelen V, et al. Screening and Prostate-Cancer Mortality in a Randomized European Study. New England Journal of Medicine. 2009;360(13):1320-8.
3. Andriole GL, Crawford ED, Grubb RL, 3rd, Buys SS, Chia D, Church TR, et al. Prostate cancer screening in the randomized Prostate, Lung, Colorectal, and Ovarian Cancer Screening Trial: mortality results after 13 years of follow-up. Journal of the National Cancer Institute. 2012;104(2):125-32.
4. Heijnsdijk EAM, Wever EM, Auvinen A, Hugosson J, Ciatto S, Nelen V, et al. Quality-of-Life Effects of Prostate-Specific Antigen Screening. New England Journal of Medicine. 2012;367(7):595-605.
5. Stone NN, Crawford ED. To screen or nor to screen: the prostate cancer dilemma. Asian journal of andrology. 2015;17(1):44-5.
6. Smith DS, Humphrey PA, Catalona WJ. The early detection of prostate carcinoma with prostate specific antigen: the Washington University experience. Cancer. 1997;80(9):1852-6.
7. Jadvar H. Prostate Cancer: PET with (18)F-FDG, (18)F- or (11)C-Acetate, and (18)F- or (11)C-Choline. Journal of nuclear medicine : official publication, Society of Nuclear Medicine. 2011;52(1):81-9.
8. Thompson IM, Pauler DK, Goodman PJ, Tangen CM, Lucia MS, Parnes HL, et al. Prevalence of prostate cancer among men with a prostate-specific antigen level < or =4.0 ng per milliliter. N Engl J Med. 2004;350(22):2239-46.
9. Humphrey PA. Gleason grading and prognostic factors in carcinoma of the prostate. Mod Pathol. 2004;17(3):292-306.
10. Draisma G, Boer R, Otto SJ, van der Cruijsen IW, Damhuis RA, Schroder FH, et al. Lead times and overdetection due to prostate-specific antigen screening: estimates from the European Randomized Study of Screening for Prostate Cancer. Journal of the National Cancer Institute. 2003;95(12):868-78.
11. Mease RC. Radionuclide Based Imgaing of Prostate Cancer. Current Topics in Medicinal Chemistry. 2010;10:1600-16.
12. Mohammed A. Biomarkers in prostate cancer: new era and prospective. Med Oncol. 2014;31(8):1-6.
13. Hessels D, Schalken JA. The use of PCA3 in the diagnosis of prostate cancer. Nature reviews Urology. 2009;6(5):255-61.
14. Dotan ZA. Bone imaging in prostate cancer. Nat Clin Pract Urol. 2008;5(8):434-44.
15. Pal RP, Thiruudaian T, Khan MA. When is a bone scan study appropriate in asymptomatic men diagnosed with prostate cancer? Asian journal of andrology. 2008;10(6):890-5.
16. Zhou J, Neale JH, Pomper MG, Kozikowski AP. NAAG peptidase inhibitors and their potential for diagnosis and therapy. Nat Rev Drug Discov. 2005;4(12):1015-26.
17. Berger UV, Carter RE, McKee M, Coyle JT. N-acetylated alpha-linked acidic dipeptidase is expressed by non-myelinating Schwann cells in the peripheral nervous system. J Neurocytol. 1995;24(2):99-109.
18. Silver DA, Pellicer I, Fair WR, Heston WD, Cordon-Cardo C. Prostate-specific membrane antigen expression in normal and malignant human tissues. Clin Cancer Res. 1997;3(1):81-5.
19. Bostwick DG, Pacelli A, Blute M, Roche P, Murphy GP. Prostate specific membrane antigen expression in prostatic intraepithelial neoplasia and adenocarcinoma: a study of 184 cases. Cancer. 1998;82(11):2256-61.
20. Sacha P, Zamecnik J, Barinka C, Hlouchova K, Vicha A, Mlcochova P, et al. Expression of glutamate carboxypeptidase II in human brain. Neuroscience. 2007;144(4):1361-72.
21. Robinson MB, Blakely RD, Couto R, Coyle JT. Hydrolysis of the brain dipeptide N-acetyl-L-aspartyl-L-glutamate. Identification and characterization of a novel N-acetylated alpha-linked acidic dipeptidase activity from rat brain. J Biol Chem. 1987;262(30):14498-506.
22. Slusher BS, Robinson MB, Tsai G, Simmons ML, Richards SS, Coyle JT. Rat brain N-acetylated alpha-linked acidic dipeptidase activity. Purification and immunologic characterization. J Biol Chem. 1990;265(34):21297-301.
23. Berger UV, Carter RE, Coyle JT. The immunocytochemical localization of N-acetylaspartyl glutamate, its hydrolysing enzyme NAALADase, and the NMDAR-1 receptor at a vertebrate neuromuscular junction. Neuroscience. 1995;64(4):847-50.

24. Carter RE, Feldman AR, Coyle JT. Prostate-specific membrane antigen is a hydrolase with substrate and pharmacologic characteristics of a neuropeptidase. Proceedings of the National Academy of Sciences of the United States of America. 1996;93(2):749-53.
25. Benveniste H, Drejer J, Schousboe A, Diemer NH. Elevation of the extracellular concentrations of glutamate and aspartate in rat hippocampus during transient cerebral ischemia monitored by intracerebral microdialysis. J Neurochem. 1984;43(5):1369-74.
26. Fagg GE, Foster AC, Ganong AH. Excitatory amino acid synaptic mechanisms and neurological function. Trends in pharmacological sciences. 1986;7(0):357-63.
27. Butcher SP, Bullock R, Graham DI, McCulloch J. Correlation between amino acid release and neuropathologic outcome in rat brain following middle cerebral artery occlusion. Stroke. 1990;21(12):1727-33.
28. Shaw PJ, Ince PG. Glutamate, excitotoxicity and amyotrophic lateral sclerosis. J Neurol. 1997;244 Suppl 2:S3-14.
29. Slusher BS, Vornov JJ, Thomas AG, Hurn PD, Harukuni I, Bhardwaj A, et al. Selective inhibition of NAALADase, which converts NAAG to glutamate, reduces ischemic brain injury. Nat Med. 1999;5(12):1396-402.
30. Ghadge GD, Slusher BS, Bodner A, Canto MD, Wozniak K, Thomas AG, et al. Glutamate carboxypeptidase II inhibition protects motor neurons from death in familial amyotrophic lateral sclerosis models. Proceedings of the National Academy of Sciences. 2003;100(16):9554-9.
31. Yamamoto T, Nozaki-Taguchi N, Sakashita Y. Spinal N-acetyl-alpha-linked acidic dipeptidase (NAALADase) inhibition attenuates mechanical allodynia induced by paw carrageenan injection in the rat. Brain Res. 2001;909(1-2):138-44.
32. Yamamoto T, Nozaki-Taguchi N, Sakashita Y, Inagaki T. Inhibition of spinal N-acetylated-alpha-linked acidic dipeptidase produces an antinociceptive effect in the rat formalin test. Neuroscience. 2001;102(2):473-9.
33. Chen SR, Wozniak KM, Slusher BS, Pan HL. Effect of 2-(phosphono-methyl)-pentanedioic acid on allodynia and afferent ectopic discharges in a rat model of neuropathic pain. J Pharmacol Exp Ther. 2002;300(2):662-7.
34. Majer P, Jackson PF, Delahanty G, Grella BS, Ko YS, Li W, et al. Synthesis and biological evaluation of thiol-based inhibitors of glutamate carboxypeptidase II: discovery of an orally active GCP II inhibitor. J Med Chem. 2003;46(10):1989-96.
35. Carpenter KJ, Sen S, Matthews EA, Flatters SL, Wozniak KM, Slusher BS, et al. Effects of GCP-II inhibition on responses of dorsal horn neurones after inflammation and neuropathy: an electrophysiological study in the rat. Neuropeptides. 2003;37(5):298-306.
36. Kozikowski AP, Zhang J, Nan F, Petukhov PA, Grajkowska E, Wroblewski JT, et al. Synthesis of urea-based inhibitors as active site probes of glutamate carboxypeptidase II: efficacy as analgesic agents. J Med Chem. 2004;47(7):1729-38.
37. Zhang W, Slusher B, Murakawa Y, Wozniak KM, Tsukamoto T, Jackson PF, et al. GCPII (NAALADase) inhibition prevents long-term diabetic neuropathy in type 1 diabetic BB/Wor rats. J Neurol Sci. 2002;194(1):21-8.
38. Jackson PF, Cole DC, Slusher BS, Stetz SL, Ross LE, Donzanti BA, et al. Design, synthesis, and biological activity of a potent inhibitor of the neuropeptidase N-acetylated alpha-linked acidic dipeptidase. J Med Chem. 1996;39(2):619-22.
39. Navratil M, Ptacek J, Sacha P, Starkova J, Lubkowski J, Barinka C, et al. Structural and biochemical characterization of the folyl-poly-gamma-l-glutamate hydrolyzing activity of human glutamate carboxypeptidase II. The FEBS journal. 2014;281(14):3228-42.
40. Zhao R, Matherly LH, Goldman ID. Membrane transporters and folate homeostasis: intestinal absorption and transport into systemic compartments and tissues. Expert Rev Mol Med. 2009;11:e4.
41. Tasch J, Gong M, Sadelain M, Heston WD. A unique folate hydrolase, prostate-specific membrane antigen (PSMA): a target for immunotherapy? Crit Rev Immunol. 2001;21(1-3):249-61.
42. Ghosh A, Heston WD. Tumor target prostate specific membrane antigen (PSMA) and its regulation in prostate cancer. J Cell Biochem. 2004;91(3):528-39.
43. Pinto JT, Suffoletto BP, Berzin TM, Qiao CH, Lin S, Tong WP, et al. Prostate-specific membrane antigen: A novel folate hydrolase in human prostatic carcinoma cells. Clin Cancer Res. 1996;2(9):1445-51.
44. Heston WD. Characterization and glutamyl preferring carboxypeptidase function of prostate specific membrane antigen: a novel folate hydrolase. Urology. 1997;49(3A Suppl):104-12.
45. Barinka C, Rojas C, Slusher B, Pomper M. Glutamate carboxypeptidase II in diagnosis and treatment of neurologic disorders and prostate cancer. Current medicinal chemistry. 2012;19(6):856-70.

46. Su SL, Huang IP, Fair WR, Powell CT, Heston WD. Alternatively spliced variants of prostate-specific membrane antigen RNA: ratio of expression as a potential measurement of progression. Cancer Res. 1995;55(7):1441-3.
47. Tiffany CW, Lapidus RG, Merion A, Calvin DC, Slusher BS. Characterization of the enzymatic activity of PSM: comparison with brain NAALADase. The Prostate. 1999;39(1):28-35.
48. Sweat SD, Pacelli A, Murphy GP, Bostwick DG. Prostate-specific membrane antigen expression is greatest in prostate adenocarcinoma and lymph node metastases. Urology. 1998;52(4):637-40.
49. Schulke N, Varlamova OA, Donovan GP, Ma D, Gardner JP, Morrissey DM, et al. The homodimer of prostate-specific membrane antigen is a functional target for cancer therapy. Proceedings of the National Academy of Sciences of the United States of America. 2003;100(22):12590-5.
50. Rycyna KJ, Bacich DJ, O'Keefe DS. Opposing roles of folate in prostate cancer. Urology. 2013;82(6):1197-203.
51. Tomaszewski JJ, Cummings JL, Parwani AV, Dhir R, Mason JB, Nelson JB, et al. Increased cancer cell proliferation in prostate cancer patients with high levels of serum folate. The Prostate. 2011;71(12):1287-93.
52. Zhang Y, Guo Z, Du T, Chen J, Wang W, Xu K, et al. Prostate specific membrane antigen (PSMA): a novel modulator of p38 for proliferation, migration, and survival in prostate cancer cells. The Prostate. 2013;73(8):835-41.
53. Yao V, Bacich DJ. Prostate specific membrane antigen (PSMA) expression gives prostate cancer cells a growth advantage in a physiologically relevant folate environment in vitro. The Prostate. 2006;66(8):867-75.
54. Yao V, Berkman CE, Choi JK, O'Keefe DS, Bacich DJ. Expression of prostate-specific membrane antigen (PSMA), increases cell folate uptake and proliferation and suggests a novel role for PSMA in the uptake of the non-polyglutamated folate, folic acid. The Prostate. 2010;70(3):305-16.
55. Liu T, Wu LY, Fulton MD, Johnson JM, Berkman CE. Prolonged androgen deprivation leads to downregulation of androgen receptor and prostate-specific membrane antigen in prostate cancer cells. Int J Oncol. 2012;41(6):2087-92.
56. Verburg FA, Krohn T, Heinzel A, Mottaghy FM, Behrendt FF. First evidence of PSMA expression in differentiated thyroid cancer using [Ga]PSMA-HBED-CC PET/CT. Eur J Nucl Med Mol Imaging. 2015.
57. Liu H, Moy P, Kim S, Xia Y, Rajasekaran A, Navarro V, et al. Monoclonal antibodies to the extracellular domain of prostate-specific membrane antigen also react with tumor vascular endothelium. Cancer Res. 1997;57(17):3629-34.
58. Chang SS, O'Keefe DS, Bacich DJ, Reuter VE, Heston WD, Gaudin PB. Prostate-specific membrane antigen is produced in tumor-associated neovasculature. Clin Cancer Res. 1999;5(10):2674-81.
59. Chang SS, Reuter VE, Heston WD, Gaudin PB. Metastatic renal cell carcinoma neovasculature expresses prostate-specific membrane antigen. Urology. 2001;57(4):801-5.
60. Baccala A, Sercia L, Li J, Heston W, Zhou M. Expression of prostate-specific membrane antigen in tumor-associated neovasculature of renal neoplasms. Urology. 2007;70(2):385-90.
61. Al-Ahmadie HA, Olgac S, Gregor PD, Tickoo SK, Fine SW, Kondagunta GV, et al. Expression of prostate-specific membrane antigen in renal cortical tumors. Mod Pathol. 2008;21(6):727-32.
62. Haffner MC, Kronberger IE, Ross JS, Sheehan CE, Zitt M, Muhlmann G, et al. Prostate-specific membrane antigen expression in the neovasculature of gastric and colorectal cancers. Human pathology. 2009;40(12):1754-61.
63. Wernicke AG, Edgar MA, Lavi E, Liu H, Salerno P, Bander NH, et al. Prostate-specific membrane antigen as a potential novel vascular target for treatment of glioblastoma multiforme. Archives of pathology & laboratory medicine. 2011;135(11):1486-9.
64. Zeng C, Ke ZF, Yang Z, Wang Z, Yang SC, Luo CQ, et al. Prostate-specific membrane antigen: a new potential prognostic marker of osteosarcoma. Med Oncol. 2012;29(3):2234-9.
65. Abdel-Hadi M, Ismail Y, Younis L. Prostate-specific membrane antigen (PSMA) immunoexpression in the neovasculature of colorectal carcinoma in Egyptian patients. Pathol Res Pract. 2014;210(11):759-63.
66. Wernicke AG, Varma S, Greenwood EA, Christos PJ, Chao KS, Liu H, et al. Prostate-specific membrane antigen expression in tumor-associated vasculature of breast cancers. APMIS. 2014;122(6):482-9.
67. Nomura N, Pastorino S, Jiang P, Lambert G, Crawford JR, Gymnopoulos M, et al. Prostate specific membrane antigen (PSMA) expression in primary gliomas and breast cancer brain metastases. Cancer cell international. 2014;14(1):26.

68. Bacich DJ, Pinto JT, Tong WP, Heston WD. Cloning, expression, genomic localization, and enzymatic activities of the mouse homolog of prostate-specific membrane antigen/NAALADase/folate hydrolase. Mammalian genome : official journal of the International Mammalian Genome Society. 2001;12(2):117-23.
69. Aggarwal S, Ricklis RM, Williams SA, Denmeade SR. Comparative study of PSMA expression in the prostate of mouse, dog, monkey, and human. The Prostate. 2006;66(9):903-10.
70. Weineisen M, Schottelius M, Simecek J, Eiber M, Schwaiger M, Wester H. Development and first in human evaluation of PSMA I&T - A ligand for diagnostic imaging and endoradiotherapy of prostate cancer. J Nucl Med. 2014;55:1083.
71. Weineisen M, Simecek J, Schottelius M, Schwaiger M, Wester H-J. Synthesis and preclinical evaluation of DOTAGA-conjugated PSMA ligands for functional imaging and endoradiotherapy of prostate cancer. EJNMMI Research. 2014;4(1):63.
72. Rawlings ND, Barrett AJ. Structure of membrane glutamate carboxypeptidase. Biochimica et biophysica acta. 1997;1339(2):247-52.
73. Rawlings ND, Barrett AJ, Bateman A. MEROPS: the peptidase database. Nucleic Acids Res. 2010;38(Database issue):D227-33.
74. Israeli RS, Powell CT, Corr JG, Fair WR, Heston WD. Expression of the prostate-specific membrane antigen. Cancer Res. 1994;54(7):1807-11.
75. Israeli RS, Powell CT, Fair WR, Heston WD. Molecular cloning of a complementary DNA encoding a prostate-specific membrane antigen. Cancer Res. 1993;53(2):227-30.
76. O'Keefe DS, Su SL, Bacich DJ, Horiguchi Y, Luo Y, Powell CT, et al. Mapping, genomic organization and promoter analysis of the human prostate-specific membrane antigen gene. Biochimica et biophysica acta. 1998;1443(1-2):113-27.
77. Anilkumar G, Rajasekaran SA, Wang S, Hankinson O, Bander NH, Rajasekaran AK. Prostate-specific membrane antigen association with filamin A modulates its internalization and NAALADase activity. Cancer Res. 2003;63(10):2645-8.
78. Rajasekaran SA, Anilkumar G, Oshima E, Bowie JU, Liu H, Heston W, et al. A novel cytoplasmic tail MXXXL motif mediates the internalization of prostate-specific membrane antigen. Mol Biol Cell. 2003;14(12):4835-45.
79. Anilkumar G, Barwe SP, Christiansen JJ, Rajasekaran SA, Kohn DB, Rajasekaran AK. Association of prostate-specific membrane antigen with caveolin-1 and its caveolae-dependent internalization in microvascular endothelial cells: implications for targeting to tumor vasculature. Microvasc Res. 2006;72(1-2):54-61.
80. Goodman OB, Jr., Barwe SP, Ritter B, McPherson PS, Vasko AJ, Keen JH, et al. Interaction of prostate specific membrane antigen with clathrin and the adaptor protein complex-2. Int J Oncol. 2007;31(5):1199-203.
81. Liu H, Rajasekaran AK, Moy P, Xia Y, Kim S, Navarro V, et al. Constitutive and antibody-induced internalization of prostate-specific membrane antigen. Cancer Res. 1998;58(18):4055-60.
82. Mesters JR, Barinka C, Li W, Tsukamoto T, Majer P, Slusher BS, et al. Structure of glutamate carboxypeptidase II, a drug target in neuronal damage and prostate cancer. The EMBO Journal. 2006;25(6):1375-84.
83. Barinka C, Starkova J, Konvalinka J, Lubkowski J. A high-resolution structure of ligand-free human glutamate carboxypeptidase II. Acta crystallographica Section F, Structural biology and crystallization communications. 2007;63(Pt 3):150-3.
84. Rong SB, Zhang J, Neale JH, Wroblewski JT, Wang S, Kozikowski AP. Molecular modeling of the interactions of glutamate carboxypeptidase II with its potent NAAG-based inhibitors. J Med Chem. 2002;45(19):4140-52.
85. Davis MI, Bennett MJ, Thomas LM, Bjorkman PJ. Crystal structure of prostate-specific membrane antigen, a tumor marker and peptidase. Proceedings of the National Academy of Sciences of the United States of America. 2005;102(17):5981-6.
86. Barinka C, Hlouchova K, Rovenska M, Majer P, Dauter M, Hin N, et al. Structural basis of interactions between human glutamate carboxypeptidase II and its substrate analogs. Journal of molecular biology. 2008;376(5):1438-50.
87. Stoermer D, Vitharana D, Hin N, Delahanty G, Duvall B, Ferraris DV, et al. Design, Synthesis, and Pharmacological Evaluation of Glutamate Carboxypeptidase II (GCPII) Inhibitors Based on Thioalkylbenzoic Acid Scaffolds. Journal of Medicinal Chemistry. 2012;55(12):5922-32.
88. Barinka C, Byun Y, Dusich CL, Banerjee SR, Chen Y, Castanares M, et al. Interactions between human glutamate carboxypeptidase II and urea-based inhibitors: structural characterization. J Med Chem. 2008;51(24):7737-43.
89. Stoermer D, Liu Q, Hall MR, Flanary JM, Thomas AG, Rojas C, et al. Synthesis and biological evaluation of hydroxamate-Based inhibitors of glutamate carboxypeptidase II. Bioorg Med Chem Lett. 2003;13(13):2097-100.

90. Choy CJ, Fulton MD, Davis AL, Hopkins M, Choi JK, Anderson MO, et al. Rationally designed sulfamides as glutamate carboxypeptidase II inhibitors. Chemical biology & drug design. 2013;82(5):612-9.
91. Pavlicek J, Ptacek J, Barinka C. Glutamate carboxypeptidase II: an overview of structural studies and their importance for structure-based drug design and deciphering the reaction mechanism of the enzyme. Current medicinal chemistry. 2012;19(9):1300-9.
92. Ferraris DV, Shukla K, Tsukamoto T. Structure-activity relationships of glutamate carboxypeptidase II (GCPII) inhibitors. Current medicinal chemistry. 2012;19(9):1282-94.
93. Pavlicek J, Ptacek J, Cerny J, Byun Y, Skultetyova L, Pomper MG, et al. Structural characterization of P1'-diversified urea-based inhibitors of glutamate carboxypeptidase II. Bioorg Med Chem Lett. 2014;24(10):2340-5.
94. Mlcochova P, Plechanovova A, Barinka C, Mahadevan D, Saldanha JW, Rulisek L, et al. Mapping of the active site of glutamate carboxypeptidase II by site-directed mutagenesis. The FEBS journal. 2007;274(18):4731-41.
95. Barinka C, Rovenska M, Mlcochova P, Hlouchova K, Plechanovova A, Majer P, et al. Structural insight into the pharmacophore pocket of human glutamate carboxypeptidase II. J Med Chem. 2007;50(14):3267-73.
96. Vitharana D, France JE, Scarpetti D, Bonneville GW, Majer P, Tsukamoto T. Synthesis and biological evaluation of (R)- and (S)-2-(phosphonomethyl)pentanedioic acids as inhibitors of glutamate carboxypeptidase II. Tetrahedron: Asymmetry. 2002;13(15):1609-14.
97. Tsukamoto T, Majer P, Vitharana D, Ni C, Hin B, Lu XC, et al. Enantiospecificity of glutamate carboxypeptidase II inhibition. J Med Chem. 2005;48(7):2319-24.
98. Mesters JR, Henning K, Hilgenfeld R. Human glutamate carboxypeptidase II inhibition: structures of GCPII in complex with two potent inhibitors, quisqualate and 2-PMPA. Acta crystallographica Section D, Biological crystallography. 2007;63(Pt 4):508-13.
99. Eder M, Schafer M, Bauder-Wust U, Hull WE, Wangler C, Mier W, et al. 68Ga-complex lipophilicity and the targeting property of a urea-based PSMA inhibitor for PET imaging. Bioconjug Chem. 2012;23(4):688-97.
100. Apolo AB, Pandit-Taskar N, Morris MJ. Novel tracers and their development for the imaging of metastatic prostate cancer. J Nucl Med. 2008;49(12):2031-41.
101. Bouchelouche K, Tagawa ST, Goldsmith SJ, Turkbey B, Capala J, Choyke P. PET/CT Imaging and Radioimmunotherapy of Prostate Cancer. Semin Nucl Med. 2011;41(1):29-44.
102. Castellucci P, Jadvar H. PET/CT in prostate cancer: non-choline radiopharmaceuticals. Q J Nucl Med Mol Imaging. 2012;56(4):367-74.
103. Foss C, Mease R, Cho S, Kim H, Pomper M. GCPII Imaging and Cancer. Current medicinal chemistry. 2012;19(9):1346-59.
104. Cherry SR, Sorenson JA, Phelps ME. chapter 13 - The Gamma Camera: Basic Principles. In: Phelps SRCASE, editor. Physics in Nuclear Medicine (Fourth Edition). Philadelphia: W.B. Saunders; 2012. p. 195-208.
105. Peterson TE, Furenlid LR. SPECT detectors: the Anger Camera and beyond. Physics in medicine and biology. 2011;56(17):R145-R82.
106. Dorenbos P, de Haas JTM, van Eijk CWE. Non-proportionality in the scintillation response and the energy resolution obtainable with scintillation crystals. Nuclear Science, IEEE Transactions on. 1995;42(6):2190-202.
107. van der Have F, Vastenhouw B, Ramakers RM, Branderhorst W, Krah JO, Ji C, et al. U-SPECT-II: An Ultra-High-Resolution Device for Molecular Small-Animal Imaging. J Nucl Med. 2009;50(4):599-605.
108. Islamian JP, Azazrm A, Mahmoudian B, Gharapapagh E. Advances in Pinhole and Multi-Pinhole Collimators for Single Photon Emission Computed Tomography Imaging. World Journal of Nuclear Medicine. 2015;14(1):3-9.
109. Gullberg GT, Reutter BW, Sitek A, Maltz JS, Budinger TF. Dynamic single photon emission computed tomography—basic principles and cardiac applications. Physics in Medicine and Biology. 2010;55(20):R111-R91.
110. Magill J PG, Galy J. Karlsruher Nuklidkarte. In: Communities E, editor. 2006-2009.
111. Sodee DB, Malguria N, Faulhaber P, Resnick MI, Albert J, Bakale G. Multicenter ProstaScint imaging findings in 2154 patients with prostate cancer. The ProstaScint Imaging Centers. Urology. 2000;56(6):988-93.
112. Troyer JK, Feng Q, Beckett ML, Wright GL, Jr. Biochemical characterization and mapping of the 7E11-C5.3 epitope of the prostate-specific membrane antigen. Urologic oncology. 1995;1(1):29-37.
113. Troyer JK, Beckett ML, Wright GL, Jr. Location of prostate-specific membrane antigen in the LNCaP prostate carcinoma cell line. The Prostate. 1997;30(4):232-42.

114. Tykvart J, Navratil V, Sedlak F, Corey E, Colombatti M, Fracasso G, et al. Comparative analysis of monoclonal antibodies against prostate-specific membrane antigen (PSMA). The Prostate. 2014;74(16):1674-90.
115. Vallabhajosula S, Kuji I, Hamacher KA, Konishi S, Kostakoglu L, Kothari PA, et al. Pharmacokinetics and biodistribution of 111In- and 177Lu-labeled J591 antibody specific for prostate-specific membrane antigen: prediction of 90Y-J591 radiation dosimetry based on 111In or 177Lu? J Nucl Med. 2005;46(4):634-41.
116. Olson WC, Heston WD, Rajasekaran AK. Clinical trials of cancer therapies targeting prostate-specific membrane antigen. Reviews on recent clinical trials. 2007;2(3):182-90.
117. Nedrow-Byers JR, Jabbes M, Jewett C, Ganguly T, He H, Liu T, et al. A phosphoramidate-based prostate-specific membrane antigen-targeted SPECT agent. The Prostate. 2012;72(8):904-12.
118. Nedrow-Byers JR, Moore AL, Ganguly T, Hopkins MR, Fulton MD, Benny PD, et al. PSMA-targeted SPECT agents: mode of binding effect on in vitro performance. The Prostate. 2013;73(4):355-62.
119. Banerjee SR, Foss CA, Castanares M, Mease RC, Byun Y, Fox JJ, et al. Synthesis and evaluation of technetium-99m- and rhenium-labeled inhibitors of the prostate-specific membrane antigen (PSMA). J Med Chem. 2008;51(15):4504-17.
120. Kularatne SA, Zhou Z, Yang J, Post CB, Low PS. Design, synthesis, and preclinical evaluation of prostate-specific membrane antigen targeted (99m)Tc-radioimaging agents. Mol Pharm. 2009;6(3):790-800.
121. Banerjee SR, Pullambhatla M, Byun Y, Nimmagadda S, Foss CA, Green G, et al. Sequential SPECT and Optical Imaging of Experimental Models of Prostate Cancer with a Dual Modality Inhibitor of the Prostate-Specific Membrane Antigen. Angewandte Chemie (International Ed in English). 2011;50(39):9167-70.
122. Hillier SM, Maresca KP, Lu G, Merkin RD, Marquis JC, Zimmerman CN, et al. 99mTc-labeled small-molecule inhibitors of prostate-specific membrane antigen for molecular imaging of prostate cancer. J Nucl Med. 2013;54(8):1369-76.
123. Lu G, Maresca KP, Hillier SM, Zimmerman CN, Eckelman WC, Joyal JL, et al. Synthesis and SAR of (9)(9)mTc/Re-labeled small molecule prostate specific membrane antigen inhibitors with novel polar chelates. Bioorg Med Chem Lett. 2013;23(5):1557-63.
124. Vallabhajosula S, Nikolopoulou A, Babich JW, Osborne JR, Tagawa ST, Lipai I, et al. 99mTc-labeled small-molecule inhibitors of prostate-specific membrane antigen: pharmacokinetics and biodistribution studies in healthy subjects and patients with metastatic prostate cancer. J Nucl Med. 2014;55(11):1791-8.
125. Hillier SM, Maresca KP, Femia FJ, Marquis JC, Foss CA, Nguyen N, et al. Preclinical evaluation of novel glutamate-urea-lysine analogues that target prostate-specific membrane antigen as molecular imaging pharmaceuticals for prostate cancer. Cancer Res. 2009;69(17):6932-40.
126. Maresca KP, Hillier SM, Femia FJ, Keith D, Barone C, Joyal JL, et al. A series of halogenated heterodimeric inhibitors of prostate specific membrane antigen (PSMA) as radiolabeled probes for targeting prostate cancer. J Med Chem. 2009;52(2):347-57.
127. Barrett JA, Coleman RE, Goldsmith SJ, Vallabhajosula S, Petry NA, Cho S, et al. First-in-man evaluation of 2 high-affinity PSMA-avid small molecules for imaging prostate cancer. J Nucl Med. 2013;54(3):380-7.
128. Turkington TG. Introduction to PET instrumentation. J Nucl Med Technol. 2001;29(1):4-11.
129. Cherry SR, Sorenson JA, Phelps ME. chapter 3 - Modes of Radioactive Decay. In: Phelps SRCASE, editor. Physics in Nuclear Medicine (Fourth Edition). Philadelphia: W.B. Saunders; 2012. p. 19-30.
130. Cherry SR, Sorenson JA, Phelps ME. chapter 18 - Positron Emission Tomography. In: Phelps SRCASE, editor. Physics in Nuclear Medicine (Fourth Edition). Philadelphia: W.B. Saunders; 2012. p. 307-43.
131. Thie JA. Understanding the standardized uptake value, its methods, and implications for usage. J Nucl Med. 2004;45(9):1431-4.
132. Cherry SR, Sorenson JA, Phelps ME. chapter 17 - Single Photon Emission Computed Tomography. In: Phelps SRCASE, editor. Physics in Nuclear Medicine (Fourth Edition). Philadelphia: W.B. Saunders; 2012. p. 279-306.
133. Khalil MM, Tremoleda JL, Bayomy TB, Gsell W. Molecular SPECT Imaging: An Overview. International Journal of Molecular Imaging. 2011;2011:796025.
134. Fahey FH. Positron emission tomography instrumentation. Radiol Clin North Am. 2001;39(5):919-29.
135. Turkington T. PET Imaging Basics. In: Shreve P, Townsend DW, editors. Clinical PET-CT in Radiology: Springer New York; 2011. p. 21-8.

136. Gunn RN, Gunn SR, Cunningham VJ. Positron Emission Tomography Compartmental Models. J Cereb Blood Flow Metab. 2001;21(6):635-52.
137. Watabe H, Ikoma Y, Kimura Y, Naganawa M, Shidahara M. PET kinetic analysis—compartmental model. Annals of nuclear medicine. 2006;20(9):583-8.
138. Cherry SR, Sorenson JA, Phelps ME. chapter 21 - Tracer Kinetic Modeling. In: Phelps SRCASE, editor. Physics in Nuclear Medicine (Fourth Edition). Philadelphia: W.B. Saunders; 2012. p. 379-405.
139. Vallabhajosula S, Goldsmith SJ, Hamacher KA, Kostakoglu L, Konishi S, Milowski MI, et al. Prediction of myelotoxicity based on bone marrow radiation-absorbed dose: radioimmunotherapy studies using 90Y- and 177Lu-labeled J591 antibodies specific for prostate-specific membrane antigen. J Nucl Med. 2005;46(5):850-8.
140. Tagawa ST, Milowsky MI, Morris M, Vallabhajosula S, Christos P, Akhtar NH, et al. Phase II study of Lutetium-177-labeled anti-prostate-specific membrane antigen monoclonal antibody J591 for metastatic castration-resistant prostate cancer. Clin Cancer Res. 2013;19(18):5182-91.
141. Pandit-Taskar N, O'Donoghue JA, Beylergil V, Lyashchenko S, Ruan S, Solomon SB, et al. (89)Zr-huJ591 immuno-PET imaging in patients with advanced metastatic prostate cancer. Eur J Nucl Med Mol Imaging. 2014;41(11):2093-105.
142. Schuchardt C, Wiessalla S, Kulkarni HR, Mueller D, Bartlett D, Ho D, et al. Biodistribution and Dosimetry of In-111 PSMA Minibody (IAb2M-DOTA): First Results. Eur J Nucl Med Mol Imaging. 2013;40:S246-S7.
143. Pomper MG, Musachio JL, Zhang J, Scheffel U, Zhou Y, Hilton J, et al. 11C-MCG: synthesis, uptake selectivity, and primate PET of a probe for glutamate carboxypeptidase II (NAALADase). Mol Imaging. 2002;1(2):96-101.
144. Chen Y, Pullambhatla M, Foss CA, Byun Y, Nimmagadda S, Senthamizhchelvan S, et al. 2-(3-{1-Carboxy-5-[(6-[18F]fluoro-pyridine-3-carbonyl)-amino]-pentyl}-ureido)-pen tanedioic acid, [18F]DCFPyL, a PSMA-based PET imaging agent for prostate cancer. Clin Cancer Res. 2011;17(24):7645-53.
145. Mease RC, Dusich CL, Foss CA, Ravert HT, Dannals RF, Seidel J, et al. N-[N-[(S)-1,3-Dicarboxypropyl]carbamoyl]-4-[18F]fluorobenzyl-L-cysteine, [18F]DCFBC: a new imaging probe for prostate cancer. Clin Cancer Res. 2008;14(10):3036-43.
146. Al-Momani E, Malik N, Machulla HJ, Reske SN, Solbach C. Radiosynthesis of [18F]FEt-Tyr-urea-Glu ([18F]FEtTUG) as a new PSMA ligand. J Radioanal Nucl Chem. 2013;295(3):2289-94.
147. Graham K, Lesche R, Gromov AV, Bohnke N, Schafer M, Hassfeld J, et al. Radiofluorinated derivatives of 2-(phosphonomethyl)pentanedioic acid as inhibitors of prostate specific membrane antigen (PSMA) for the imaging of prostate cancer. J Med Chem. 2012;55(22):9510-20.
148. Lesche R, Kettschau G, Gromov AV, Bohnke N, Borkowski S, Monning U, et al. Preclinical evaluation of BAY 1075553, a novel (18)F-labelled inhibitor of prostate-specific membrane antigen for PET imaging of prostate cancer. Eur J Nucl Med Mol Imaging. 2014;41(1):89-101.
149. Malik N, Machulla HJ, Solbach C, Winter G, Reske SN, Zlatopolskiy B. Radiosynthesis of a new PSMA targeting ligand ([18F]FPy-DUPA-Pep). Appl Radiat Isot. 2011;69(7):1014-8.
150. Malik N, Zlatopolskiy B, Machulla H-J, Reske SN, Solbach C. One pot radiofluorination of a new potential PSMA ligand [Al18F]NOTA-DUPA-Pep. Journal of Labelled Compounds and Radiopharmaceuticals. 2012;55(9):320-5.
151. Winter G, Zlatopolskiy B, Kull T, Bertram J, Genze F, Cudek G, et al. 68Ga-DOTA-DUPA-Pep as a new peptide conjugate for molecular imaging of prostate carcinoma. J NUCL MED MEETING ABSTRACTS. 2011;52(1_MeetingAbstracts):1597-.
152. Baur B, Solbach C, Andreolli E, Winter G, Machulla HJ, Reske SN. Synthesis, Radiolabelling and In Vitro Characterization of the Gallium-68-, Yttrium-90- and Lutetium-177-Labelled PSMA Ligand, CHX-A''-DTPA-DUPA-Pep. Pharmaceuticals (Basel). 2014;7(5):517-29.
153. Banerjee SR, Pullambhatla M, Byun Y, Nimmagadda S, Green G, Fox JJ, et al. 68Ga-labeled inhibitors of prostate-specific membrane antigen (PSMA) for imaging prostate cancer. J Med Chem. 2010;53(14):5333-41.
154. Afshar-Oromieh A, Malcher A, Eder M, Eisenhut M, Linhart HG, Hadaschik BA, et al. PET imaging with a [68Ga]gallium-labelled PSMA ligand for the diagnosis of prostate cancer: biodistribution in humans and first evaluation of tumour lesions. Eur J Nucl Med Mol Imaging. 2013;40(4):486-95.
155. Afshar-Oromieh A, Zechmann CM, Malcher A, Eder M, Eisenhut M, Linhart HG, et al. Comparison of PET imaging with a (68)Ga-labelled PSMA ligand and (18)F-choline-based PET/CT for the diagnosis of recurrent prostate cancer. Eur J Nucl Med Mol Imaging. 2014;41(1):11-20.
156. Eiber M, Nekolla SG, Maurer T, Weirich G, Wester HJ, Schwaiger M. Ga-PSMA PET/MR with multimodality image analysis for primary prostate cancer. Abdominal imaging. 2014.
157. Maurer T, Eiber M, Krause BJ. Molecular multimodal hybrid imaging in prostate and bladder cancer. Der Urologe Ausg A. 2014;53(4):469-83.

158. Afshar-Oromieh A, Avtzi E, Giesel FL, Holland-Letz T, Linhart HG, Eder M, et al. The diagnostic value of PET/CT imaging with the Ga-labelled PSMA ligand HBED-CC in the diagnosis of recurrent prostate cancer. Eur J Nucl Med Mol Imaging. 2014.
159. Cho SY, Gage KL, Mease RC, Senthamizhchelvan S, Holt DP, Jeffrey-Kwanisai A, et al. Biodistribution, tumor detection, and radiation dosimetry of 18F-DCFBC, a low-molecular-weight inhibitor of prostate-specific membrane antigen, in patients with metastatic prostate cancer. J Nucl Med. 2012;53(12):1883-91.
160. Beheshti M, Kunit T, Haim S, Zakavi R, Schiller C, Stephens A, et al. BAY 1075553 PET-CT for Staging and Restaging Prostate Cancer Patients: Comparison with [F] Fluorocholine PET-CT (Phase I Study). Mol Imaging Biol. 2014.
161. Maurer T, Weirich G, Schottelius M, Weineisen M, Frisch B, Okur A, et al. Prostate-specific Membrane Antigen-radioguided Surgery for Metastatic Lymph Nodes in Prostate Cancer. Eur Urol. 2015;68(3):530-4.
162. Ntziachristos V. Going deeper than microscopy: the optical imaging frontier in biology. Nat Meth. 2010;7(8):603-14.
163. Weissleder R, Ntziachristos V. Shedding light onto live molecular targets. Nat Med. 2003;9(1):123-8.
164. Chin PTK, Beekman CAC, Buckle T, Josephson L, van Leeuwen FWB. Multispectral visualization of surgical safety-margins using fluorescent marker seeds. American Journal of Nuclear Medicine and Molecular Imaging. 2012;2(2):151-62.
165. Lutje S, Rijpkema M, Franssen GM, Fracasso G, Helfrich W, Eek A, et al. Dual-Modality Image-Guided Surgery of Prostate Cancer with a Radiolabeled Fluorescent Anti-PSMA Monoclonal Antibody. J Nucl Med. 2014;55(6):995-1001.
166. Liu T, Wu LY, Kazak M, Berkman CE. Cell-Surface labeling and internalization by a fluorescent inhibitor of prostate-specific membrane antigen. The Prostate. 2008;68(9):955-64.
167. Chen Y, Dhara S, Banerjee SR, Byun Y, Pullambhatla M, Mease RC, et al. A Low Molecular Weight PSMA-Based Fluorescent Imaging Agent for Cancer. Biochemical and biophysical research communications. 2009;390(3):624-9.
168. Kularatne SA, Wang K, Santhapuram HK, Low PS. Prostate-specific membrane antigen targeted imaging and therapy of prostate cancer using a PSMA inhibitor as a homing ligand. Mol Pharm. 2009;6(3):780-9.
169. Chen Y, Pullambhatla M, Banerjee SR, Byun Y, Stathis M, Rojas C, et al. Synthesis and biological evaluation of low molecular weight fluorescent imaging agents for the prostate-specific membrane antigen. Bioconjug Chem. 2012;23(12):2377-85.
170. Laydner H, Huang SS, Heston WD, Autorino R, Wang X, Harsch KM, et al. Robotic real-time near infrared targeted fluorescence imaging in a murine model of prostate cancer: a feasibility study. Urology. 2013;81(2):451-6.
171. Kovar JL, Cheung LL, Simpson MA, Olive DM. Pharmacokinetic and Biodistribution Assessment of a Near Infrared-Labeled PSMA-Specific Small Molecule in Tumor-Bearing Mice. Prostate Cancer. 2014;2014:104248.
172. Heidenreich A, Bellmunt J, Bolla M, Joniau S, Mason M, Matveev V, et al. EAU Guidelines on Prostate Cancer. Part 1: Screening, Diagnosis, and Treatment of Clinically Localised Disease. European Urology. 2011;59(1):61-71.
173. Sharifi N, Gulley JL, Dahut WL. Androgen deprivation therapy for prostate cancer. JAMA. 2005;294(2):238-44.
174. Kassis AI, Adelstein SJ. Radiobiologic principles in radionuclide therapy. J Nucl Med. 2005;46 Suppl 1:4S-12S.
175. Zalutsky MR, Vaidyanathan G. Astatine-211-labeled radiotherapeutics: an emerging approach to targeted alpha-particle radiotherapy. Curr Pharm Des. 2000;6(14):1433-55.
176. Langmuir VK, Fowler JF, Knox SJ, Wessels BW, Sutherland RM, Wong JY. Radiobiology of radiolabeled antibody therapy as applied to tumor dosimetry. Medical physics. 1993;20(2 Pt 2):601-10.
177. Dvorakova Z, Henkelmann R, Lin X, Turler A, Gerstenberg H. Production of 177Lu at the new research reactor FRM-II: Irradiation yield of 176Lu(n,gamma)177Lu. Appl Radiat Isot. 2008;66(2):147-51.
178. Wangler C, Buchmann I, Eisenhut M, Haberkorn U, Mier W. Radiolabeled peptides and proteins in cancer therapy. Protein Pept Lett. 2007;14(3):273-9.
179. Zoller F, Eisenhut M, Haberkorn U, Mier W. Endoradiotherapy in cancer treatment — Basic concepts and future trends. European Journal of Pharmacology. 2009;625(1–3):55-62.
180. Graham K, Wang Q, Garcia Boy R, Eisenhut M, Haberkorn U, Mier W. Synthesis and evaluation of intercalating somatostatin receptor binding peptide conjugates for endoradiotherapy. J Pharm Pharm Sci. 2007;10(2):286s-97s.

181. Parker C, Nilsson S, Heinrich D, Helle SI, O'Sullivan JM, Fossa SD, et al. Alpha emitter radium-223 and survival in metastatic prostate cancer. N Engl J Med. 2013;369(3):213-23.
182. Milowsky MI, Nanus DM, Kostakoglu L, Vallabhajosula S, Goldsmith SJ, Bander NH. Phase I trial of yttrium-90-labeled anti-prostate-specific membrane antigen monoclonal antibody J591 for androgen-independent prostate cancer. J Clin Oncol. 2004;22(13):2522-31.
183. Bander NH, Milowsky MI, Nanus DM, Kostakoglu L, Vallabhajosula S, Goldsmith SJ. Phase I trial of 177lutetium-labeled J591, a monoclonal antibody to prostate-specific membrane antigen, in patients with androgen-independent prostate cancer. J Clin Oncol. 2005;23(21):4591-601.
184. Tagawa ST, Beltran H, Vallabhajosula S, Goldsmith SJ, Osborne J, Matulich D, et al. Anti–prostate-Specific membrane antigen-based radioimmunotherapy for prostate cancer. Cancer. 2010;116(S4):1075-83.
185. Zechmann CM, Afshar-Oromieh A, Armor T, Stubbs JB, Mier W, Hadaschik B, et al. Radiation dosimetry and first therapy results with a (124)I/ (131)I-labeled small molecule (MIP-1095) targeting PSMA for prostate cancer therapy. Eur J Nucl Med Mol Imaging. 2014;41(7):1280-92.
186. Decristoforo C, Knopp R, von Guggenberg E, Rupprich M, Dreger T, Hess A, et al. A fully automated synthesis for the preparation of 68Ga-labelled peptides. Nuclear medicine communications. 2007;28(11):870-5.
187. Stetter H, Frank W. Complex Formation with Tetraazacycloalkane-N,N′,N″,N‴-tetraacetic Acids as a Function of Ring Size. Angewandte Chemie International Edition in English. 1976;15(11):686-.
188. Wieghardt K, Bossek U, Chaudhuri P, Herrmann W, Menke BC, Weiss J. 1,4,7-Triazacyclononane-N,N',N''-triacetate (TCTA), a new hexadentate ligand for divalent and trivalent metal ions. Crystal structures of [CrIII(TCTA)], [FeIII(TCTA)], and Na[CuII(TCTA)].bul.2NaBr.bul.8H2O. Inorganic Chemistry. 1982;21(12):4308-14.
189. Simecek J, Zemek O, Hermann P, Wester HJ, Notni J. A monoreactive bifunctional triazacyclononane phosphinate chelator with high selectivity for gallium-68. ChemMedChem. 2012;7(8):1375-8.
190. Notni J, Simecek J, Hermann P, Wester HJ. TRAP, a powerful and versatile framework for gallium-68 radiopharmaceuticals. Chemistry. 2011;17(52):14718-22.
191. Bernard-Gauthier V, Wängler C, Schirrmacher E, Kostikov A, Jurkschat K, Wängler B, et al. (18)F-Labeled Silicon-Based Fluoride Acceptors: Potential Opportunities for Novel Positron Emitting Radiopharmaceuticals. BioMed Research International. 2014;2014:454503.
192. McBride WJ, Sharkey RM, Goldenberg DM. Radiofluorination using aluminum-fluoride (Al18F). EJNMMI Res. 2013;3(1):36.
193. Eisenwiener KP, Powell P, Macke HR. A convenient synthesis of novel bifunctional prochelators for coupling to bioactive peptides for radiometal labelling. Bioorg Med Chem Lett. 2000;10(18):2133-5.
194. Bernhard C, Moreau M, Lhenry D, Goze C, Boschetti F, Rousselin Y, et al. DOTAGA-anhydride: a valuable building block for the preparation of DOTA-like chelating agents. Chemistry. 2012;18(25):7834-41.
195. Behr TM, Becker WS, Sharkey RM, Juweid ME, Dunn RM, Bair HJ, et al. Reduction of renal uptake of monoclonal antibody fragments by amino acid infusion. J Nucl Med. 1996;37(5):829-33.
196. Eder M, Lohr T, Bauder-Wust U, Reber M, Mier W, Schafer M, et al. Pharmacokinetic properties of peptidic radiopharmaceuticals: reduced uptake of (EH)3-conjugates in important organs. J Nucl Med. 2013;54(8):1327-30.
197. Huang SS, Wang X, Zhang Y, Doke A, DiFilippo FP, Heston WD. Improving the biodistribution of PSMA-targeting tracers with a highly negatively charged linker. The Prostate. 2014;74(7):702-13.
198. Arano Y, Wakisaka K, Ohmono Y, Uezono T, Akizawa H, Nakayama M, et al. Assessment of Radiochemical Design of Antibodies Using an Ester Bond as the Metabolizable Linkage: Evaluation of Maleimidoethyl 3-(Tri-n-butylstannyl)hippurate as a Radioiodination Reagent of Antibodies for Diagnostic and Therapeutic Applications. Bioconjugate Chemistry. 1996;7(6):628-37.
199. Dekker B, Keen H, Shaw D, Disley L, Hastings D, Hadfield J, et al. Functional comparison of annexin V analogues labeled indirectly and directly with iodine-124. Nucl Med Biol. 2005;32(4):403-13.
200. Vaidyanathan G, Zalutsky MR. Preparation of N-succinimidyl 3-[*I]iodobenzoate: an agent for the indirect radioiodination of proteins. Nat Protoc. 2006;1(2):707-13.
201. Chen Y, Foss CA, Byun Y, Nimmagadda S, Pullambhatla M, Fox JJ, et al. Radiohalogenated prostate-specific membrane antigen (PSMA)-based ureas as imaging agents for prostate cancer. J Med Chem. 2008;51(24):7933-43.
202. Iovkova L, Wangler B, Schirrmacher E, Schirrmacher R, Quandt G, Boening G, et al. para-Functionalized aryl-di-tert-butylfluorosilanes as potential labeling synthons for (18)F radiopharmaceuticals. Chemistry. 2009;15(9):2140-7.

203. Schottelius M, Reubi JC, Eltschinger V, Schwaiger M, Wester HJ. N-terminal sugar conjugation and C-terminal Thr-for-Thr(ol) exchange in radioiodinated Tyr3-octreotide: effect on cellular ligand trafficking in vitro and tumor accumulation in vivo. J Med Chem. 2005;48(8):2778-89.
204. Chandran SS, Banerjee SR, Mease RC, Pomper MG, Denmeade SR. Characterization of a targeted nanoparticle functionalized with a urea-based inhibitor of prostate-specific membrane antigen (PSMA). Cancer biology & therapy. 2008;7(6):974-82.
205. Saha GB, Whitten J, Go RT. Conditions of radioiodination with iodogen as oxidizing agent. International Journal of Radiation Applications and Instrumentation Part B Nuclear Medicine and Biology. 1989;16(4):431-3.
206. Schottelius M, Rau F, Reubi JC, Schwaiger M, Wester H-J. Modulation of Pharmacokinetics of Radioiodinated Sugar-Conjugated Somatostatin Analogues by Variation of Peptide Net Charge and Carbohydration Chemistry. Bioconjugate Chemistry. 2005;16(2):429-37.
207. Mueller D, Klette I, Baum RP, Gottschaldt M, Schultz MK, Breeman WA. Simplified NaCl based (68)Ga concentration and labeling procedure for rapid synthesis of (68)Ga radiopharmaceuticals in high radiochemical purity. Bioconjug Chem. 2012;23(8):1712-7.
208. Mathias CJ, Sun YZ, Welch MJ, Connett JM, Philpott GW, Martell AE. N,N'-bis(2-hydroxybenzyl)-1-(4-bromoacetamidobenzyl)-1,2 -ethylenediamine-N,N'-diacetic acid: a new bifunctional chelate for radiolabeling antibodies. Bioconjug Chem. 1990;1(3):204-11.
209. Schwarz SW, Mathias CJ, Sun JY, Dilley WG, Wells SA, Jr., Martell AE, et al. Evaluation of two new bifunctional chelates for radiolabeling a parathyroid-specific monoclonal antibody with In-111. International journal of radiation applications and instrumentation Part B, Nuclear medicine and biology. 1991;18(5):477-81.
210. Schuhmacher J, Klivenyi G, Hull WE, Matys R, Hauser H, Kalthoff H, et al. A bifunctional HBED-derivative for labeling of antibodies with 67Ga, 111In and 59Fe. Comparative biodistribution with 111In-DPTA and 131I-labeled antibodies in mice bearing antibody internalizing and non-internalizing tumors. International journal of radiation applications and instrumentation Part B, Nuclear medicine and biology. 1992;19(8):809-24.
211. Bailey GA, Price EW, Zeglis BM, Ferreira CL, Boros E, Lacasse MJ, et al. H(2)azapa: a versatile acyclic multifunctional chelator for (67)Ga, (64)Cu, (111)In, and (177)Lu. Inorg Chem. 2012;51(22):12575-89.
212. Price EW, Cawthray JF, Bailey GA, Ferreira CL, Boros E, Adam MJ, et al. H4octapa: an acyclic chelator for 111In radiopharmaceuticals. J Am Chem Soc. 2012;134(20):8670-83.
213. McBride WJ, Sharkey RM, Karacay H, D'Souza CA, Rossi EA, Laverman P, et al. A novel method of 18F radiolabeling for PET. J Nucl Med. 2009;50(6):991-8.
214. Laverman P, McBride WJ, Sharkey RM, Eek A, Joosten L, Oyen WJ, et al. A novel facile method of labeling octreotide with (18)F-fluorine. J Nucl Med. 2010;51(3):454-61.
215. Dorow DS, Cullinane C, Conus N, Roselt P, Binns D, McCarthy TJ, et al. Multi-tracer small animal PET imaging of the tumour response to the novel pan-Erb-B inhibitor CI-1033. Eur J Nucl Med Mol Imaging. 2006;33(4):441-52.
216. Trinkaus ME, Blum R, Rischin D, Callahan J, Bressel M, Segard T, et al. Imaging of hypoxia with 18F-FAZA PET in patients with locally advanced non-small cell lung cancer treated with definitive chemoradiotherapy. Journal of medical imaging and radiation oncology. 2013;57(4):475-81.
217. Eiber M, Maurer T, Souvatzoglou M, Beer AJ, Ruffani A, Haller B, et al. Evaluation of Hybrid 68Ga-PSMA Ligand PET/CT in 248 Patients with Biochemical Recurrence After Radical Prostatectomy. J Nucl Med. 2015;56(5):668-74.
218. Schirrmacher R, Bradtmoller G, Schirrmacher E, Thews O, Tillmanns J, Siessmeier T, et al. 18F-labeling of peptides by means of an organosilicon-based fluoride acceptor. Angew Chem Int Ed Engl. 2006;45(36):6047-50.
219. Schirrmacher E, Wängler B, Cypryk M, Bradtmöller G, Schäfer M, Eisenhut M, et al. Synthesis of p-(Di-tert-butyl[18F]fluorosilyl)benzaldehyde ([18F]SiFA-A) with High Specific Activity by Isotopic Exchange: A Convenient Labeling Synthon for the 18F-Labeling of N-amino-oxy Derivatized Peptides. Bioconjugate Chemistry. 2007;18(6):2085-9.
220. Hohne A, Yu L, Mu L, Reiher M, Voigtmann U, Klar U, et al. Organofluorosilanes as model compounds for 18F-labeled silicon-based PET tracers and their hydrolytic stability: experimental data and theoretical calculations (PET = positron emission tomography). Chemistry. 2009;15(15):3736-43.
221. Iovkova-Berends L, Wangler C, Zoller T, Hofner G, Wanner KT, Rensch C, et al. t-Bu2SiF-derivatized D2-receptor ligands: the first SiFA-containing small molecule radiotracers for target-specific PET-imaging. Molecules (Basel, Switzerland). 2011;16(9):7458-79.
222. Baranyai Z, Reich D, Vagner A, Weineisen M, Toth I, Wester H-J, et al. Shortcut to high-affinity Ga-68 and Cu-64 radiopharmaceuticals: One-pot click chemistry trimerisation on the TRAP platform. Dalton Transactions. 2015;44:11137-11146.

223. Notni J, Pohle K, Wester HJ. Comparative gallium-68 labeling of TRAP-, NOTA-, and DOTA-peptides: practical consequences for the future of gallium-68-PET. EJNMMI Res. 2012;2(1):28.
224. Imming P, Jung M-H. Pentafluorophenyl Esters of Dicarboxylic Acids. Archiv der Pharmazie. 1995;328(1):87-91.
225. Bai M, Bornhop DJ. Recent advances in receptor-targeted fluorescent probes for in vivo cancer imaging. Current medicinal chemistry. 2012;19(28):4742-58.
226. Kratochwil NA, Huber W, Muller F, Kansy M, Gerber PR. Predicting plasma protein binding of drugs: a new approach. Biochemical pharmacology. 2002;64(9):1355-74.
227. Trüssel S, Dumelin C, Frey K, Villa A, Buller F, Neri D. New Strategy for the Extension of the Serum Half-Life of Antibody Fragments. Bioconjugate Chemistry. 2009;20(12):2286-92.
228. Fischer CR, Groehn V, Reber J, Schibli R, Ametamey SM, Muller C. Improved PET imaging of tumors in mice using a novel (18) F-folate conjugate with an albumin-binding entity. Mol Imaging Biol. 2013;15(6):649-54.
229. Dumelin CE, Trussel S, Buller F, Trachsel E, Bootz F, Zhang Y, et al. A portable albumin binder from a DNA-encoded chemical library. Angew Chem Int Ed Engl. 2008;47(17):3196-201.
230. Horoszewicz JS, Leong SS, Chu TM, Wajsman ZL, Friedman M, Papsidero L, et al. The LNCaP cell line--a new model for studies on human prostatic carcinoma. Progress in clinical and biological research. 1980;37:115-32.
231. Horoszewicz JS, Leong SS, Kawinski E, Karr JP, Rosenthal H, Chu TM, et al. LNCaP model of human prostatic carcinoma. Cancer Res. 1983;43(4):1809-18.
232. Lupold SE, Hicke BJ, Lin Y, Coffey DS. Identification and characterization of nuclease-stabilized RNA molecules that bind human prostate cancer cells via the prostate-specific membrane antigen. Cancer Res. 2002;62(14):4029-33.
233. Zhang AX, Murelli RP, Barinka C, Michel J, Cocleaza A, Jorgensen WL, et al. A remote arene-binding site on prostate specific membrane antigen revealed by antibody-recruiting small molecules. J Am Chem Soc. 2010;132(36):12711-6.
234. Wangler C, Waser B, Alke A, Iovkova L, Buchholz HG, Niedermoser S, et al. One-step (1)(8)F-labeling of carbohydrate-conjugated octreotate-derivatives containing a silicon-fluoride-acceptor (SiFA): in vitro and in vivo evaluation as tumor imaging agents for positron emission tomography (PET). Bioconjug Chem. 2010;21(12):2289-96.
235. Šimeček J, Hermann P, Havlíčková J, Herdtweck E, Kapp TG, Engelbogen N, et al. A Cyclen-Based Tetraphosphinate Chelator for the Preparation of Radiolabeled Tetrameric Bioconjugates. Chemistry – A European Journal. 2013;19(24):7748-57.
236. Banerjee SR, Pullambhatla M, Foss CA, Nimmagadda S, Ferdani R, Anderson CJ, et al. 64Cu-Labeled Inhibitors of Prostate-Specific Membrane Antigen for PET Imaging of Prostate Cancer. Journal of Medicinal Chemistry. 2014;57(6):2657-69.
237. Šimeček J, Notni J, Kapp TG, Kessler H, Wester H-J. Benefits of NOPO As Chelator in Gallium-68 Peptides, Exemplified by Preclinical Characterization of 68Ga-NOPO–c(RGDfK). Molecular Pharmaceutics. 2014;11(5):1687-95.
238. Tykvart J, Schimer J, Barinkova J, Pachl P, Postova-Slavetinska L, Majer P, et al. Rational design of urea-based glutamate carboxypeptidase II (GCPII) inhibitors as versatile tools for specific drug targeting and delivery. Bioorganic & medicinal chemistry. 2014;22(15):4099-108.
239. Carone FA, Peterson DR, Oparil S, Pullman TN. Renal tubular transport and catabolism of proteins and peptides. Kidney Int. 1979;16(3):271-8.
240. Uehara T, Koike M, Nakata H, Hanaoka H, Iida Y, Hashimoto K, et al. Design, Synthesis, and Evaluation of [188Re]Organorhenium-Labeled Antibody Fragments with Renal Enzyme-Cleavable Linkage for Low Renal Radioactivity Levels. Bioconjugate Chemistry. 2006;18(1):190-8.
241. Li L, Olafsen T, Anderson AL, Wu A, Raubitschek AA, Shively JE. Reduction of kidney uptake in radiometal labeled peptide linkers conjugated to recombinant antibody fragments. Site-specific conjugation of DOTA-peptides to a Cys-diabody. Bioconjug Chem. 2002;13(5):985-95.
242. Akizawa H, Imajima M, Hanaoka H, Uehara T, Satake S, Arano Y. Renal brush border enzyme-cleavable linkages for low renal radioactivity levels of radiolabeled antibody fragments. Bioconjug Chem. 2013;24(2):291-9.
243. Benesova M, Schafer M, Bauder-Wust U, Mier W, Haberkorn U, Eisenhut M, et al. Linker Modifications of DOTA-conjugated Inhibitors of the Prostate-Specific Membrane Antigen (PSMA). Eur J Nucl Med Mol Imaging. 2013;40:S281-S.
244. Wang H, Byun Y, Barinka C, Pullambhatla M, Bhang H-eC, Fox JJ, et al. Bioisosterism of urea-based GCPII inhibitors: Synthesis and structure–activity relationship studies. Bioorganic & Medicinal Chemistry Letters. 2010;20(1):392-7.
245. Foss CA, Mease RC, Fan H, Wang Y, Ravert HT, Dannals RF, et al. Radiolabeled small-molecule ligands for prostate-specific membrane antigen: in vivo imaging in experimental models of prostate cancer. Clin Cancer Res. 2005;11(11):4022-8.

246. Gourni E, Demmer O, Schottelius M, D'Alessandria C, Schulz S, Dijkgraaf I, et al. PET of CXCR4 expression by a (68)Ga-labeled highly specific targeted contrast agent. J Nucl Med. 2011;52(11):1803-10.
247. Skidgel RA. Basic carboxypeptidases: regulators of peptide hormone activity. Trends in pharmacological sciences. 1988;9(8):299-304.
248. Arano Y, Fujioka Y, Akizawa H, Ono M, Uehara T, Wakisaka K, et al. Chemical Design of Radiolabeled Antibody Fragments for Low Renal Radioactivity Levels. Cancer Research. 1999;59(1):128-34.
249. Kratochwil C, Giesel FL, Leotta K, Eder M, Hoppe-Tich T, Youssoufian H, et al. PMPA for Nephroprotection in PSMA-Targeted Radionuclide Therapy of Prostate Cancer. J Nucl Med. 2015;56(2):293-8.
250. Eder M, Schafer M, Bauder-Wust U, Haberkorn U, Eisenhut M, Kopka K. Preclinical evaluation of a bispecific low-molecular heterodimer targeting both PSMA and GRPR for improved PET imaging and therapy of prostate cancer. The Prostate. 2014;74(6):659-68.
251. O'Keefe DS, Bacich DJ, Heston WD. Comparative analysis of prostate-specific membrane antigen (PSMA) versus a prostate-specific membrane antigen-like gene. The Prostate. 2004;58(2):200-10.
252. Weineisen M, Schottelius M, Simecek J, Baum RP, Yildiz A, Beykan S, et al. 68Ga- and 177Lu-Labeled PSMA I&T: Optimization of a PSMA-Targeted Theranostic Concept and First Proof-of-Concept Human Studies. J Nucl Med. 2015;56:1169-76.
253. KleinJan GH, van den Berg NS, Brouwer OR, de Jong J, Acar C, Wit EM, et al. Optimisation of fluorescence guidance during robot-assisted laparoscopic sentinel node biopsy for prostate cancer. Eur Urol. 2014;66(6):991-8.
254. Perner S, Hofer MD, Kim R, Shah RB, Li H, Moller P, et al. Prostate-specific membrane antigen expression as a predictor of prostate cancer progression. Human pathology. 2007;38(5):696-701.
255. Herrmann K, Bluemel C, Weineisen M, Schottelius M, Wester HJ, Czernin J, et al. Biodistribution and radiation dosimetry for a novel probe targeting prostate specific membrane antigen for Imaging and Therapy (68Ga-PSMA I&T). J Nucl Med. 2015;56:855-861.

4 PUBLICATIONS

Peer-reviewed journal articles

- Weineisen M, Simecek J, Schottelius M, Schwaiger M, Wester H-J. Synthesis and preclinical evaluation of DOTAGA-conjugated PSMA ligands for functional imaging and endoradiotherapy of prostate cancer. EJNMMI Research. 2014;4(1):63.
- Baranyai Z, Reich D, Vagner A, Weineisen M, Toth I, Wester H-J, et al. Shortcut to high-affinity Ga-68 and Cu-64 radiopharmaceuticals: One-pot click chemistry trimerisation on the TRAP platform. Dalton Transactions. 2015;44:11137-11146.
- Herrmann K, Bluemel C, Weineisen M, Schottelius M, Wester HJ, Czernin J, et al. Biodistribution and radiation dosimetry for a novel probe targeting prostate specific membrane antigen for Imaging and Therapy (^{68}Ga-PSMA I&T). J Nucl Med. 2015;56:855-861.
- Maurer T, Weirich G, Schottelius M, Weineisen M, Frisch B, Okur A, et al. Prostate-specific Membrane Antigen-radioguided Surgery for Metastatic Lymph Nodes in Prostate Cancer. Eur Urol. 2015;68:530-534.
- Weineisen M, Schottelius M, Simecek S, Baum RP, Yildiz A, et al. ^{68}Ga- and ^{177}Lu-labeled PSMA I&T: Optimization of a PSMA targeted theranostic concept and first proof of concept human studies. J Nucl Med. 2015;56:1169-1176.

Reviews

- Weineisen M, Robu S, Schottelius M, Wester H-J. Novel and Established Radiopharmaceuticals for Diagnosis and Therapy of Prostate Carcinoma. Nuklearmediziner. 2015;38:89-98.

Selected conference abstracts

- Weineisen M, Schottelius M, Simecek J, Baum R, Schwaiger M, Wester H. J. Evaluation of new chelator-conjugated PSMA ligands for diagnostic imaging and endoradiotherapy of prostate cancer. Nuklearmedizin. 2014;53:A10.
- Weineisen M, Schottelius M, Simecek J, Wester H. New chelator-conjugated PSMA ligands for functional imaging and endoradiotherapy of prostate cancer. Eur J Nucl Med Mol Imaging. 2013;40:S258.
- Simecek J, Notni J, Pohle K, Kapp T, Weineisen M, Schottelius M et al. NOPO-based 68Ga and 64Cu PET radiopharmaceuticals. Eur J Nucl Med Mol Imaging. 2013;40:S422.
- Kulkarni H, Weineisen M, Mueller D, Schuchardt C, Schottelius M, Wester H et al. First clinical results with Lu-177 PSMA-TUM1 for the treatment of castrate-resistant metastatic prostate cancer. J Nucl Med. 2014;55:10.
- Schuchardt C, Weineisen M, Wiessalla S, Schottelius M, Kulkarni H, Mueller D et al. Biodistribution and dosimetry of Lu-177 PSMA in metastasized castrate resistant prostate cancer patients. J Nucl Med. 2014;55:641.
- Weineisen M, Schottelius M, Simecek J, Eiber M, Schwaiger M, Wester H. Development and first in human evaluation of PSMA I&T - A ligand for diagnostic imaging and endoradiotherapy of prostate cancer. J Nucl Med. 2014;55:1083.

- Kulkarni H, Weineisen M, Mueller D, Schuchardt C, Schottelius M, Wester H, Baum R. Safety and Efficacy of Lu-177 PSMA-TUM1 for THERANOSTICS of Castrate-Resistant Metastatic Prostate Cancer: Initial Results. Eur J Nucl Med Mol Imaging 2014, 41:291.

- Weineisen M, Roselt P, Cullinane C, Hicks R, Wester H. Design and evaluation of a high-affinity AlF-18 labeled PSMA inhibitor for PET imaging of prostate cancer. Nuklearmedizin 2015; 53 (P22).

- Eiber M, Schottelius M, Weineisen M, Weirich G, Kübler H, Gschwend J et al. Use of a 111In-labelled PSMA-ligand for intraoperative radioguided surgery in recurrent prostate cancer. Nuklearmedizin 2015; 53 (V100).

- Frisch B, Maurer T, Okur A, Weineisen M, Schottelius M, Weirich G et al. Freehand SPECT for PSMA-radioguided lymphadenectomy in prostate cancer patients. J. Nucl Med. 2015.

- Kulkarni H, Baum R, Weineisen M, Wester H, Schuchardt C, Wiessalla S et al. Therapy of Metastasized Castrate-Resistant Prostate Cancer Using Lu-177 Labeled DOTAGA-PSMA Small Molecules: First Clinical Results in a Larger Patient Cohort. J Nucl Med. 2015;56:10.

- Weineisen M, Roselt P, Cullinane O'Keefe G, Rigopoulos A, Hicks R, Wester HJ. Preliminary investigation of a gallium-68, copper-64 and lutetium-177 labeled PSMA targeting ligand for imaging and radionuclide therapy of prostate cancer. Internal Medicine Journal. 2015;45:1-20.

5 ACKNOWLEDGEMENTS

Particularly, I would like to thank Prof. Dr. Hans-Jürgen Wester for giving me the possibility of performing a doctorate in his group, for the interesting research project, the support in all scientific questions and your intensive collaboration to organize the initial patient applications. I am very grateful for supporting and finally realizing my research internship at the Peter MacCallum Cancer Centre in Melbourne, Australia.

PD Dr. Margret Schottelius, Dr. Behrooz Yousefi and Dr. Johannes Notni merit acknowledgement for the important discussions on my project, synthetic and instrumental impact, reading abstracts, presentations, posters, and papers. Special thanks are due to you, Margret Schottelius, for all the last-minute support on evenings and weekends! Thanks Jakub Simecek for your expertise in radiometallation and metabolite analysis, I learned a lot from you. I would like to thank Dr. Behrooz Yousefi for your advice and discussions about all the important things of life and work and Dr. Frauke Hoffmann for your expertise in the animal work. I very much appreciate all of your contribution, Steffi Robu, Theresa Osl, Andi Poschenrieder and Alex Schmidt, in supervision of my students in the lab. Thank you also to Sven and Moni for always helping out. The lab work conducted by the students Simon Schmied, Alexander Wurzer, Dominik Reich, Markus Miedl, Claudia Ott, Thomas Günther, Simon Moosmang, Sophia Beslmüller and Stefanie Heilmann is highly acknowledged.

Prof. Dr. Rod Hicks, Dr. Peter Roselt, Wayne Noonan, Dr. Carleen Cullinane and her group, especially Patricia and Kelly, I would like to thank for the help with setting up and performing my experiments and for finalizing the animal work. Thanks to all people I met in Melbourne, especially Margarete Kleinschmidt, Peter Roselt and Christian Wichmann for making this business trip an unforgettable experience.

Prof. Dr. Markus Schwaiger I would like to thank for the lab space, and together with PD Dr. Matthias Eiber, Dr. Tobias Maurer and colleagues for a successful cooperation and important scientific discussions. The contribution of the PET/SPECT-MTAs, especially Simone Loher for taking blood samples (thanks Sven for volunteering to provide your veins!) and assistance with the activity deliveries and ordering is highly recognized. Thanks goes to the GMP team and cyclotron operators, R. Klitsch, Michael Herz, Marina Schenk, Alexander Ruffani and Andrea Alke for the support in ^{11}C production, quality control and for lending your Allen wrench.

For practical and theoretical explanations on small animal PET imaging thanks is due to Dr. Iina Laitinen and Prof. Dr. Sibylle Ziegler. Special thanks are due to the small animal PET Team, Sybille Reder, Markus Mittelhäuser and Marco Lehmann, for always making additional scans possible, especially when the tumor growth was unpredictable and for your help with catheter injections of animals.

I very much appreciate the backing from my family, especially from my parents. Fabi, thanks for tolerating my bad moods and always motivating and encouraging me to continue.